Have you tried turning the light off and on again?- Mechanistic studies on the impact of light on the hydrogen evolution reactivity of thiomolybdates

Dissertation zur Erlangung des Grades ‘Doktor rerum naturalium (Dr. rer. nat.)’

im Promotionsfach Chemie

am Fachbereich 09 – Chemie, Pharmazie, Geographie und Geowissenschaften

der Johannes Gutenberg-Universität.

Sophia Henriette Kolbinger

Geboren in Worms

Mainz, 2026

Betreuer:

- Prof. Dr. Carsten Streb

Zweitgutachterin:

- Prof. Dr. Katja Heinze

Tag der mündlichen Prüfung: 23. Juni. 2026

Don’t dream it,

Be it!

- Frank N. Furter, Rocky Horror Picture Show

Statutory Declaration

This scientific work was carried out in the period from June 2023 to April 2026 at the Department of Chemistry at Johannes Gutenberg-University Mainz under the supervision of Prof. Dr. Carsten Streb.

I, Sophia Henriette Kolbinger, hereby declare that I wrote this dissertation with the title "*Have you tried turning the light off and on again? – Mechanistic studies on the impact of light on the hydrogen evolution reactivity of thiomolybdates*" without any unauthorized external assistance and used only sources acknowledged in the work. All textual passages which are appropriate verbatim or paraphrased from published and unpublished texts as well as all information obtained from oral sources are duly indicated and listed in accordance with bibliographical rules. I hereby certify that I have not used any aids whose use the examiner has explicitly prohibited. In carrying out this research, I complied with the rules of standard scientific practice as formulated in the statutes of Johannes Gutenberg-University Mainz to ensure standard scientific practice.

The AI-tools used for writing this work are documented in Table 1. By submitting this work, I assume responsibility for the entire submitted product. I am therefore also responsible for any AI-generated content that I have included in my work. I have verified the accuracy of the included (AI-generated) statements and content to the best of my knowledge and belief.

I am aware that a violation of the aforementioned points will result in disciplinary consequences and, in particular, may lead to the doctoral thesis being graded as "failed." Enrollment may be revoked for up to two years if a student cheats on examinations on two or more occasions (§ 69 (4) and (5) HochSchG).

I further declare that I have not yet submitted this scientific work in the same or a similar form to any other German university, foreign university or comparable institution for the award of another academic degree or qualification. I have neither successfully or unsuccessfully completed a doctorate or a comparable graduation procedure in this doctoral subject with the doctoral degree "Dr. rer. nat.", nor have I successfully applied for admission to a doctoral examination or a comparable graduation procedure in the subject of this doctorate "Dr. rer. nat." at the Johannes Gutenberg-University Mainz or another

university with the right to award doctorates. I further affirm that I have not made use of any paid assistance from third parties, in particular no doctoral advice or mediation.

I am aware of the current doctoral degree regulations of Johannes Gutenberg-University Mainz dated October 18, 2021 in the version of February 17, 2025 for the acquisition of the degree “Dr. rer. nat.”. I hereby apply for the doctoral degree in natural science from Johannes Gutenberg University Mainz for the first time.

_____

Place, Date Sophia Henriette Kolbinger

Table 1: Usage of AI-tools

AI-Tool	Used for	Why	When
ChatGPT	Literature research	Finding relevant and suited Publications and Reviews for this thesis	Reviewing literature for this work
ChatGPT	Rephrasing of my draft text	Improving readability	Throughout the whole work
DeepL Translate	Translation English-german and vice versa	Improving readability and finding accurate translation for words and phrases.	Throughout the whole work

ChemDraw, Powerpoint and Python were used to create the figures.

Abstract

As the global population continues to grow, energy demand is increasing rapidly. At present, energy production is still largely associated with greenhouse gas emissions, which contribute significantly to climate change. Therefore, the development of sustainable and environmentally friendly energy technologies has become increasingly urgent. Hydrogen is widely regarded as a promising energy carrier, as it enables the controlled storage and transport of energy. However, its current production is itself often associated with substantial greenhouse gas emissions and high energy consumption. Consequently, new strategies for hydrogen production based on renewable energy sources and sustainable materials are required.

In recent years, thiomolybdates have attracted considerable attention as catalysts for the light-driven hydrogen evolution reaction (HER). This work focuses on the reactivity of thiomolybdates and their reaction mechanism with an emphasis on the impact of light.

Prominent representatives of this compound class are the $[Mo_3S_{13}]^{2-}$ (**{Mo_3}**) and the $[Mo_2S_{12}]^{2-}$ (**{Mo_2}**) clusters. While the intrinsic reaction conditions of homogeneous light-driven HER systems employing these clusters have already been extensively studied and optimized in the literature, extrinsic parameters such as irradiation conditions have often been neglected. In this work, the influence of dynamic irradiation on these systems was investigated using a Design of Experiments (DoE) approach. Three parameters were selected: frequency, duty cycle, and LED current, the latter determining the irradiation power. The individual effects of these parameters, as well as their interactions, were evaluated. Based on the resulting data analysis, optimized parameter settings for maximizing the turnover number (TON) were identified. In addition, their influence on photonic efficiency was assessed. Furthermore, degradation of both the photosensitizer (PS) and the catalyst under optimized irradiation conditions was investigated in order to rationalize the observed trends. Time-dependent density functional theory (TD-DFT) calculations were used to interpret UV-Vis spectroscopic data obtained during the catalyst degradation process.

Thio-oxo-molybdates have also been proposed in the literature as promising catalysts for the light-driven HER, although this field has so far received comparatively little attention.

To address this knowledge gap, initial photocatalytic and mechanistic studies on the thio-oxo-molybdate $[Mo_2O_2S_6]^{2-}$ as prototype were carried out in a homogeneous system. Possible catalyst degradation via ligand exchange, as previously reported for thiomolybdates, was investigated using Raman and UV-Vis spectroscopy. In addition, TD-DFT calculations were performed to evaluate the catalytic activity of the different species formed during this process, and a plausible reaction mechanism was proposed.

This work includes two peer-reviewed publications and one manuscript in preparation. In all publications and manuscripts, the contribution of the author of this thesis includes: Conceptualization, methodology, investigation, formal analysis, data processing, writing original draft, visualization, discussion and revision.

For Information in more detail, see chapter 3.

Zusammenfassung

Da die Weltbevölkerung weiterhin wächst, steigt der Energiebedarf rapide an. Derzeit ist die Energieerzeugung noch weitgehend mit Treibhausgasemissionen verbunden, die erheblich zum Klimawandel beitragen. Daher wird die Entwicklung nachhaltiger und umweltfreundlicher Energietechnologien immer dringlicher. Wasserstoff gilt weithin als vielversprechender Energieträger, da er die kontrollierte Speicherung und den Transport von Energie ermöglicht. Seine derzeitige Herstellung ist jedoch oft selbst mit erheblichen Treibhausgasemissionen und hohem Energieverbrauch verbunden. Folglich sind neue Strategien zur Wasserstoffproduktion auf der Grundlage erneuerbarer Energiequellen und nachhaltiger Materialien erforderlich.

In den letzten Jahren haben Thiomolybdate als Katalysatoren für die lichtgetriebene Wasserstoffentwicklungsreaktion (HER) große Aufmerksamkeit auf sich gezogen. Im Mittelpunkt dieser Arbeit stehen die Reaktivität von Thiomolybdaten und deren Reaktionsmechanismen, wobei der Schwerpunkt auf dem Einfluss von Licht liegt.

Prominente Vertreter dieser Verbindungsklasse sind die $[Mo_3S_{13}]^{2-}$ (**{Mo_3}**) und $[Mo_2S_{12}]^{2-}$ (**{Mo_2}**) Cluster. Während die intrinsischen Reaktionsbedingungen homogener, lichtgetriebener HER-Systeme, die diese Cluster nutzen, in der Literatur bereits umfassend untersucht und optimiert wurden, wurden extrinsische Parameter wie die Bestrahlungsbedingungen oft vernachlässigt. In dieser Arbeit wurde der Einfluss dynamischer Bestrahlung auf diese Systeme unter Verwendung eines Design-of-Experiments-Ansatzes (DoE) untersucht. Es wurden drei Parameter ausgewählt: Frequenz, An/Aus-Verhältnis und LED-Strom, wobei letzterer die Bestrahlungsleistung bestimmt. Auf der Grundlage der daraus resultierenden Datenanalyse wurden optimierte Parametereinstellungen zur Maximierung der Umsatzzahl (TON) ermittelt. Zudem wurde deren Einfluss auf die photonische Effizienz bewertet. Darüber hinaus wurde der Abbau sowohl des Photosensibilisators (PS) als auch der Katalysatoren unter optimierten Bestrahlungsbedingungen untersucht, um die beobachteten Trends zu erklären. Zur Interpretation der während des Katalysatorabbaus gewonnenen UV-Vis-spektroskopischen Daten wurden Berechnungen nach der zeitabhängigen Dichtefunktionaltheorie (TD-DFT) unterstützend herangezogen.

Thio-Oxo-Molybdate wurden in der Literatur ebenfalls als vielversprechende Katalysatoren für die lichtgetriebene HER vorgeschlagen, obwohl diesem Bereich bislang vergleichsweise wenig Aufmerksamkeit geschenkt wurde. Um diese Wissenslücke zu schließen, wurden erste photokatalytische und mechanistische Untersuchungen am Thio-Oxo-Molybdat $[Mo_2O_2S_6]^{2-}$ als Prototyp in einem homogenen System durchgeführt. Ein möglicher Katalysatorabbau durch Ligandenaustausch, wie er zuvor für Thiomolybdate beschrieben wurde, wurde mittels Raman- und UV-Vis-Spektroskopie untersucht. Darüber hinaus wurden TD-DFT-Berechnungen durchgeführt, um die katalytische Aktivität der verschiedenen während dieses Prozesses gebildeten Spezies zu bewerten, und ein plausibler Reaktionsmechanismus wurde vorgeschlagen.

Diese Arbeit umfasst zwei begutachtete Veröffentlichungen und ein Manuskript in Begutachtung. Bei allen Veröffentlichungen und Manuskripten umfasst der eigene Beitrag der Autorin dieser Dissertation: Konzeption, Methodik, Untersuchung, formale Analyse, Datenverarbeitung, Verfassen des ersten Entwurfs, Visualisierung, Diskussion und Überarbeitung.

Nähere Informationen finden Sie im Kapitel 3.

Table of Contents

List of abbreviations

The following abbreviations were used, in addition to standard notations:

A	Absorbance
Ab	Absorption
Ac	Electron acceptor
ADP	Adenosine diphosphate
Asc	Ascorbate
AscH	Ascorbic acid
ATP	Adenosine triphosphate
bpy	2,2’-bipyridine
Cat	Catalyst
Chl a	Chlorophyll a
Cys	Cysteine
Cyt b_6f	Cytochrome b_6f
D	Electron donor
DoE	Design of Experiments
E	Energy
EDTA	Ethylenediaminetetraacetic acid
F	Fluorescence
FAIR	Finable, Accessible, interoperable, reusable
Fe/S	Iron-sulfur-based cluster
Ferr	Ferredoxin
FNR	Ferredoxin-NADP reductase
FRET	Förster resonance energy transfer
HEC	Hydrogen evolution catalysis
HER	Hydrogen evolution reaction
IC	Internal conversion
ISC	Intersystem crossing

LED	Light emitting diode
MeOH	Methanol
MLCT	Metal-to-ligand charge transfer
MO	Molecular orbital
{Mo_2}	$[Mo_2S_{12}]^{2-}$
{Mo_3}	$[Mo_3S_{13}]^{2-}$
NAD	Nicotinamide adenine dinucleotide
NADPH	Nicotinamide adenine dinucleotide phosphate
NHE	Normal hydrogen electrode
OEC	Oxygen evolution complex
P	Phosphorescence
PC	Plastocyanin
PCET	Proton-coupled electron transfer
Pheo	Pheophytin
P_i	Inorganic phosphate
PQ	Plastoquinone
S	Singlet
SED	Sacrificial electron donor
T	Triplet
TD-DFT	Time-dependent Density functional theory
TEA	Triethyl amine
TEOA	Triethanol amine
TOF	Turnover frequency
TON	Turnover number
Tyr	Tyrosine
UV-Vis	Ultraviolet-visible
Vit K_1	Vitamin K_1
VR	Vibrational relaxation

Scientific Contributions

List of peer-reviewed publications

1. "Fewer photons, more hydrogen: effects of dynamic irradiation on light-driven hydrogen evolution by thiomolybdate catalysts", S. H. Kolbinger, L. Haxha, P. C. Schröder, D. Kowalczyk, L. Senz, L. Schleicher, A. Mukherjee, D. Malcolm, C. L. Kufner, D. Ziegenbalg* and C. Streb,* *Sustainable Energy Fuels*, **2026**, 10, 1313-1320.

   DOI: 10.1039/D5SE01490E

2. "Light-driven hydrogen evolution reactivity of molecular thio-oxomolybdate catalysts", L. T. Schleicher, ‡ S. H. Kolbinger, ‡ A. Edwards, K. Sellmann, L. Senz, S. Kupfer, M. Schmitt,* J. Popp and C. Streb,* *Sustainable Energy Fuels*, **2026**, *Accepted Manuscript*.

   DOI: 10.1039/D6SE00061D

All publications are reprinted within this work with the permission of the respective publisher (see chapter 3).

Authors who contributed equally to the respective publications and are therefore joint first authors of these works have been marked with the symbol "‡". The corresponding authors are indicated with an asterisk "*".

Conferences and Conference Contributions

18.06.2023 - 23.06.2023	**MECAREACT**, Paris, *Poster*
21.07.2023 – 23.07.2023	**young Symposium on the Photochemistry and Photophysics of Coordination Compounds**, Ulm, *member of the organization team*
23.07.2023 - 27.07.2023	**25th International Symposium on the Photochemistry and Photophysics of Coordination Compounds**, Ulm, *Participation*
25.02.2024 - 28.02.2024	**Koordinationschemie Treffen**, Innsbruck, *Poster*

28.07.2024 - 04.08.2024	**International Conference on Raman Spectroscopy 2024**, Rome, *Poster*
05.08.2024 - 09.08.2024	**Non-contact Atomic Force Microscopy 2024**, Montreal, *Poster → awarded „Best Poster Prize“*
16.09.2024 - 18.09.2024	**Lecture Conference on Photochemistry**, Mainz, *Part of the Young scientific commitee*
07.07.2025 - 12.07.2025	**26th International Symposium on the Photochemistry and Photophysics of Coordination Compounds**, Milazzo, *Poster*
21.07.2025 - 25.07.2025	**8th Frontiers in Metal Oxid Cluster Science**, Mainz, *member of the organization team*
22.09.2025 - 26.09.2025	**Catalight Summer School**, Eisenach, *Participation*

1 Intro and overview

For understanding the motivational and scientific background of this work an introduction into global warming and climate change, photosynthesis, hydrogen evolving systems in nature, hydrogen evolution reaction, performance, reactivity and stability in photocatalysis, thiomolybdates and thio-oxo-molybdates as well as Design of Experiments is necessary and summarized in the following chapters.

1.1 Global warming and Climate change

It has been known for decades that our planet is undergoing anthropogenic climate change as a consequence of elevated greenhouse gas emissions.[1] The Industrial Revolution, which began in 1750, marked the onset of large-scale human-caused greenhouse gas emissions and is widely regarded as the starting point of the present climate crisis.[2] Ongoing population growth is associated with an increasing energy demand, which in turn contributes to rising greenhouse gas emissions.[3] The most important greenhouse gases driving climate change are carbon dioxide (CO_2) and methane (CH_4).[1,2] These gases are released as by-products in a wide range of industrial and agricultural sectors. The combustion of fossil fuels for the generation of heat and electricity is among the largest sources of CO_2 emissions.[4,5] In addition, livestock farming contributes substantially to methane emissions, particularly through enteric fermentation in cattle.[6]

Greenhouse gases exert their warming effect by trapping heat in the atmosphere.[7] Solar radiation reaches the Earth and warms its surface, which subsequently emits energy back toward space in the form of infrared radiation. Greenhouse gases interfere with this radiation because their IR-active vibrational modes absorb part of the outgoing infrared radiation and re-emit it in all directions, thereby retaining heat within the atmosphere.[8] Under natural conditions, this establishes an energy balance that stabilizes the global temperature. Increased greenhouse gas levels in the atmosphere however intensify this effect and disrupt the natural radiative equilibrium.[2] The consequence is a rise in global mean temperature, which has already been observed since the late 19th century.[1]

This increase in global temperature has far-reaching consequences for ecological and climatic systems. Climate zones are shifting, winters in many regions are becoming milder, and ocean warming affects marine ecosystems, including algal growth.[9–12] At the same time, melting ice caps contribute to rising sea levels, which increases the flood risk for coastal regions.[10] In addition, climate change is associated with an increase in the frequency and intensity of extreme weather events such as storms and droughts.[13–16] These developments highlight the urgent need to reduce greenhouse gas emissions in order to mitigate further disruption of the Earth's climate system.

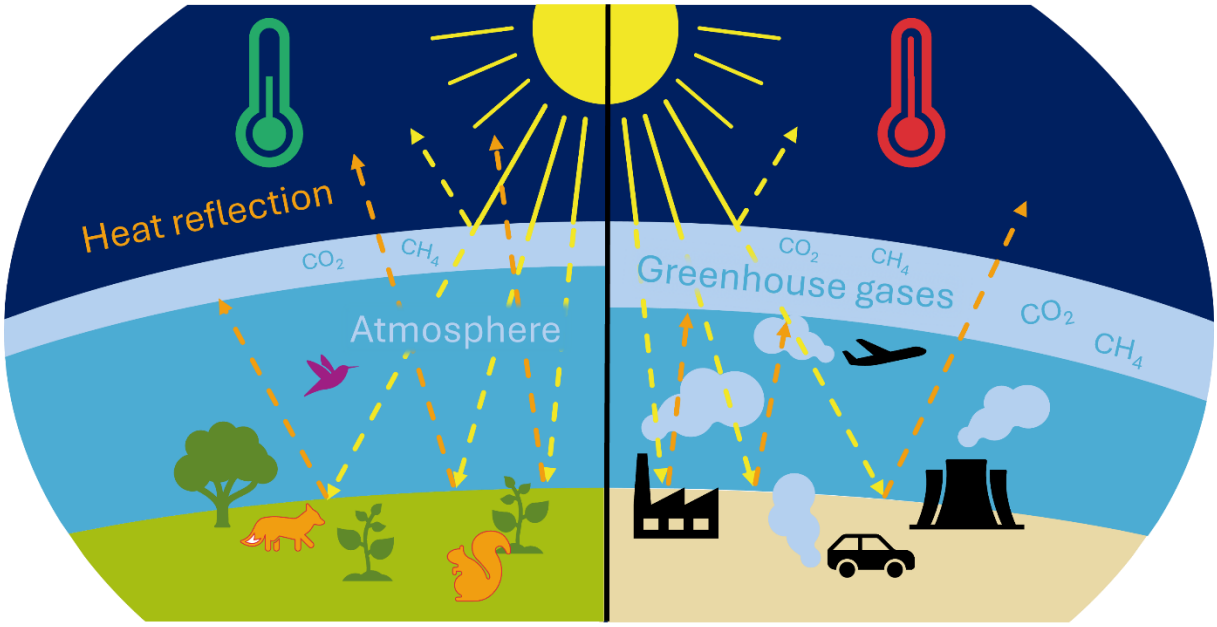

Figure 1: Schematic illustration of the greenhouse gas effect on Earth.

The use of renewable energy sources is an important strategy for reducing greenhouse gas emissions. A major limitation of many renewable energy technologies, however, is their dependence on external conditions such as weather and time of day.[17,18] For example, solar energy can be harvested using photovoltaic systems. However, its availability is limited to periods of sufficient solar irradiation and therefore varies both geographically and temporally.[17,19,20] In contrast, energy demand often remains high during periods of low or no solar input, particularly at night.[21] This mismatch between energy production and energy demand creates the need for efficient energy storage technologies.[21,22]

Various approaches for energy storage have already been developed and are applied in practice, including pumped hydro storage,[23,24] batteries,[25,26] and chemical fuels.[27,28]

Another promising option is the storage of energy in the form of hydrogen.[29–31] Owing to its low molecular weight and high molar enthalpy of combustion, hydrogen exhibits an exceptional gravimetric energy density of 120–142 MJ kg^{-1}.[32,33] On Earth, however, hydrogen does not occur naturally in substantial amounts in its elemental form (H_2), but is predominantly bound in hydrogen-containing compounds. Therefore, hydrogen must be produced from suitable feedstocks such as water, alcohols (e.g., methanol or ethanol), or biomass-derived compounds.[34,35]

At present, industrial hydrogen production is still associated with substantial greenhouse gas emissions. Large-scale hydrogen demand is driven, among other factors, by ammonia synthesis via the Haber–Bosch process, which is essential for fertilizer production.[36] Conventional hydrogen production methods, such as steam reforming and hydrocarbon pyrolysis, require significant energy input and are often based on fossil resources, resulting in considerable CO_2 emissions.[37] It is therefore essential to develop sustainable and low-emission routes for hydrogen production. One of the best-known natural examples of light-driven proton-coupled reduction based on renewable resources is photosynthesis.

1.2 Photosynthesis

Photosynthesis is the most prominent natural example of photocatalysis. It is carried out by plants, algae, and cyanobacteria,[38,39] the latter of which played a crucial role in the oxygenation of the Earth's early atmosphere.[40,41] Photosynthesis is therefore fundamental to most life on Earth. Although molecular oxygen is generated during this process, it is primarily a by-product of water oxidation and does not represent the main energetic benefit for the photosynthetic organism.[39] The primary purpose of photosynthesis is the conversion of solar energy into chemical energy, which is initially stored in the form of nicotinamide adenine dinucleotide phosphate (NADPH) and adenosine triphosphate (ATP), and is subsequently used for the synthesis of carbohydrates.[40,42] These carbohydrates serve as energy-rich compounds and contribute to biomass formation.[43]

In plants and cyanobacteria, the light-driven processes of photosynthesis take place in thylakoid membranes.[39] These membranes separate the thylakoid lumen from the surrounding stroma and provide the structural environment for the photosynthetic

electron transport chain. In plant cells, thylakoids are located within chloroplasts, whereas in cyanobacteria they form internal membrane systems within the cell.[39]

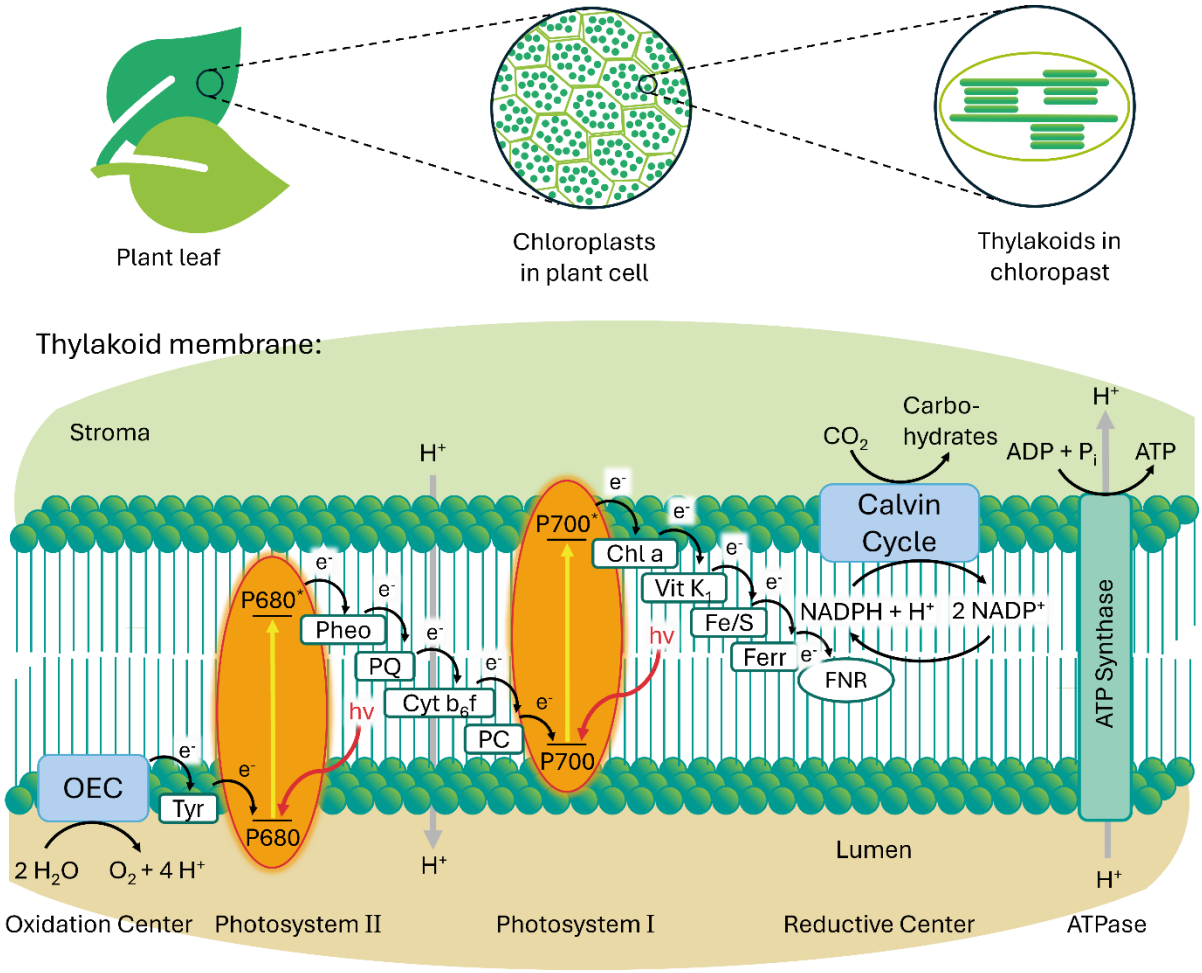

Figure 2: Z-scheme of natural photosynthesis in the thylakoid membrane showing the correlations of the individual components for the most important electron transfer steps and essential reactions. Note that the positions of the components imply the divergent relative energy values rather than absolute energy values or energetic distances. The following abbreviations for the compounds involved were used: OEC: oxygen-evolving complex; Tyr: tyrosine; P680: photoactive special pair of Photosystem II; Pheo: pheophytin; PQ: plastoquinone; Cyt b_6f: cytochrome b_6f; PC: plastocyanin; P700: photoactive special pair of Photosystem I; Chl a: chlorophyll a; Vit K_1: vitamin K_1; Fe/S: iron-sulfur-based clusters; Ferr: ferredoxin; FNR: ferredoxin-NADP reductase; NADP: nicotinamide adenine dinucleotide phosphate; ADP: adenosine diphosphate; P_i: inorganic phosphate; ATP: adenosine triphosphate.[44,45]

Photosynthesis can be divided into three major stages:

- Photosystem II: light absorption and water oxidation
- Photosystem I: light absorption and $NADP^+$ reduction
- Carbon fixation: CO_2 reduction in the Calvin cycle

Each of these stages plays a crucial role in converting electromagnetic energy in the form of light into chemical energy and involves a sequence of coupled reaction steps. The process begins with the absorption of light by the light-harvesting pigments associated with Photosystem II.[39] The photochemically active reaction center is referred to as P680, named after its absorption maximum at 680 nm. Excitation energy is transferred between the antenna pigments (chlorophyll and β-carotene) and the reaction center by Förster resonance energy transfer (FRET) until charge separation occurs.[46,47] This leads to electron transfer from the excited reaction center to a nearby pheophytin molecule.[47] From pheophytin, the electron is transferred further to plastoquinone, which subsequently delivers electrons via the cytochrome b_6f complex to plastocyanin.[47,48] Plastocyanin then serves as the mobile electron carrier connecting the two photosystems.[48]

The oxidized reaction center $P680^+$ is regenerated by electron transfer from the oxygen-evolving complex, where water is oxidized to molecular oxygen, protons, and electrons.[49] This process occurs on the lumenal side of the thylakoid membrane and contributes to proton accumulation in the thylakoid lumen, thereby supporting the formation of a proton gradient across the membrane.[50,51] This proton gradient is later used by ATP synthase for ATP production.[52]

The process continues in Photosystem I. In this photosystem, light is absorbed by the antenna pigments and transferred to the reaction center of P700, which is named after its absorption maximum at approximately 700 nm.[53,54] Following excitation, charge separation occurs and an electron is transferred from the excited reaction center to a series of electron acceptors.[53,54] As in Photosystem II, excitation energy is transferred through the pigment network by FRET before photochemical charge separation takes place.[53]

The electron is transferred from P700* via chlorophyll a and phylloquinone (vitamin K_1) to a series of iron-sulfur clusters and finally to ferredoxin.[39] Ferredoxin then serves as the electron donor for ferredoxin–$NADP^+$ reductase, which catalyzes the reduction of NADP+ to NADPH.[39] This NADPH is subsequently used in carbon fixation reactions as electron and proton donor.[43] The oxidized reaction center $P700^+$ is regenerated by electron transfer from plastocyanin, which delivers electrons Photosystem II.[39]

During the photosynthetic electron transport cascade, protons are translocated from the stroma into the thylakoid lumen, resulting in the formation of a proton gradient across the thylakoid membrane.[50,52] This electrochemical gradient provides the driving force for ATP synthesis by ATP synthase.[52] The enzyme catalyzes the conversion of adenosine diphosphate (ADP) and inorganic phosphate (P_i) into ATP on the stromal side of the membrane.[52] Although no additional photon absorption is required directly for ATP formation itself, this process is still functionally part of the light-dependent reactions because it relies on the proton gradient generated by light-driven electron transfer.[50,51]

ATP is the universal cellular energy carrier and powers numerous biological processes.[55] Together with NADPH, which is also generated during the light-dependent reactions, ATP provides the chemical energy required for subsequent carbon fixation and carbohydrate synthesis.[42] In this way, photosynthesis converts light energy into chemically stored energy that sustains the metabolism and growth of the organism.

In the subsequent light-independent reactions, the ATP and NADPH generated during the light-dependent stage are consumed in the Calvin cycle to drive the reduction and assimilation of CO_2.[43] The Calvin cycle comprises a series of enzyme-catalyzed reactions through which inorganic carbon is incorporated into organic molecules.[43] In this way, carbohydrates are synthesized from CO_2 using the chemical energy and reducing equivalents provided by ATP and NADPH.[43]

In both photosystems, energy-transfer and electron-transfer processes are involved in directing the absorbed photon energy to the reactive sites, as outlined above. The relevant energy-transfer mechanism is FRET. In this process, dipole-dipole interactions ($\Delta\mu$) between an excited donor (D*) and an acceptor (Ac) enable non-radiative energy transfer (Figure 3a).[56] As a result, the donor returns to its ground state (D), while the acceptor is promoted to its excited state (Ac*).[56]

In contrast, oxidative electron transfer involves the transfer of an electron from an excited donor (D*) to an acceptor (Ac), resulting in the formation of a reduced acceptor (Ac^-) and an oxidized donor (D^+), see Figure 3b.[57] Whether this process is thermodynamically feasible is primarily determined by the redox potentials of the species involved.[57,58] Similarly, electron transfer can also occur from a donor in a reduced state to an acceptor.

In such cases, the transferred electron originates from the highest-energy occupied orbital of the donor species.[58]

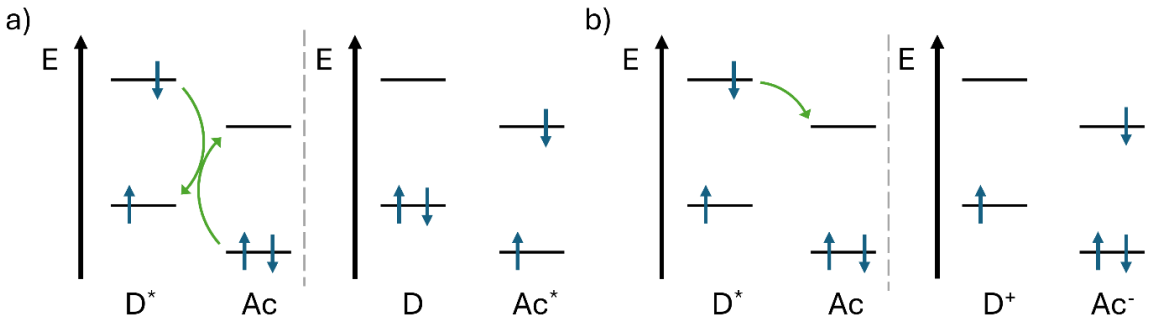

Figure 3: Simplified scheme of a) the Förster resonance energy transfer (FRET) which is based on dipole-dipole interactions Δμ and b) oxidative electron transfer.

The Z-scheme shown in Figure 2 illustrates that photosynthesis is a complex multistep process involving tightly coordinated light-induced energy- and electron-transfer reactions. Despite this complexity, natural photosynthesis operates as a robust and efficient system for the conversion of solar energy into chemical energy while simultaneously enabling CO_2 fixation. This demonstrates that biological systems can serve as valuable models for the development of artificial and biomimetic approaches aimed at sustainable energy conversion and storage.

1.3 Hydrogen evolving systems in nature

In nature, two classes of enzymes are known to catalyze hydrogen evolution: nitrogenases and hydrogenases.[59,60] These enzymes occur in various anaerobic microorganisms, as well as in some aerobic bacteria and green algae.[59,60] Nitrogenases produce H_2 irreversibly as a by-product during nitrogen fixation under anaerobic and nitrogen-limited conditions.[59] In contrast, hydrogenases catalyze the reversible formation and oxidation of H_2 under mild conditions, typically at neutral pH and ambient temperature.[60] Many hydrogenases operate in aqueous media and are characterized by low activation barriers as well as high turnover numbers and turnover frequencies (TONs and TOFs; see chapter 1.5).[60] In green algae, the light-dependent reactions of photosynthesis proceed as described in chapter 1.2.[61] Under suitable conditions, electrons generated in Photosystem I are transferred via ferredoxin to hydrogenase, which catalyzes proton

reduction to molecular hydrogen.[61] In this way, biological light harvesting can be directly coupled to enzymatic hydrogen evolution.

Hydrogenases are generally classified into three major groups: [FeFe]-, [NiFe]-, and [Fe]-hydrogenases.[60] These classes differ with respect to the metal composition of their active sites, molecular weight, electron-carrier specificity, cellular localization, and their tolerance toward heat and oxygen.[60,62] Despite these differences, all hydrogenases catalyze reactions involving molecular hydrogen under mild conditions.

A common structural feature of these enzymes is the presence of transition-metal-containing active sites embedded in a sulfur-rich protein environment.[60] In [FeFe]- and [NiFe]-hydrogenases in particular, the active sites contain iron coordinated by sulfur ligands, including acid-labile sulfur atoms in associated iron-sulfur clusters, which are essential for electron transfer and catalytic activity.[63]

[FeFe]-hydrogenases are the most catalytically active members of the hydrogenase family and are found in bacteria and lower eukaryotes. Their active site, the so-called H-cluster, consists of a [Fe_4S_4] cubane cluster that is covalently linked via a cysteine thiolate ligand to a dinuclear [Fe_2] subsite.[64] The latter serves as the catalytic center.

Within this [Fe_2] subsite, the two iron atoms fulfill distinct functions during catalysis. The distal iron center (Fe^d) is considered the primary site for substrate binding and catalysis, as it provides an open coordination site that can accommodate hydrogenic intermediates such as hydrides.[65] In contrast, the proximal iron center (Fe^p) is more tightly coordinated and mainly contributes to the structural and electronic stabilization of the active site.[65] In addition, the amine functionality of the bridging azadithiolate ligand is thought to act as a proton relay, thereby facilitating proton transfer between the H-cluster and the surrounding protein environment.[64]

The active sites of the other hydrogenase classes are structurally distinct. [NiFe]-hydrogenases contain a redox-active $Ni(S\text{-}Cys)_4$ center, in which two cysteine thiolate ligands bridge to a $Fe^2(CN)_2(CO)$ fragment that is generally considered redox-inactive under catalytic conditions.[66] In contrast, [Fe]-hydrogenases possess a mononuclear iron center.[67]

A major structural difference between [Fe]-hydrogenases and the other two classes is the absence of additional iron-sulfur clusters, which is associated with a lower oxygen sensitivity compared with [FeFe]- and [NiFe]-hydrogenases.[62,67] Nevertheless, cysteine-derived sulfur ligands are also present in [Fe]-hydrogenases, underlining the general importance of sulfur coordination and transition-metal centers in biological hydrogen conversion.[67]

The other enzyme class, nitrogenase, is more closely related to the subject of the present work. Its active site contains the FeMo cofactor ([FeMoco]), a [$MoFe_7S_9X$]-homocitrate cluster in which X can be C, N, or O.[68] Alternative nitrogenases contain vanadium or iron in place of molybdenum at this position.[68,69] The FeMo cofactor provides the catalytic site for dinitrogen reduction to ammonia and is also responsible for the accompanying hydrogen-evolution side reaction.[69]

Structurally, the cofactor consists of a sulfur-rich metal cluster in which bridging sulfide ligands and an interstitial μ_6-carbide connect the [$MoFe_3S_3$] and [Fe_4S_3] subclusters.[68,69] In addition, the Mo^{IV} center is coordinated by a homocitrate ligand, which completes its coordination environment.[69] Under molybdenum-deficient conditions, some organisms express alternative nitrogenases containing vanadium or iron instead of molybdenum.[70,71] This observation highlights the central role of molybdenum in the most common nitrogenase system, while also underlining the structural importance of sulfur ligands within the cofactor framework.

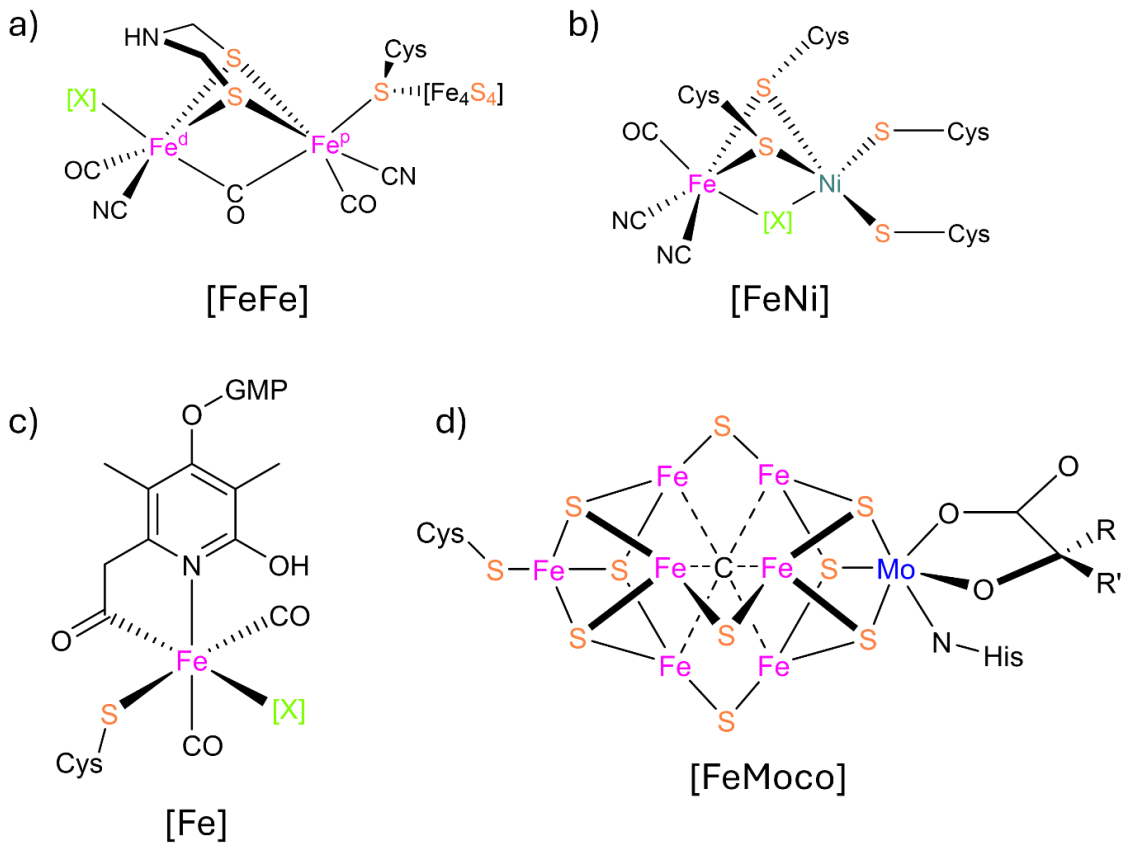

Figure 4: Chemical structure of a) [FeFe]-, b) [FeNi]- and c) [Fe]-hydrogenase as well as the [FeMoco] nitrogenase where R and R' represent the rest of the homocitrate. GMP stands for nucleotide guanidine monophosphate.

1.4 Hydrogen evolution reaction

The hydrogen evolution reaction (HER) refers to the reduction of protons to molecular hydrogen. In catalytic hydrogen evolution, a general distinction can be made between homogeneous and heterogeneous systems.[72] In addition, HER can be driven by different forms of energy input, most commonly in electrocatalytic or photocatalytic approaches. In some cases, both concepts are combined in photoelectrocatalytic systems.[72,73] Since the present work focuses exclusively on photocatalytic hydrogen evolution, only this approach is discussed in the following.

Photocatalysis uses light as the energy input to drive a chemical reaction. As in natural photosynthesis (see chapter 1.2), each component in a photocatalytic system fulfills a distinct function within the overall process. At least three components are required for a

photocatalytic HER system: a sacrificial electron donor (SED), a photosensitizer (PS), and a catalyst (CAT).[74] The photosensitizer absorbs electromagnetic radiation and converts it into excited-state energy, which enables electron transfer within the system. The catalyst serves as the active site at which proton reduction takes place. The sacrificial electron donor provides electrons to regenerate the photoactive system and thereby sustains continuous hydrogen evolution.

The interplay between these three components can be illustrated by a simplified reaction scheme (Figure 5).

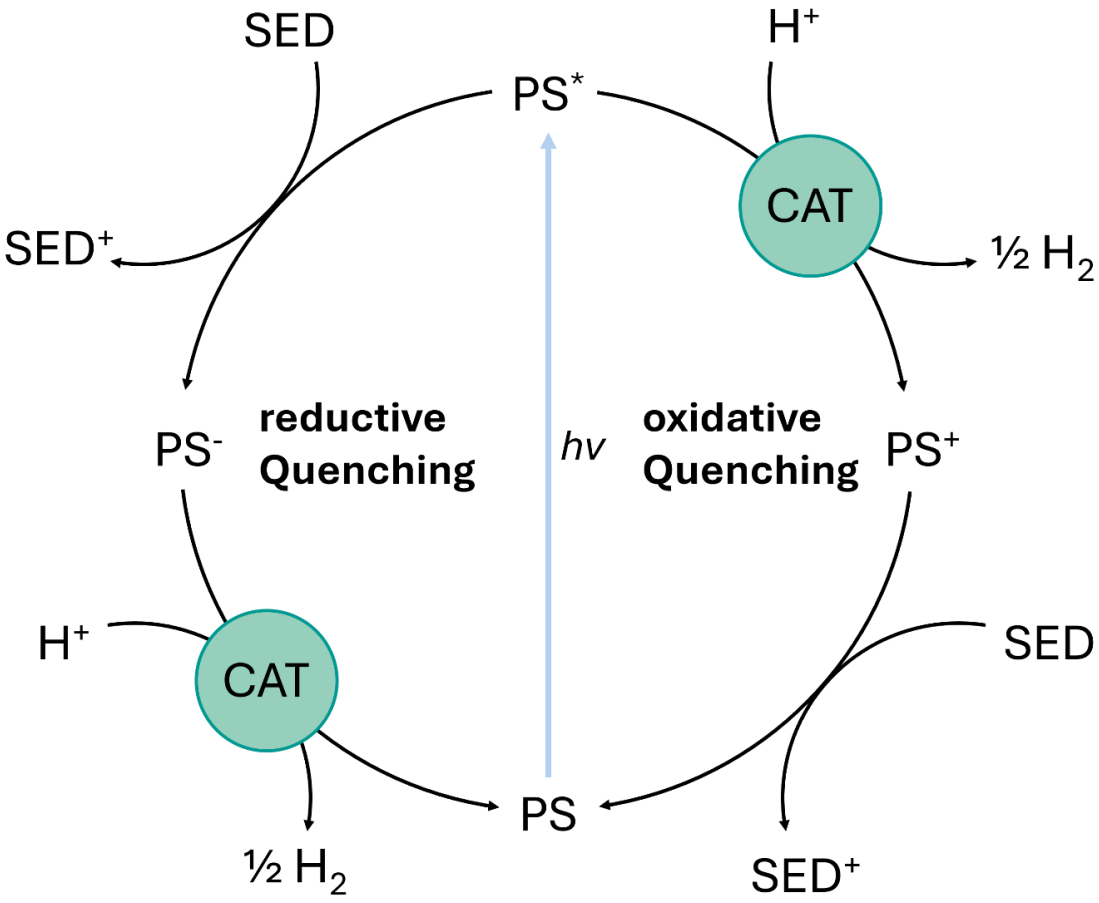

Figure 5: Simplified scheme of the photocatalytic HER showing the reductive and oxidative quenching pathways of the PS and the roles of the individual components of the system.

First, the PS is excited by absorption of a photon of suitable wavelength, forming PS*. From this excited state, two principal quenching pathways are possible: reductive quenching and oxidative quenching.[75–77]

In the reductive quenching pathway, PS* is reduced by the SED, generating the reduced photosensitizer PS^-.[75,76] This reduced species subsequently transfers an electron to the catalyst.[75,76] Through repeated electron-transfer and protonation steps at the catalyst, molecular hydrogen is formed, while the ground-state photosensitizer is regenerated.[75,76]

In the oxidative quenching pathway, the order of electron-transfer steps is reversed. In this case, the excited photosensitizer first transfers an electron to the catalyst, resulting in the formation of the oxidized photosensitizer PS^+.[75,76] The catalyst can then use the transferred electron for proton reduction.[75,76] Subsequently, the SED regenerates the ground-state photosensitizer by reducing PS^+.[75,76]

However, this catalytic cycle only describes the overall picture of light-driven HER and illustrates how the absorbed photon energy is transferred through the system to enable proton reduction. The actual HER takes place at the active sites of the catalyst. In general, HER at the catalyst is described via elementary reaction steps involving adsorbed hydrogen intermediates.

The first step is commonly described by the Volmer reaction. In this step, a proton is adsorbed at a catalytic binding site (*), while an electron is transferred to the proton, leading to the formation of an adsorbed hydrogen intermediate (H*) on the catalyst surface (Equation 1).[72,78] The ability of the catalyst to bind hydrogen is a key parameter governing catalytic performance. According to the Sabatier principle, the interaction between the catalyst and hydrogen should be neither too strong nor too weak.[79] Ideally, the Gibbs free energy of hydrogen adsorption should therefore be close to zero ($\Delta G_{H^*} \approx 0$) for efficient HER catalysis.[79]

Following the Volmer step, two possible reaction pathways may occur. One possibility is the Heyrovsky reaction, which is typically favored at low H* surface coverage.[72,78] In this case, a proton-coupled electron transfer (PCET) step leads to the formation and desorption of H_2, thereby regenerating a vacant catalytic site (Equation 2). [72,78] Alternatively, at high H* surface coverage, the Tafel reaction becomes favorable.[72,78] In this pathway, two neighboring adsorbed hydrogen atoms recombine to form H_2, which subsequently desorbs from the catalyst surface (Equation 3). [72,78] Together, these elementary steps give rise to the overall HER stoichiometry (Equation 4). [72,78]

Volmer:	$H^+ + e^- + * \rightarrow H*$	(1)
Heyrovsky:	$H* + H^+ + e^- \rightarrow H_2 + *$	(2)
Tafel:	$H* + H* \rightarrow H_2 + 2\ *$	(3)
Netto:	$2\ H^+ + 2\ e^- \rightarrow H_2$	(4)

It should be noted that the Volmer-Heyrovsky-Tafel model is primarily used to describe heterogeneous or surface-based catalysis and cannot, in general, be directly applied to molecular catalytic systems.[72]

A wide range of catalysts, PSs, and SEDs have been investigated for photocatalytic HER.[80] However, not every combination gives rise to an efficient photocatalytic system. Several requirements must be fulfilled for productive hydrogen evolution to occur. As illustrated by the photocatalytic cycle shown in Figure 5, electron-transfer steps are central to the overall process. Efficient electron transfer requires not only suitable redox properties of the individual components, but also sufficiently favorable intermolecular interactions to enable productive quenching and charge transfer (compare chapter 1.2, Figure 3). The most commonly used photosensitizers and sacrificial electron donors in photocatalytic systems are introduced in the following.

1.4.1 Photosensitizers

A wide variety of chromophores can serve as photosensitizers. These include organometallic complexes as well as purely organic and purely inorganic chromophores. Whether a given chromophore is suitable for use as a photosensitizer depends on its photochemical and photophysical properties.[81] In particular, strong absorption in the visible region of the spectrum and the ability to generate reactive charge-separated excited states are highly desirable.[81–83] The photophysical properties and excited-state behavior of a chromophore can be illustrated qualitatively using a Jablonski diagram (Figure 6).

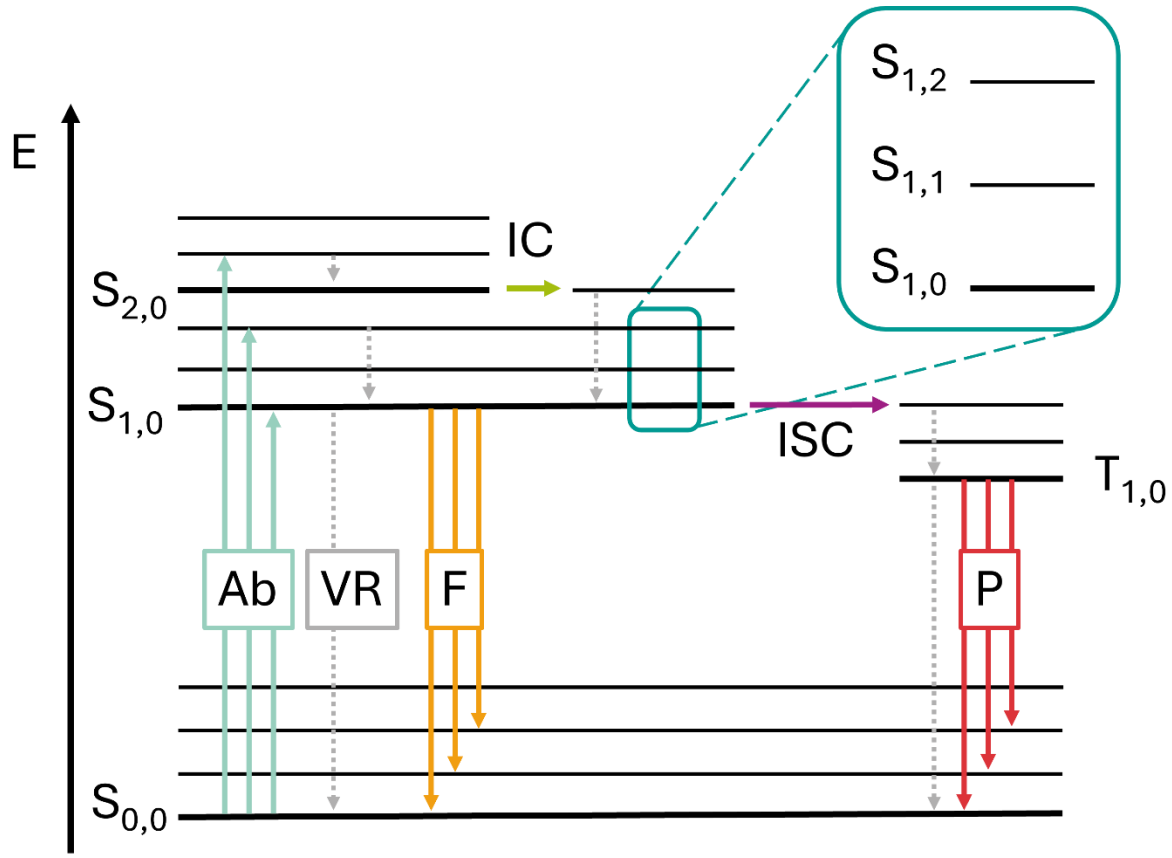

Figure 6: Simplified Jablonski diagram showing the different radiative transitions between electronic states: absorption (Ab), fluorescence (F) and phosphorescence (P) as well as the non-radiative transitions: vibrational relaxation (VR), internal conversion (IC) and inter-system crossing (ISC).

The Jablonski diagram illustrates the possible transitions between the electronic and vibrational states of a molecule. Each electronic state M_e can be subdivided into several vibrational levels $M_{e,v}$. Here, M denotes the multiplicity of the state, where S refers to a singlet state and T to a triplet state. The index e indicates the electronic state, while v denotes the vibrational level.[84]

According to the Pauli principle and Hund's rules, the electronic ground state of a closed-shell molecule is typically a singlet ground state (S_0).[85,86] When a molecule in its ground state absorbs a photon of sufficient energy, an electron is promoted from an occupied molecular orbital to an unoccupied molecular orbital of higher energy. This absorption process occurs on an ultrafast timescale of approximately 10^{-15} s. As a result, the molecule is transferred into an electronically excited state such as $S_{1,v}$, $S_{2,v}$, or higher excited states.[84]

The Franck-Condon principle describes that electronic excitation occurs much faster than nuclear motion.[87] Therefore, the transition initially populates a vibrational level of the excited electronic state that is accessible without significant change in nuclear geometry. Subsequently, the molecule relaxes to the lowest vibrational level of that excited state by vibrational relaxation (VR). According to Kasha's rule, photophysical and photochemical processes generally occur from the lowest vibrational state of a given electronic state.[88] Vibrational relaxation is a non-radiative process and typically takes place on a timescale of about 10^{-12} s.[84]

Deactivation of an excited state can proceed through several pathways. One possibility is internal conversion (IC), a non-radiative transition between electronic states of the same multiplicity, in which excess electronic energy is converted into vibrational energy. Another possible pathway is inter-system crossing (ISC), in which the multiplicity changes, for example from a singlet to a triplet state. Since ISC is spin-forbidden, it is generally less probable than IC, although its efficiency strongly depends on the molecular structure and the presence of spin-orbit coupling. Both IC and ISC are non-radiative deactivation processes.[84]

In addition to these non-radiative pathways, excited states may also decay radiatively by luminescence. Radiative relaxation from an excited state to a ground state of the same multiplicity is called fluorescence (F). For many organic molecules, fluorescence from an excited singlet state typically occurs on a timescale of about 10^{-9} to 10^{-8} s. In contrast, phosphorescence originates from an excited triplet state and involves a change in multiplicity. Because this transition is spin-forbidden, phosphorescence (P) is generally much slower and excited triplet-state lifetimes can range from approximately 10^{-3} s up to seconds, depending on the system.[84]

The lifetimes of excited states are of central importance for the application of chromophores in photocatalytic systems, since sufficiently long-lived excited states are required to enable productive energy- and electron-transfer processes.

One of the most widely studied and best-known photosensitizers is tris(2,2'-bipyridine)ruthenium(II), $[Ru(bpy)_3]^{2+}$. The complex was first synthesized by Burstall in 1936.[89] Its first absorption spectrum was reported in 1949,[90] followed by the

first emission spectrum in 1959.[91] The latter triggered research into the photophysical properties of the complex. During the late 1960s and 1970s, $[Ru(bpy)_3]^{2+}$ was investigated in increasing detail, particularly with regard to energy- and electron-transfer processes.[92] Early studies on light-driven hydrogen evolution using $[Ru(bpy)_3]^{2+}$ as a photosensitizer were later reported by Creutz and co-workers.[93]

Today, $[Ru(bpy)_3]^{2+}$ is widely used as a benchmark photosensitizer in fields such as photochemistry, photoelectrochemistry, photophysics, photoredox catalysis, and biochemical research. Owing to its broad applicability and thoroughly characterized properties, it has become one of the most important reference compounds in molecular photocatalysis.[92]

The success of $[Ru(bpy)_3]^{2+}$ as a photosensitizer can be attributed to several favorable properties. As discussed above, the lifetime of an excited state is a key parameter in photocatalysis. In this regard, $[Ru(bpy)_3]^{2+}$ exhibits an excited-state lifetime of approximately 600 ns for its triplet metal-to-ligand charge-transfer state (^{3}MLCT), depending on the solvent and the presence of oxygen[82,93–95]. The corresponding absorption band is centered around 452 nm and therefore lies in the visible region of the spectrum.[90] This greatly facilitates its application in photocatalysis, since readily available blue LEDs can be used instead of UV light sources.

In addition, the electrochemical properties of $[Ru(bpy)_3]^{2+}$ have been studied extensively. Depending on the redox properties of the sacrificial electron donor or other quenchers present in the system, the excited state can undergo either oxidative or reductive quenching.[93] The oxidized form, $[Ru(bpy)_3]^{3+}$, exhibits a redox potential of +1.26 V vs. the normal hydrogen electrode (NHE) and therefore acts as a strong oxidant, whereas the reduced form, $[Ru(bpy)_3]^{+}$, has a redox potential of −1.28 V vs. NHE and acts as a strong reductant.[96] These electrochemical properties make $[Ru(bpy)_3]^{2+}$ suitable for a wide range of photocatalytic applications, including hydrogen evolution and, in principle, also water oxidation.[93,96]

Despite these advantages, $[Ru(bpy)_3]^{2+}$ is not immune to degradation processes. Various decomposition pathways have been described in the literature, and their occurrence depends strongly on factors such as solvent, pH, irradiation conditions, and the nature of

the other components in the system. Photobleaching is one of the most common degradation pathways of chromophores. In the case of $[Ru(bpy)_3]^{2+}$, photodegradation is often associated with Ru–N bond cleavage. Upon irradiation and population of excited states, antibonding orbitals can become involved, which weakens the Ru–N bond and may ultimately lead to ligand dissociation. As a consequence, the vacant coordination site can be occupied by other ligands such as aqua, hydroxo or chloro ligands. [97–102]

Other photosensitizers frequently used in photocatalysis include dendrimers,[103] metalloporphyrins,[104] metallophthalocyanines,[105] and organic dyes such as Eosin Y.[106] Metal-free chromophores are often characterized by extended π-conjugated systems, whereas many metal-containing coordination compounds exhibit charge-transfer excited states, such as metal-to-ligand charge transfer (MLCT), that are beneficial for photocatalytic applications. [91,93] The photophysical properties of such dyes can often be tuned effectively through structural modification of the aromatic ligand framework. However, excessive steric hindrance at the ligand periphery may limit this tunability, as it can reduce orbital overlap and thereby impair electron-transfer processes.[107–109] In heterogeneous photocatalytic systems, semiconducting materials such as titanium dioxide (TiO_2),[110] quantum dots (e.g., CdSe),[111] and conjugated polymers are also commonly employed.[112]

1.4.2 Sacrificial electron donors

Another essential component of a photocatalytic system is the SED. Its function is to regenerate the oxidized photosensitizer (PS^+) and, depending on the reaction pathway, to reductively quench the excited photosensitizer (PS*). To fulfill this role, the SED must be readily oxidizable and able to provide the required electrons efficiently. Ideally, its oxidation products should be chemically inert in order to suppress charge recombination and avoid competing side reactions. Since the SED is consumed during the catalytic cycle and is not regenerated, it inherently limits the long-term sustainability of the system.[113]

In aqueous photocatalytic systems, the redox potential of the electron donor is of particular importance. The donor must be oxidized more readily than water in order to suppress competing water oxidation. Commonly used sacrificial electron donors in such systems include triethylamine (TEA), triethanolamine (TEOA), ethylenediaminetetraacetic

acid (EDTA), and ascorbic acid/ascorbate (AscH/Asc). Their redox behavior strongly depends on pH. For TEA and TEOA, the most suitable pH range is typically close to their pKa values, since excessive protonation reduces their electron-donating ability. EDTA is frequently employed in near-neutral systems, whereas ascorbate-based donor systems are particularly effective under mildly acidic to neutral conditions, where deprotonated ascorbate acts as the more readily oxidizable species.[113–115]

1.4.3 Homogeneous vs. heterogeneous

Catalysis can generally be carried out either homogeneously or heterogeneously. Homogeneous catalysis refers to systems in which all components are present in the same phase, typically in solution. In such systems, catalysis occurs at the molecular level. The individual components are usually well defined, and their structures are often known in detail. This allows mechanistic investigations at the molecular scale and often results in high selectivity.[116,117]

At the same time, the elementary steps in homogeneous catalytic systems are frequently diffusion-controlled. Productive electron transfer requires that the relevant molecular components encounter each other under suitable conditions, which can limit the overall efficiency of the system.[118] A major disadvantage of homogeneous catalysis is the difficulty of catalyst recovery and recycling. Because all components are present in the same phase, their separation is often challenging, making purification and reuse comparatively expensive.[119] One of the first molecular model systems for light-driven hydrogen evolution catalysis (HEC) was reported by Lehn, Sauvage, and co-workers in 1977.[120] Since then, numerous homogeneous systems for light-driven hydrogen evolution have been developed.[76]

Heterogeneous systems (components in different phases: e.g. solid/gaseous, solid/liquid) on the other hand are often easier to recover because the individual components can be separated more readily and reused. In many cases, heterogeneous catalysts are also more robust and thermally stable than their molecular counterparts. These features are among the main reasons why heterogeneous catalysis is widely applied in industrial processes.[121–123]

A disadvantage of heterogeneous systems is that the active sites are often unevenly distributed and less well defined than in molecular systems, since their local coordination environment cannot usually be characterized with the same precision. In addition, the catalytic reaction is restricted to the catalyst surface. As a result, the accessible surface area strongly influences the reaction rate, making surface maximization a key factor in catalyst design.[123,124]

1.5 Performance, stability and reactivity in photocatalysis

The photocatalytic performance, stability, and reactivity of a system can be assessed using experimental performance metrics. To enable meaningful comparison between different systems, unbiased, reliable and reproducible evaluation is essential. This requires well-defined experimental protocols, standardized reaction setups, and clearly accessible performance indicators. In addition, transparent reporting and structured data handling are necessary to ensure that experimental results can be compared, reproduced, and reused effectively. In this context, the FAIR principles—findable, accessible, interoperable, and reusable—provide an important framework for the management and dissemination of scientific data, particularly with regard to automated and data-driven analysis.[125,126]

A wide range of parameters can individually influence the performance, stability, and reactivity of a photocatalytic system. Some of these factors are commonly investigated, including pH, sacrificial agents, photosensitizers, solvents, and concentration effects, whereas others are often neglected, such as temperature and mass transport, ionic strength, and in the case of photocatalysis also reactor design or the mode of reactor operation.[126] Since a comprehensive discussion of all relevant parameters would be beyond the scope of this chapter, only those factors that are directly relevant to the present work are discussed in the following.

The **concentrations of the individual components, as well as their relative ratios,** have a major influence on photochemical reactivity. Even small changes in these parameters can shift a system from virtually inactive to highly reactive.[127,128] This strong dependence arises from the complex interplay between the components and the underlying reaction mechanisms. A detailed understanding of these relationships is therefore essential for the rational optimization of photocatalytic systems.[129,130]

The **solvent** influences the solubility, stability, and intermolecular interactions of the individual components. In addition, it can participate directly in the reaction, for example as a reagent or as a coordinating species. In some systems, the solvent may also interfere with photoredox processes if it is able to act as an electron donor or acceptor.[131,132]

Intermolecular and supramolecular interactions represent particularly important challenges in homogeneous systems. Depending on their nature, these interactions can either promote or impair the reactivity and stability of the photocatalytic system. Relevant interactions include electrostatic interactions, van der Waals forces, π-π stacking, and hydrogen bonding. In addition, host-guest complex formation may influence the system by inducing aggregation of molecular components in solution.[133,134] Such interactions can have both beneficial and detrimental consequences. For example, pre-organization or pre-aggregation of the components may facilitate and accelerate charge-transfer processes.[135] In contrast, unfavorable aggregation can lead to colloid formation, precipitation, [129] or rapid charge recombination.[97] These effects reduce the number of catalytically active species in solution and thereby limit the overall reactivity of the system.[126]

Another important challenge in homogeneous systems is the **matching of kinetic rates**. The individual mechanistic steps of photocatalysis occur on very different timescales, ranging from femtoseconds to milliseconds and beyond.[136] The alignment of these timescales is crucial for efficient catalysis.[137,138] Reaction conditions can be adjusted to bring the relevant processes into a productive balance. For example, diffusion-controlled steps are influenced by temperature, reagent concentration, and solvent viscosity.[138] In many cases, the timescale of such diffusion-controlled processes must be matched to the lifetime of the photoexcited photosensitizer in order to enable efficient oxidative or reductive quenching by an electron donor or acceptor.[93,139] The excited-state lifetime itself is also affected by reaction conditions, for example by solvent polarity.[139]

As described above, photons provide the electromagnetic energy required to drive a photocatalytic reaction.[126] In this sense, light can be regarded as an additional reagent that has a direct influence on the system. The **incident photon flux** describes the number of photons reaching the reaction vessel per unit time and thus provides an essential basis for the quantitative interpretation of light-driven catalytic reactivity data.[140,141] It is

determined by factors such as the light source, the optical path, the irradiation geometry, and the design of the reactor walls.[142,143] Consequently, a detailed description of the irradiation setup and its geometry is crucial to ensure the reproducibility and comparability of photocatalytic data.[126]

Another important parameter is the **absorbed photon flux**. It describes how many photons of the incident photon flux can be absorbed by the system and are in principle available for the catalytic process.[141]

The influence of **photoreactor design** has already been addressed in part in the context of the incident photon flux. However, reactor design affects not only the distribution of light within the system, but also the local reaction environment. In this context, factors such as non-ideal mixing, dead zones, and residence time distributions must also be considered. [144]

To evaluate the influence of the parameters discussed above, performance indicators are used. These metrics provide critical information on catalytic activity and enable comparison between different systems. Depending on the purpose of the analysis, they can be normalized to catalyst amount, reaction time, or photon input. One of the most widely used amount-normalized performance indicators is the turnover number (TON).[126] It is defined as the amount of product formed, n_{Pro}, divided by the amount of catalyst used, n_{Cat}.

$$TON = \frac{n_{Pro}}{n_{Cat}} \quad (5)$$

The time-dependent analogue of the TON is the turnover frequency (TOF).[126] It describes the change in TON over time. When determined over a finite time interval, TOF corresponds to the average change in TON divided by the corresponding reaction time interval:

$$TOF = \frac{\Delta TON}{\Delta t} \quad (6)$$

The photon-based analogue is given by the photonic efficiency (PE).[126] In this case, the amount of product formed n_{Pro} is normalized to the amount of incident photons $n_{Ph,inc}$.

$$PE = \frac{n_{Pro}}{n_{Ph,inc}} \quad (7)$$

Another photon-based performance indicator is the quantum yield (Φ). In contrast to the indicators introduced above the quantum yield is not limited to product formation. Instead, it can also be used to relate the occurrence of a specific event, n_{Event}, such as molecular degradation, to the number of photons absorbed by the system, $n_{Ph,abs}$.[145]

$$\Phi = \frac{n_{Event}}{n_{Ph,abs}} \quad (8)$$

1.6 Thiomolybdates and thio-oxo-molybdates

As noble-metal-free catalysts for the HER, thiomolybdates have attracted considerable attention over the past decades.[72] This interest has been motivated in part by the active sites of hydrogenases and nitrogenase (see chapter 1.3), which contain sulfur-rich transition-metal clusters. Inspired by these biological systems, research into (poly)thiomolybdates has expanded significantly.[72] The first studies on two prototype thiomolybdate anions were reported by Müller and co-workers in the late 1970s.[146] These prototype species were the dinuclear cluster $[Mo^{+5}_2S_{12}]^{2-}$ (**{Mo₂}**) and the trinuclear cluster $[Mo^{+4}_3S_{13}]^{2-}$ (**{Mo₃}**) both isolated as ammonium salts.[146,147] Their synthetic approach has remained essentially unchanged to this day. The clusters are formed in the reduction of Mo^{+6}, typically starting from ammonium heptamolybdate ($(NH_4)_6[Mo_7O_{24}]$), in aqueous solutions containing sulfide or polysulfide species.[146,147] The resulting crystalline products can subsequently be isolated.

Structurally, these two prototype clusters share several common features. The Mo centers are coordinated by one or two terminal disulfide ligands and by two bridging disulfide ligands, S_2^{2-} and μ_2-S_2^{2-}, respectively. In the **{Mo₃}** cluster, an additional apical sulfide ligand (μ_3-S^{2-}) coordinates the three molybdenum centers.[146,147]

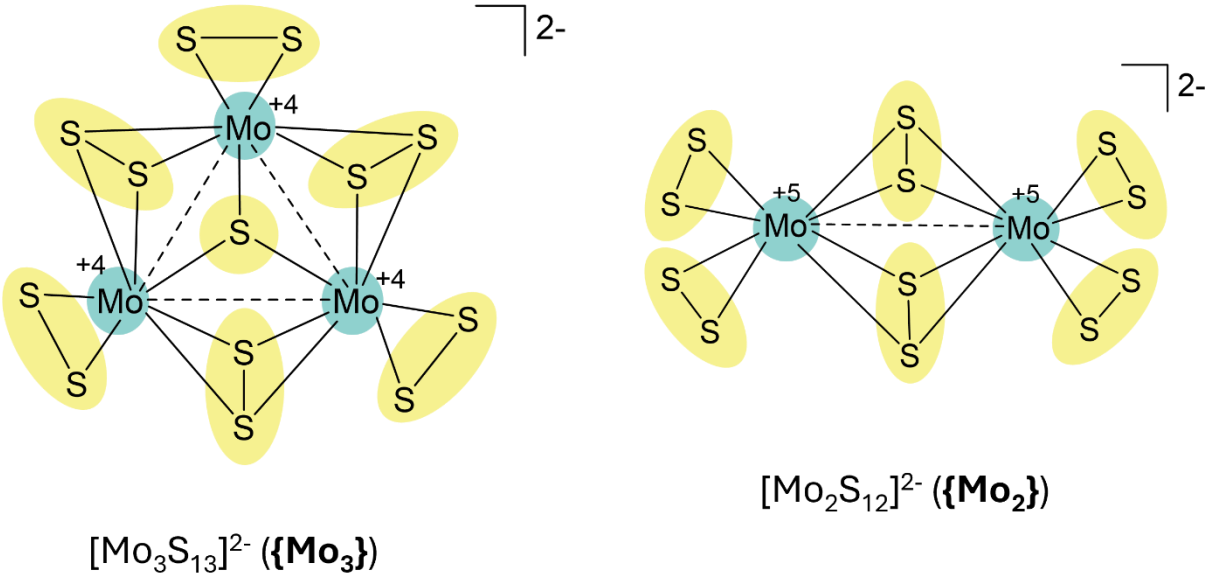

*Figure 7: Chemical structure of the thiomolybdates **{Mo₃}** (left) and **{Mo₂}** (right).*

Both homogeneous and heterogeneous approaches to light-driven HEC with thiomolybdates have been investigated and discussed in the literature.[72] Since the present work focuses exclusively on homogeneous catalysis, only this approach is introduced further in this chapter.

Initial mechanistic studies on homogeneous light-driven HER systems based on thiomolybdates revealed a pronounced sensitivity to sample preparation and reaction conditions.[127,148] Catalytic performance was found to depend strongly on the solvent, and different solvents proved to be optimal for the individual prototype clusters. Owing to its suitable redox properties, the photosensitizer $[Ru(bpy)_3]^{2+}$ is most commonly employed in combination with thiomolybdates.[116, 127,148] Accordingly, irradiation with blue light is typically used to drive catalysis.

Min and co-workers investigated the **{Mo₃}** cluster in combination with alternative photosensitizers, including Eosin Y, and found that replacing $[Ru(bpy)_3]^{2+}$ resulted in a complete loss of hydrogen-evolution activity. In the same study, various sacrificial electron donors, such as organic amines and organic carboxylic acids, were also examined. Among these, ascorbic acid proved to be a particularly suitable sacrificial electron donor. One possible explanation for this behavior may lie in its additional proton-donating ability. [149]

The concentrations of thiomolybdate catalysts are typically kept in the sub-micromolar range, since higher concentrations can promote aggregation and colloid formation with

the photosensitizer. Under these conditions, photosensitizer concentrations of around 20 µM are generally sufficient to sustain catalysis.[127,148] Although higher photosensitizer concentrations are often employed in other transition-metal-based systems, in thiomolybdate-based systems such concentrations are frequently limited by solvent effects and aggregation phenomena.[102,129]

Streb and co-workers reported that the **{Mo$_3$}** system can achieve turnover numbers (TONs) exceeding 20 000 after 6 h of irradiation and 40 000 after 24 h of continuous irradiation under optimized conditions. The highest TON values were obtained in a methanol/water solvent mixture (10:1, v:v). In addition, degradation pathways of the cluster were investigated by Raman spectroscopy, which was used to monitor the proposed exchange of terminal disulfide ligands by water (Figure 8). Combined catalytic studies and theoretical calculations indicated that the catalytic activity depends on the number of exchanged ligands. Notably, the most active species was proposed not to be the original model cluster itself, but rather a ligand-exchanged derivative.[148]

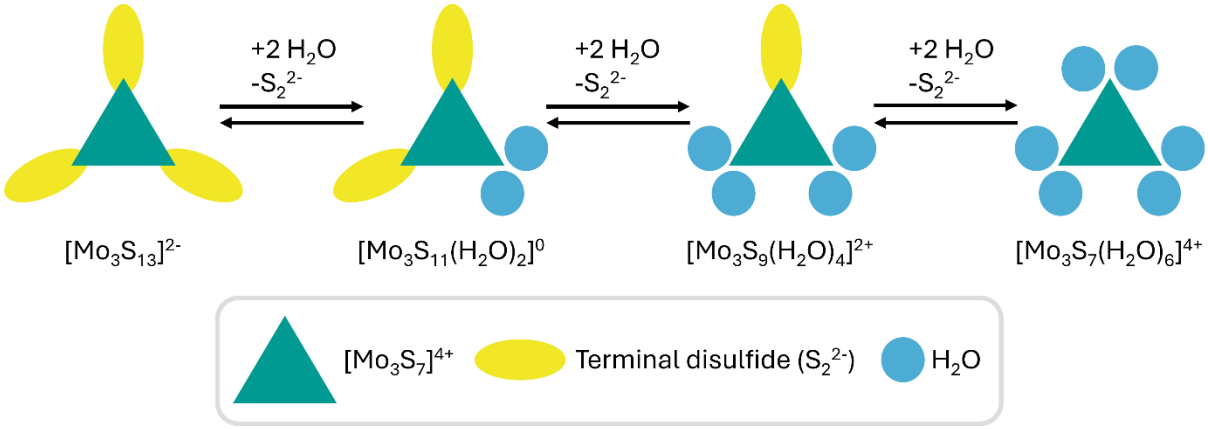

Figure 8: Schematic visualization of the terminal disulfide exchange against water molecules reported by Dave et al.[148]

In a separate study, further enhancement of HER performance was achieved by addition of NH_4^+ to the catalytic system. It was suggested that ammonium either prolongs the lifetime of the excited photosensitizer (PS*) or facilitates intermolecular, collision-induced proton-coupled electron-transfer (PCET) processes. In this context, NH_4^+ may contribute to proton management through additional hydrogen-bonding interactions during catalysis.[150]

The smaller thiomolybdate cluster **{Mo_2}** was also investigated by Streb and co-workers. In homogeneous catalysis, the system reached a TON of 1600 after 6 h of irradiation in pure methanol. Interestingly, the catalytic activity decreased with increasing water content in the solvent mixture. Emission-quenching studies showed that quenching of $[Ru(bpy)_3]^{2+}$ by the cluster becomes less efficient as the water content of the solvent increases.[127]

A possible ligand-exchange process, similar to that proposed for the **{Mo_3}** cluster, was also investigated for **{Mo_2}**. Raman spectroscopy was again used to monitor potential structural changes. No changes were observed over the course of two hours, and evidence for ligand exchange was only obtained after prolonged reaction times. These findings suggest that the **{Mo_2}** cluster is more stable than the **{Mo_3}** cluster under the conditions investigated. The loss of catalytic activity in the **{Mo_2}** system was mainly attributed to degradation of PS. Accordingly, HER activity could be restored by addition of a second aliquot of PS.[127]

In addition to thiomolybdates, other Mo-S-based molecular compound classes have attracted increasing attention in recent years because of their potential as HER catalysts. One such class is thio-oxo-molybdates, in which thiomolybdate frameworks are modified by incorporation of oxygen-containing ligands. One of the smallest clusters in this group is $[Mo^{+5}_2O_2S_6]^{2-}$ cluster. In this cluster, two Mo^{+5} centers are connected by two bridging sulfide ligands (μ-S^{2-}) and are each additionally coordinated by one terminal disulfide ligand (S_2^{2-}) and an oxo ligand (O^{2-}) each (Figure 9).[72]

The synthesis of this cluster was also first reported by Müller and co-workers in 1980.[151] In a later study, Miras and colleagues investigated the HER mechanism of this and other small thio-oxo-molybdate clusters. Using electrocatalytic experiments in combination with theoretical calculations, they showed that the cluster is capable of catalyzing electrocatalytic HER and that the oxo ligand plays a crucial role in stabilizing the reduced cluster. They further proposed that the catalytic process most likely follows a Volmer-Heyrovsky-type mechanism and identified the terminal disulfide ligands as the active sites of the cluster. [152]

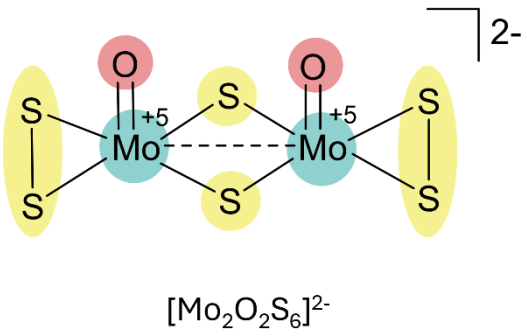

Figure 9: Chemical structure of the thio-oxo-molybdate $[Mo_2O_2S_6]^{2-}$.

1.7 Design of Experiments

Several parameters affecting photocatalytic systems were introduced in chapter 1.5. Traditionally, the influence of such parameters has often been investigated using a one-factor-at-a-time (OFAT) approach, in which only a single parameter is varied while all others are kept constant. The resulting changes are then interpreted individually. However, this approach is time-consuming and requires a large number of experiments to evaluate the influence of each parameter separately. In addition, interactions between individual parameters are difficult to identify using OFAT.[153,154]

A statistical design of experiments (DoE) approach provides a solution to these limitations. By varying several parameters simultaneously, the number of experiments required to identify significant effects can be reduced substantially. Moreover, statistical analysis enables the detection of interactions between parameters, thereby allowing a more comprehensive understanding of the experimental data. In addition, DoE can be used to predict optimal process conditions and thus support systematic process optimization.[153]

DoE is applied across a wide range of research fields. In chemistry and pharmaceutical research, it has already been used extensively in synthetic studies to evaluate the influence of individual reaction conditions as well as their interactions.[153]

The full potential of a DoE approach can be realized when the eight-step workflow is followed systematically:

1. **Define the objective**: Which issues occur during the process, and which of them should be addressed? In many cases, the aim is to optimize a process by varying

the experimental conditions. However, DoE can also be used to gain a deeper understanding of the process itself by identifying the effects of individual parameters, also called factors, and their interactions. [153]

2. **Definition of the factors/parameters and their ranges**: Depending on the available resources and the feasibility of varying individual reaction conditions, the factors or parameters of interest are selected. For each factor, an appropriate value range must be defined. In general, a low and a high level are chosen to cover a broad range of conditions. However, the effect of a factor does not necessarily have to be linear across this range; in such cases, it may be useful to investigate more than two levels. As each additional factor and each additional level increases the number of experiments required to analyze the system, it is important to prioritize the variables based on existing knowledge. Factors that are unlikely to have a significant influence should preferably be excluded in favor of those expected to have a stronger effect. [153]
3. **Definition of the responses**: At this stage, the measurable outcomes of the process must be defined. Multiple responses can be included without increasing the number of experiments, provided that the sample preparation is identical. The reproducibility of the experimental method is of crucial importance in order to minimize systematic errors. Therefore, experiments should be performed in triplicate. [153]
4. **Selection of the experimental design**: A variety of experimental designs can be chosen depending on the available resources and the overall objective. Two commonly used types are screening designs and optimization designs. The latter requires a larger number of experiments but provides a more comprehensive model of the system. Screening designs, in contrast, are primarily used to obtain qualitative information about the relevance of individual factors or parameters. The choice of design depends on the objective, the number of factors or parameters, their ranges or levels, and the available resources. In many cases, these resources are directly linked to the number of experiments required. For example, time is often a limiting factor; if it is scarce, a screening design is usually preferred, as it requires fewer experiments while still providing sufficient information, whereas a more complex design may demand substantially more

experimental effort for only a comparatively small additional gain in information. [153]

5. **Generating the experimental plan**: The choices made in steps 2, 3, and 4 are entered into suitable software (e.g., Minitab), which is then used to generate an experimental plan including the number and order of experiments. The experimental run order should be randomized in order to minimize and avoid systematic errors. [153]
6. **Performing the experiments and collecting the data**: The experiments are carried out in the order specified by the experimental plan. Experimental and analytical conditions should be kept as consistent as possible in order to minimize bias. [153]
7. **Data analysis**: Once all experiments have been completed and the response values for each run have been entered into the software, the data can be analyzed. The software typically determines the statistical significance of each factor or parameter as well as their interactions. Outliers can also be identified, for example based on residuals or by applying specific outlier tests. The effects of individual factors or parameters can be visualized using main effects plots, whereas interactions between factors are commonly illustrated in interaction plots. Another important parameter in data analysis is the coefficient of determination, R^2. It describes how much of the variation in the response variables is explained by the investigated factors or parameters and their interactions. A high R^2 value indicates that the selected factors account for a large proportion of the variability in the system and that only a minor part of the relevant influences have been neglected. In contrast, unmeasured or uncontrollable factors, such as fluctuations in atmospheric pressure or operator-dependent variation, may reduce the R^2 value. A low R^2 value may therefore indicate that additional relevant factors should be included in the experimental design or that the experiments were not performed with sufficient reproducibility, resulting in increased variation in the response values. Once the effects of the investigated factors, their interactions, and the R^2 value have been determined, the model can be used to predict conditions for a desired target, such as maximizing, minimizing, or achieving a specific response value. The software then predicts which combination of parameters is most likely to achieve this target and estimates the probability of success. In addition, a

confidence interval is usually provided, indicating the range within which the response values are expected to fall with a defined probability, often 95%, for experiments performed under the optimized conditions. [153,155]

8. **Confirmation of the predicted model** Since the optimized conditions suggested by the DoE analysis software represent only a model-based prediction, it is essential to verify and validate this forecast experimentally. [153]

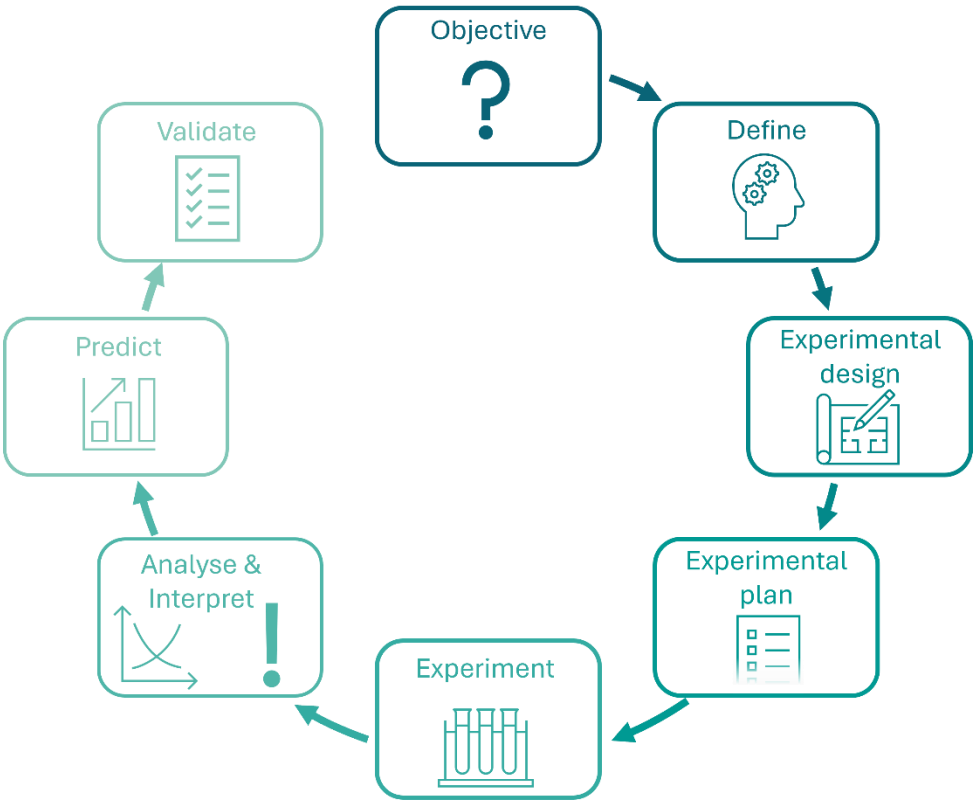

Figure 10: Schematic visualization of the DoE approach and the workflow.

2 Objective

The growing global demand for energy requires urgent solutions for low-emission or emission-free energy production in order to mitigate climate change (see chapter 1.1). In this context, green hydrogen represents a promising approach to addressing these challenges. Accordingly, the development of sustainable catalysts for hydrogen evolution is of considerable interest for future green energy technologies. Among these, thiomolybdates have attracted increasing attention in recent years as noble-metal-free and earth-abundant catalysts for the light-driven HER. However, their potential for industrial application still requires further investigation. In particular, the limitations of these systems and possible degradation pathways need to be better understood in order to improve catalyst stability and develop effective mitigation strategies. In addition, external reaction conditions such as irradiation are often neglected in studies of photocatalytic systems, not only for thiomolybdates but in photocatalysis more broadly. This neglect results in a significant knowledge gap that should not be underestimated. Furthermore, thio-oxo-molybdates may also represent promising candidates for light-driven HEC. However, this class of compounds has so far hardly been investigated or characterized in this context, leaving a substantial gap in current knowledge.

This work focuses on two major projects:

1) While internal reaction conditions such as pH, solvent, and concentration have already been investigated for homogeneous thiomolybdate systems containing **{Mo_3}** or **{Mo_2}**, the influence of irradiation has largely been neglected. Addressing this gap is the focus of the first project, which comprises one peer reviewed publication and one manuscript in preparation. The central research question is how irradiation affects the catalytic performance of these systems. In photocatalysis, irradiation is usually applied continuously. However, dynamic irradiation has not yet been systematically investigated for thiomolybdate-based systems. This dynamic approach can be divided into several key factors that can be independently controlled and varied. To obtain the maximum amount of information from the system with a limited number of experiments, a DoE approach is particularly suitable. Based on the resulting data, process optimization

can be carried out. In addition, hypotheses regarding observed trends and possible light-induced degradation pathways of the individual system components can be examined systematically, leading to a deeper understanding of the role of irradiation in these light-driven systems. Ultimately, this may open new avenues for more energy-efficient and sustainable approaches in photocatalysis.

2) Thio-oxo-molybdates have so far received only limited attention as catalysts for the light-driven HER. The second project therefore addresses the question of whether thio-oxo-molybdates are suitable catalysts for homogeneous light-driven HER and consist of one publication. To answer this question, initial studies on the catalytic performance and activity of the $[Mo_2O_2S_6]^{2-}$ cluster are carried out. Photocatalytic experiments are performed in homogeneous systems comparable to those previously described in the literature. Since ligand exchange is a known process for thiomolybdates in solution, this possible degradation pathway is also investigated. In addition, further light-induced degradation pathways are examined using a range of analytical methods. To gain deeper insight into the catalytic activity and the underlying kinetics, TD-DFT calculations are conducted and complemented by electrochemical investigations. Overall, this work provides an initial characterization of the selected thio-oxo-molybdate cluster and may contribute to the development of a new, potentially more stable alternative to thiomolybdates for the sustainable production of hydrogen.

3 Results and Discussion

In this chapter the results of the different projects carried out during this work are presented. These summaries are intended to address the research questions introduced in chapter 2.

3.1 Fewer photons, more hydrogen: effects of dynamic irradiation on light-driven hydrogen evolution by thiomolybdate catalysts

The results presented in this chapter are based on an article published under the Creative Commons Attribution 3.0 International License (CC BY 3.0). The article was published as "*Fewer photons, more hydrogen: effects of dynamic irradiation on light-driven hydrogen evolution by thiomolybdate catalysts*", S. Henriette Kolbinger, Laura Haxha, P. Charlotte Schröder, Daniel Kowalczyk, Luis Senz, Luca Schleicher, Arijit Mukherjee, Daniel Malcolm, Corinna L. Kufner, Dirk Ziegenbalg,* and Carsten Streb,* *Sustainable Energy Fuels*, **2026**, 10, 1313-1320, DOI: 10.1039/D5SE01490E. The numbering of tables, figures, equations and references was adapted for inclusion in this thesis. No other adaptations were made. The contributions of the co-authors are acknowledged after the abstract. The supporting information to the manuscript can be found directly after the manuscript's conclusion.

Abstract

Molecular molybdenum sulfide clusters such as $[Mo_3S_{13}]^{2-}$ (**{Mo_3}**) are promising earth-abundant catalysts for the light-driven hydrogen evolution reaction (HER). Their catalytic performance strongly depends on the irradiation conditions, which can influence both activity and stability. In this study, the prototype thiomolybdate **{Mo_3}** was combined with $[Ru(bpy)_3]^{2+}$ as a photosensitizer (PS) to evaluate HER performance under dynamic irradiation conditions, a combination that has not been systematically explored before. A statistical Design of Experiments (DoE) approach was applied to assess the impact of three key parameters, *i.e.*, irradiation intensity, on/off frequency, and duty cycle on the catalytic performance (assessed based on the turnover number). The results identify irradiation intensity as the main control parameter for catalytic activity, followed by duty cycle and on/off frequency. Interactions between frequency and duty cycle underline the importance of dark periods in the irradiation sequence. Optimization of the three key

parameters resulted in a 102% increase in hydrogen production compared to continuous irradiation while reducing the required energy input by 25%. Mechanistic studies provide initial insights into photosensitizer and catalyst deactivation under the given irradiation conditions. These findings highlight the potential of controlled pulsed irradiation to improve energy use in light-driven homogeneous HER.

Author Contributions:

S. H. Kolbinger	Conceptualization, methodology, investigation, formal analysis, data processing, writing original draft, visualization, discussion and revision
L. Haxha	Investigation, methodology
P. C. Schröder	Investigation, formal analysis
D. Kowalczyk	Methodology, resources, discussion and revision
L. Senz	Methodology, validation, resources
L. Schleicher	Methodology, formal analysis, computational simulations
A. Mukherjee	Investigation, discussion and revision
D. Malcolm	Investigation, methodology, visualization of computational data
C. L. Kufner	Supervision, funding acquisition, writing original draft, discussion and revision
D. Ziegenbalg*	Conceptualization, supervision, funding acquisition, writing original draft, discussion and revision
C. Streb*	Conceptualization, supervision, funding acquisition, writing original draft, discussion and revision, visualization

* Corresponding author

Motivation & introduction

Molybdenum sulfides have attracted considerable attention as earth-abundant, noble-metal-free catalysts for the HER.[156–159] Specifically, molecular molybdenum sulfide clusters, so-called thiomolybdates, have been used as molecular prototypes to study reactivity and understand the underlying mechanisms which govern HER activity and catalyst stability.[72, 116, 148,160] Specifically, the prototype thiomolybdate $[Mo_3S_{13}]^{2-}$ (=**{Mo_3}**, Figure 11) has been explored in homogeneous light-driven HER,[148,149] and the system has demonstrated remarkable turnover numbers (TONs) in the tens of thousands.[148]

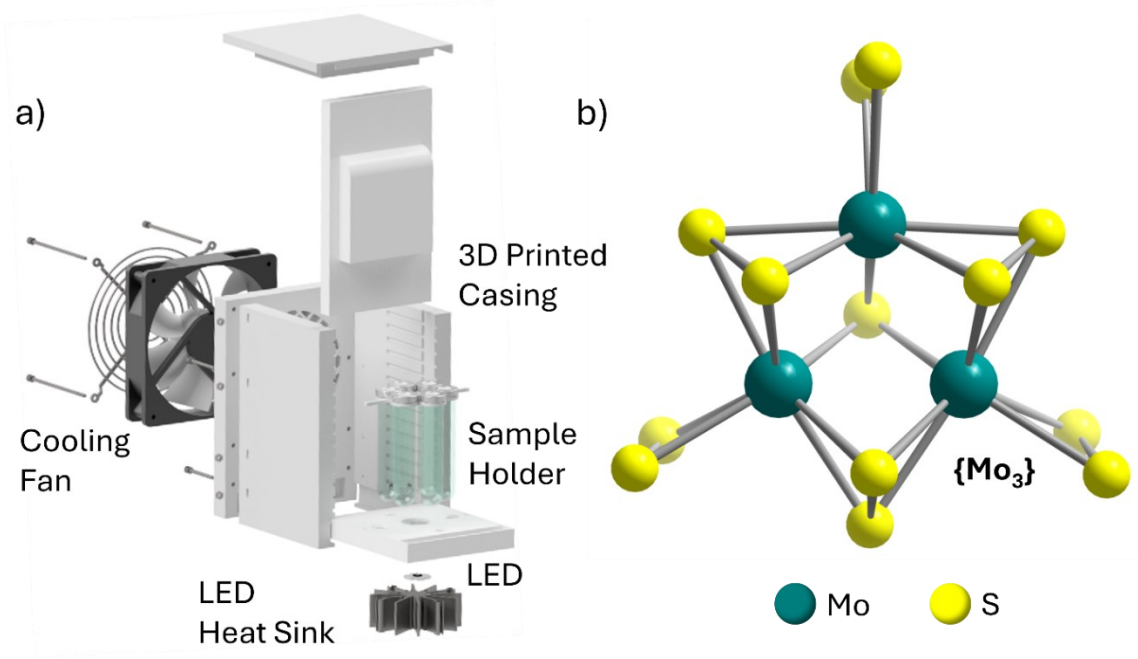

Figure 11: (a) 3D Scheme of the modular photoreactor corpus[144] and (b) illustration of the $[Mo_3S_{13}]^{2-}$ catalyst.

However, **{Mo_3}** is highly sensitive to the reaction conditions and shows highly dynamic behavior under catalytic operation.[72,148] In addition, mechanistic studies of **{Mo_3}** require precise preparation and careful experimental timing, as the cluster undergoes extensive disulfide ligand exchange reactions over time in solution, which results in time-dependent changes in HER activity, making mechanistic studies challenging.[72, 148,161]

Specifically, to-date, there is no information on the effects of irradiation on the HER performance of **{Mo_3}** (and on homogeneous HER catalysts in general). Thus, there is a

distinct knowledge gap regarding the interplay between irradiation conditions, HER performance and catalyst/photosensitizer stability.[97,126] This is despite the fact that it was recently demonstrated that dynamic irradiation of light-driven molecular catalysts can be used to control and improve catalyst stability and consequently, catalytic performance.[142] However, exploration of the complex interplay between all reaction parameters involved is far from trivial and has not been tackled in thiomolybdate catalysis or general HER catalysis to-date.

These aspects are particularly relevant for technological implementation where precise control of light exposure is essential to maximize both photocatalytic efficiency and energy utilization.[162–164] Photochemical processes, in particular, benefit from recent advances in LED technology, which allow for finetuned modulation of irradiation intensity, frequency, and pulsing.[144,165,166] Such dynamic irradiation conditions can offer new insights into the kinetics of light-driven systems and may lead to improved reaction control by identifying and selectively addressing rate-determining steps.[142]

Here, we report the influence of dynamically modulated irradiation on the light-driven HER of **{Mo_3}** when coupled with $[Ru(bpy)_3]^{2+}$ as PS. The study assesses the impact of irradiation parameters (irradiation intensity, on/off frequency, and duty cycle) on the catalytic system and uses these data to identify optimized reaction conditions and reveal key correlations between these reaction parameters.[153] A statistical DoE approach is used for these investigations since it enables the reduction of the number of experiments necessary to get all the information to a minimum and identify significant influences and correlations between parameters based on statistical analysis. In addition, combined experimental and theoretical mechanistic studies provide initial insights into the molecular processes which govern the reactivity and stability of this system.

Results and discussion

To understand the fundamental reactivity of the catalytic system under study, we first identified standard conditions (regarding solvent, reagent concentrations, acidity, etc.) which are used to comparatively assess the impact of dynamic irradiation.[154,167] This was particularly important as **{Mo_3}** reactivity is known to be dependent on the reaction parameters.[150,161] Thus, the standard system used in all measurements is based on the

thiomolybdate catalyst $(NH_4)_2[Mo_3S_{13}]$ (=$(NH_4)_2$**{Mo_3}**; *c* = 0.3 mM), $[Ru(bpy)_3](PF_6)_2$ as a photosensitizer (*c* = 20 mM) and a buffer solution of ascorbic acid/sodium ascorbate (pH = 4) as a sacrificial electron donor (SED; *c* = 10 mM) in a methanol : water mixture (9 : 1, v : v). The reaction mixture was irradiated with a monochromatic LED at λ_{max} = 465 nm.[150] Irradiation was performed in a custom-built 3D-printed modular photoreactor with 6 positions, which enables standardized, reproducible irradiation, thus limiting the impact of experimental error.[144] In addition, the system can be used to introduce dynamic irradiation while maintaining all other reactor parameters (irradiation geometry, *etc*.). Note that the reaction mixtures were not stirred as this led to reduced photocatalytic performance in this reactor type as reported previously.[144]

Static irradiation with an LED driver current of 700 mA was chosen as a standard irradiation setting, as this corresponds to an average photon fluence rate rate of 51 nmol s^{-1} cm^{-2}. To ensure comparability, the light power was determined for each of the six individual sample positions of the photoreactor (Figure 11, for details see the SI). Note that in the following, only the respective LED driver current will be given instead of the light power for clarity and brevity.

Hydrogen evolution was measured after 5 h of static irradiation by gas chromatography for three different sample positions, and the corresponding TON was determined. Different sample positions were used to eliminate systematic errors due to minor differences between the irradiation conditions due to different relative positioning of the sample vial and LED.[144] The measurement was performed six times in total and the standard deviations (SDs) for the measurements were determined. Note that these SDs are due to possible minor leakage of H_2 through the septa and general experimental errors, *e.g*. during preparation of the catalytic samples or slight differences in irradiation intensities in the different positions. These measurements represent the standard benchmark for this work and correspond to an irradiation intensity of 700 mA, a frequency of 0 Hz and a duty cycle of 100% (Figure 12). Under these irradiation settings a TON of 670 ± 140 was determined.

DoE for dynamic irradiation

With the catalytic benchmark under static conditions established, further analysis of dynamic irradiation was carried out. The influence of dynamic irradiation was studied based on the three main parameters: photon fluence rate (determined from the LED current, 350 mA, 500 mA or 700 mA), LED on/off frequency (2 Hz or 50 Hz, number of full on/off cycles per second) and duty cycle (25% or 75%, on/off time ratio of the LED per cycle). A schematic diagram of the different parameter combinations of duty cycle and irradiation frequency is shown in Figure 12.

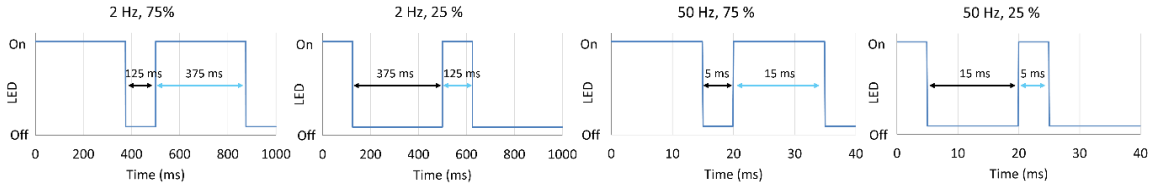

Figure 12: Detailed illustration of the on/off frequencies and duty cycle used for the experimental studies.

The simultaneous investigation of multiple parameters is challenging, as it can require a large number of experiments, particularly for identifying correlations between individual parameters. Traditionally, the one-factor-at-a-time (OFAT) model is applied to study such influences.[154,167] However, the OFAT model provides no insights into possible interactions between the individual parameters, which can lead to misinterpretation of results.[168] An alternative to address these drawbacks is the use of Design of Experiments (DoE), which we use in the present study. DoE uses a statistical approach to experiment planning and can provide insight into the impact of each parameter and possible interactions between individual parameters. Moreover, it decreases the number of experiments required to get a full overview of the interaction and correlation between individual parameters while enabling the changing of all parameters simultaneously.[153] For this work a full factorial screening design was selected to obtain a complete overview of individual influences of the parameters and their possible interactions. An experiment plan was generated using Minitab Statistical Software 22. The order of experiments was randomized. The detailed experimental plan is provided in the SI.

Each experiment was carried out in triplicate using the standard experimental conditions described above ($(NH_4)_2$**{Mo_3}**; *c* = 0.3 mM, $[Ru(bpy)_3](PF_6)_2$; *c* = 20 mM, buffer solution of

ascorbic acid/sodium ascorbate (pH = 4) as the SED; *c* = 10 mM in a methanol : water mixture 9 : 1, v : v, no stirring) as well as the respective parameter settings as outlined above. An overview of the resulting H_2 TONs is shown in Figure 13and SI, Table 8. Based on these data, and using TONs as the performance parameter, we obtained the main effect diagrams shown in Figure 13.

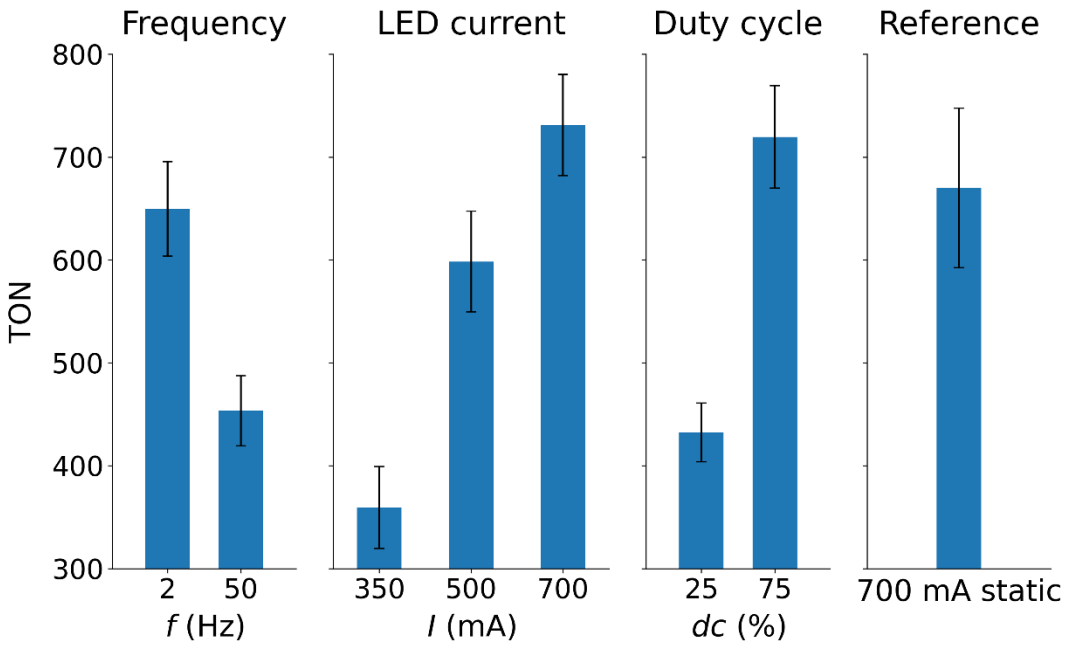

Figure 13: Main effect diagram for the individual parameters: on/off frequency, LED current and duty cycle. Plot of the average TON vs. frequency, LED current and duty cycle. The TON of the reference experiment (static conditions: 700 mA, 0 Hz, 100%) is shown for comparison. Error bars represent the standard error of the mean.

The main effect diagram can be interpreted as follows: the individual graphs show the influence of the lower vs. the higher value setting. The vertical range covered by a graph in terms of the responding parameter indicates the extent of the influence of the respective parameters. With that in mind, the main effect diagram can be interpreted. An increased frequency has a negative impact on the TON while an increased LED current and duty cycle have a positive impact. Furthermore, the LED current causes the biggest changes in the TON. This implies that the LED current and therefore light intensity have the biggest influence on the HER performance of the system, followed by the duty cycle and the on/off frequency. These results suggest that at high light power and high duty cycle, more photons are provided to the reaction, resulting in higher catalytic turnover. By contrast, the negative trend observed for frequency is less intuitive, as changing frequency

does not alter the total energy input. Further analysis is therefore needed to rationalize this observation.

One possible explanation for this observation is that exchange of the terminal disulfide ligands at **{Mo$_3$}** is photon fluence rate dependent, so that high photon fluence rates can result in increased deactivation. This hypothesis will be tested later in this work. Based on earlier work,[148] we propose that the catalyst degradation might follow a similar mechanism as discussed for the photosensitizer $[Ru(bpy)_3]^{2+}$,[98] In both cases, loss of terminal chelating ligands (**{Mo$_3$}**: S_2^{2-}; photosensitizer: bpy) requires cleavage of two coordinative bonds to result in deactivation. At low photon fluence rates this is less likely compared with high photon fluence rates, offering a plausible explanation for the photon fluence rate-dependency of deactivation. Note that the loss of these terminal ligands is expected to have a major impact on catalytic reactivity as these sites are discussed as the reactive centers for HER by **{Mo$_3$}**.[72]

In the next step, we analyzed possible interactions between the parameters which are not captured by the main effect diagram. This is visualized in interaction diagrams, see Figure 14.

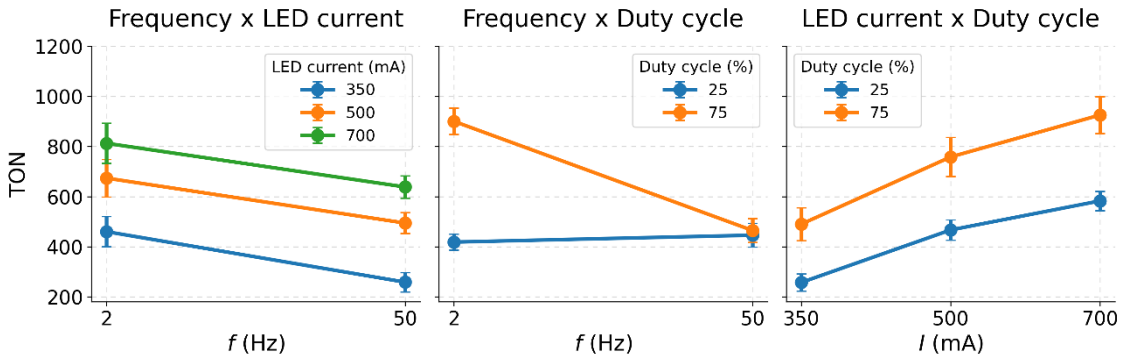

Figure 14: Interaction diagram to explore interdependence of two parameters. Left: Average TONs vs. on/off frequency for different LED currents; center: average TONs vs. on/off frequency for different duty cycles; right: average TONs vs. LED current for different duty cycle. Error bars represent the standard error of the mean.

In general, interaction diagrams indicate the presence of interactions between two parameters when the connecting lines between individual experimental series are non-parallel or even cross (Figure 14, center). In contrast, no interactions are present when the

connecting lines are parallel (e.g. Figure 14, left and right). Here, we observe interactions between the on/off frequency and the duty cycle as shown in Figure 14, center. Since the on/off frequency and duty cycle together describe the duration of the irradiation and dark phases, our findings indicate that certain dark-phase lengths are favorable for reaching higher TONs. This insight will be used later to identify optimized irradiation conditions for this reaction.

Before aiming at optimized reaction conditions, it is important to assess whether most of the changes in reactivity observed are due to the parameters tested, or caused by other, untested (or unknown) parameters. This can be assessed based on the R^2 value, which is a goodness-of-fit parameter to assess whether enough parameters have been used in the data analysis, or whether more complex models using additional parameters would be better suited.[155] Here, the analysis of variance (ANOVA) for this data determined R^2 to be 70.6%, indicating that ca. 71% of the TON changes observed are due to the parameters studied, while ca. 29% of the TON changes observed are due to other, unknown factors (e.g. minor differences in irradiation geometry, H_2 gas leakage, general experimental errors, etc.). This indicates that most TON changes are explained by the parameters studied, which is a sufficient basis for subsequent TON optimization studies.

Finally, the DoE analysis enables prediction of the optimal parameter settings (within the investigated parameter space) for maximizing TON. Based on the factorial model, the predicted optimum is an on/off frequency of 2 Hz, an LED current of 700 mA, and a duty cycle of 75%. To validate this prediction, HER experiments were performed under these conditions. As summarized in Table 2, the resulting TON increased substantially compared to the best conditions shown in Figure 14 as well as compared to the standard setting described above. Notably, the optimum uses a 75% duty cycle and reaches a TON of 1350, whereas a static experiment under otherwise comparable conditions yields only TON = 670. Thus, the optimum setting results in a 102% higher TON while requiring 25% less energy input. Also, TON normalized to energy input increases by a factor of approximately three (Table 2). This unexpected result indicates that introducing dark phases can significantly enhance catalytic turnover while simultaneously reducing energy consumption. Possible explanations include light-induced degradation of reaction

components under continuous irradiation, or a positive role of dark phases in specific catalytic steps; these hypotheses are discussed further below.

Table 2: Average TON for standard and optimized irradiation settings.

Irradiation setting	**700 mA static**	**700 mA, 2 Hz, 75%**
TON	670 ± 140	1350 ± 160
Energy Input	65 mWh	48.75 mWh
TON / energy Input	10.3 mWh^{-1}	27.7 mWh^{-1}

To gain quantitative insights into the energy costs to produce hydrogen in our system, we set out to determine the photonic efficiency (PE) under different irradiation conditions. The photonic efficiency (PE = $n(H_2)/n$(incident photons))[169] was calculated for each parameter setting to identify the most photon-efficient setting. The calculated PEs for all irradiation settings can be found in the SI. The parameter setting with the highest PE was found to be 500 mA, 50 Hz and 25%.

First, for static irradiation (Table 3, entries 1 and 2), we observed identical PEs at different photon fluence rates q_{ph}, indicating that photon fluence rate does not alter the underlying hydrogen evolution mechanisms under continuous, static irradiation. This behavior is also observed in the main effect diagram (Figure 13), where a linear increase of LED current results in a linear increase of TON, indicating that the mechanism of hydrogen evolution under static irradiation remains unchanged over the photon fluence rate range studied. However, under pulsed irradiation conditions (Table 3, entries 3 and 4) we observe that decreasing photon fluence rate results in increasing photonic efficiencies. Most notably, under optimized dynamic conditions (500 mA, 50 Hz, 25%, Table 3, entry 4), the PE increased by a factor of four compared to the static benchmark (Table 3, entry 2). This highlights that dynamic irradiation affects the hydrogen evolution process, most likely by impacting reactions which occur on the same timescale as the dynamic changes (*i.e.*, millisecond timescale). This interpretation suggests that slower processes (*e.g.*, diffusion, aggregation, and ion pairing) are impacted, rather than the faster photophysical/photochemical processes (excitation and charge-separation). Future work will explore potential reaction paths impacted by dynamic irradiation using combined *in situ* experimental studies and theoretical computations.

Table 3: Calculated photonic efficiencies PE, and average photon fluence rate qPh for standard, TON-optimized irradiation settings and the highest PE found

Entry no.	Setting	PE (10^{-3})	qPh (nmol s^{-1} cm^{-2})	TON (-) after 5 h of irradiaiton
1	350 mA static	0.7 ± 0.4	27 ± 4	340 ± 120
2	700 mA static	0.7 ± 0.2	51 ± 4	670 ± 140
3	700 mA, 2 Hz, 75%	1.9 ± 0.3	38 ± 3	1350 ± 160
4	500 mA, 50 Hz, 25%	3.0 ± 1.1	9 ± 1	520 ± 140

The results found for TON and PE as a function of the different irradiation settings are also visualized in a 3D plot in Figure 15. The 3D plot for the TON shows that the surfaces for the different LED currents do not cross each other but seem to be parallel. The LED current shifts the TON only up and down while frequency and duty cycle have different influences. For the PE, the surfaces of the different LED currents intersect. The influence of all 3 key parameters on PE seems to be more complex. The 3D representations clearly show that for achieving the two different optimization objectives, *i.e*. TON or PE, different irradiation conditions must be set.

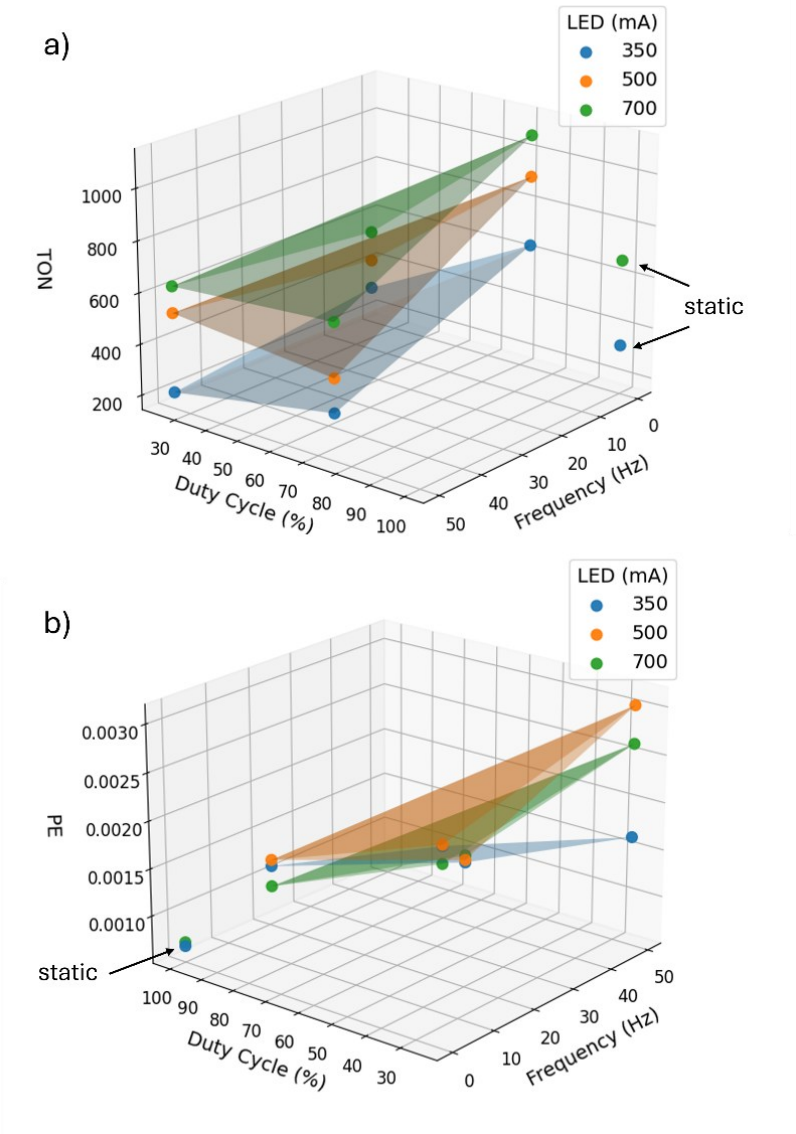

Figure 15: (a) 3D-plot of TON vs. duty cycle and frequency for different LED currents. (b) 3D-plot of PE vs. duty cycle and frequency for different LED currents. Single points represent the static benchmark experiments.

To better understand the trends observed, it is critical to assess the stability of the **PS** and **{Mo$_3$}** under the given reaction conditions. Note that irradiation of the **PS** can lead to degradation (photobleaching), which will impact the observed catalytic reactivity.[97]

Decay rate constants of [Ru(bpy)$_3$]$^{2+}$

As noted above, the photobleaching of the **PS** can be a limiting factor for the catalytic performance of the system. To evaluate whether dynamic irradiation can lead to decreased photobleaching, the decay rate constants of the **PS** were determined under different irradiation conditions using UV-Vis spectroscopy. To this end, the decrease of the

characteristic MLCT transition at 452 nm was monitored over 5 h of irradiation ($\lambda_{irradiation}$ = 465 nm). The degradation of the PS was investigated in two different systems: (1) **PS** in methanol (Ru) and (2) the catalytic system as used in the experiments above (RuSEDCat). The concentration of **PS** was kept identical throughout the experimental series. Decay quantum yields F of the degradation of the **PS** were calculated for the two systems irradiated under different irradiation settings.[170] The data are shown in Table 4.

*Table 4: Decay quantum yields F and time-averaged photon fluence rates q_{Ph} for the two systems Ru (c($[Ru(bpy)_3]^{2+}$) = 20 mM in MeOH) and RuSEDCat (c(**{Mo_3}**) = 0.3 mM, c($[Ru(bpy)_3]^{2+}$) = 20 mM, c(SED) = 10 mM in MeOH : H_2O, 9 : 1, v : v) under different irradiation settings*

Setting	**q_{Ph} (nmol s^{-1} cm^{-2})**	**Φ (10^{-5})**	**$Φ_{RuSEDCat}$ (10^{-5})**
700 mA static	51 ± 44	4.16 ± 0.01	3.2 ± 0.2
500 mA static	37 ± 4	3.330 ± 0.001	4.8 ± 0.5
700 mA, 2 Hz, 75%	38 ± 3	3.7 ± 0.1	4.1 ± 0.1
500 mA, 50 Hz, 25%	9 ± 1	1.2 ± 0.2	8 ± 1

The decay quantum yields for **PS** in pure methanol solutions show a clear trend, in that increasing photonic energy input results in more photobleaching and higher decay quantum yields. We note a particularly low decay quantum yield (*i.e.*, high **PS** stability) for the 500 mA, 50 Hz, 25% setting. Essentially, the data show a linear relationship between photon fluence rate and decay quantum efficiency (Table 16). This is plausible, as higher photonic excitation rates can lead to an increased population of antibonding orbitals on the **PS**, resulting in increased loss of the bpy ligand, which is a known deactivation mechanism for the **PS**.[98–101] Thus, lower photon fluence rate will result in reduced ligand loss, as bpy is a chelating ligand which requires the cleavage of two Ru–N bonds for complete bpy removal.[171] To further study this observation, future studies will focus on detailed time-resolved photophysical studies and complementary theoretical calculations.

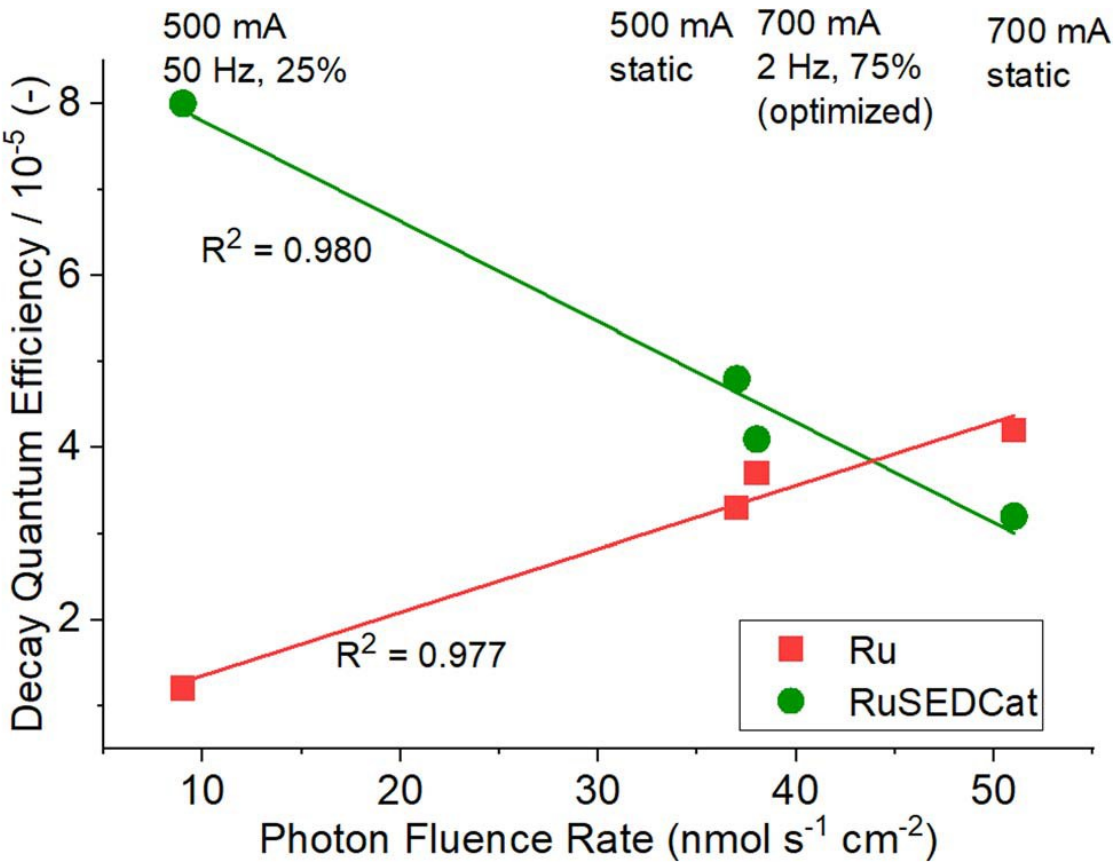

Figure 16: Decay quantum efficiencies Φ_{Ru} and $\Phi_{RuSEDCat}$ depending on photon fluence rate q_{Ph}. The data show linear dependencies and different trends depending on the reaction and irradiation conditions.

In the catalytic system RuSEDCat, we observe a different trend: in general, the decay quantum yields are higher than those for the pure Ru system (except for the high-fluence rate situation, *i.e.*, 700 mA static, Table 4 and Figure 16). This indicates that other components now present in the system (*e.g.* SED, catalyst, *etc.*) increase **PS** degradation. Notably, here, increased photon fluence rate results in decreased decay quantum efficiency (Figure 16), which is the opposite trend to what we observed for the **PS** alone. These initial data suggest that operating the full catalytic system (RuSEDCat) at higher photon fluence rate is beneficial to **PS** stability. One underlying molecular feature which can impact irradiation stability of the PS is the formation of **PS**-SED adducts, which we observed (based on their characteristic UV-Vis absorbance at 532 nm, see SI, Figure 22-29).[118] Importantly, when linking **PS** stability and optimized reaction conditions, we note no major difference in the decay quantum efficiencies for the **PS** between the TON-optimized irradiation conditions (700 mA, 2 Hz, 75%) compared to standard conditions (700 mA, static). This suggests that decreased photobleaching (and thus, higher **PS**

stability) is not the major driver for the higher TONs observed under dynamic irradiation, and in fact, the given dynamic conditions can result in slightly increased PS degradation. For this reason, we subsequently examined the photostability of the catalyst.

Photodegradation of {Mo_3}

{Mo_3} is a red compound and shows visible light-absorption. In a methanol : water mixture (9 : 1, v : v), characteristic absorption bands are observed at λ_{max} = 428 nm, 268 nm and 233 nm (spectra are shown in SI, Figure 30 and 31). The absorption band at 428 nm is likely attributed to a disulfide-to-molybdenum LMCT transition, as supported by DFT calculations (see the SI).

To examine the photostability of **{Mo_3}**, we performed time dependent UV-Vis spectroscopy over 5 hours using the same solvent conditions as used in the catalytic studies (methanol : water mixture (9 : 1, v : v)). Three conditions were examined: static irradiation, dynamic irradiation (both using LED-irradiation at 465 nm), and in the absence of light. Under irradiation, the absorption bands at 428 nm and 268 nm gradually merge into a broad shoulder, and the spectra show fewer distinct peaks (Figure 17). A broad absorption feature between 300 and 350 nm emerges, which increases during irradiation. Based on preliminary TD-DFT-calculations (see the SI), we assign this new band to a previously reported, ligand-exchanged derivative, $[Mo_3S_{13-x}(H_2O)_x]^{(2-x)-}$ (x = 2, 4, 6).[72,148] Based on previous literature, it is likely that under the given conditions, the reaction system contains a mixture of species with varying degrees of ligand substitution (x).[148] Note that DFT calculations of the ligand-exchanged **{Mo_3}** species support these findings and indicate that with increasing degree of ligand substitution, the characteristic spectral features disappear, and lead to a broad absorption in the region of 200–350 nm (for details see the SI). In contrast to the spectral changes observed under irradiation, the non-irradiated solution (Figure 17) shows no significant changes in absorption, confirming that the observed structural transformation of **{Mo_3}** is light-induced.

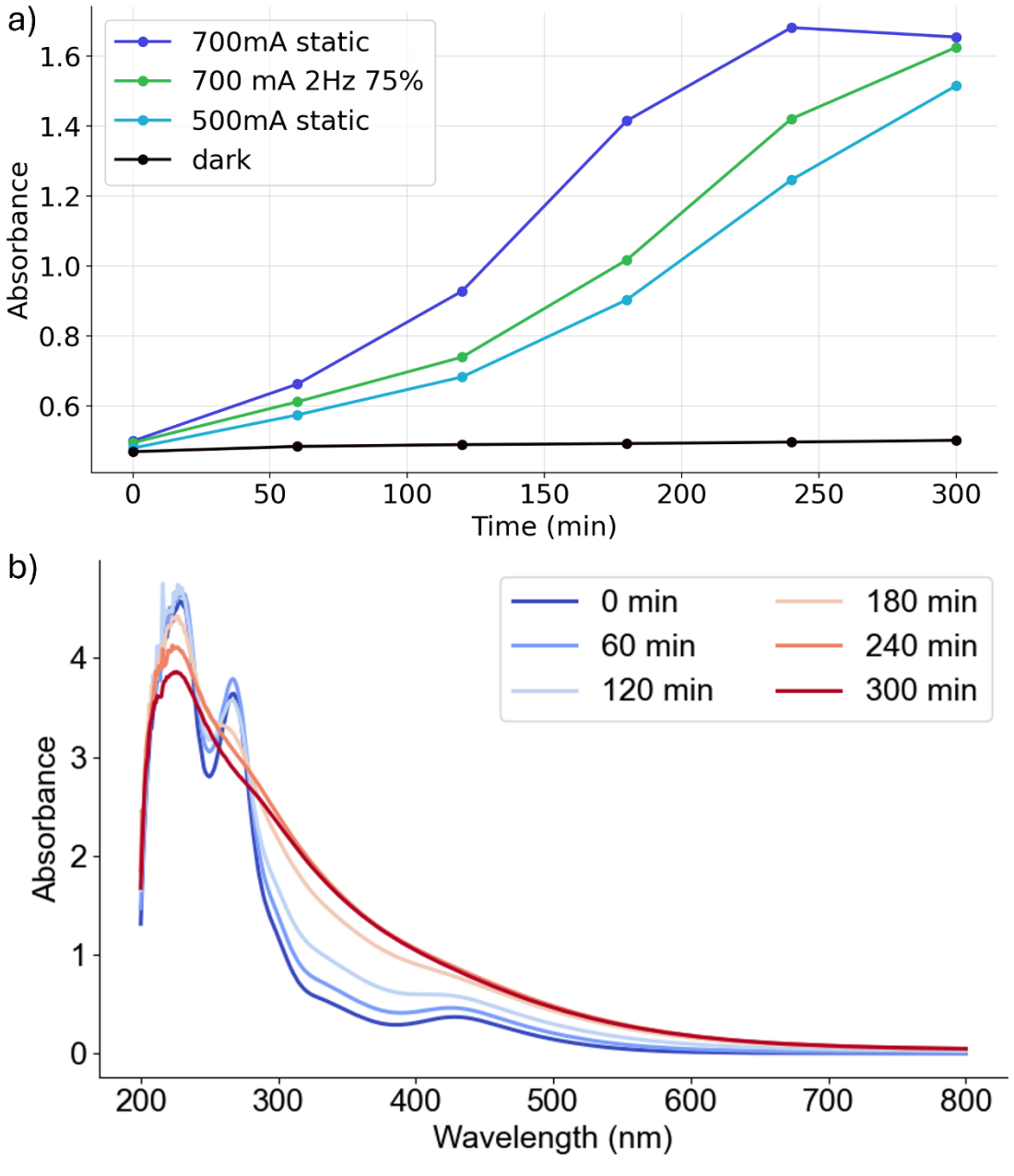

Figure 17: (a) Absorbance at 340 nm over the course of 5 h for the four ***{Mo₃}*** *solutions. One was irradiated statically at 700 mA, one was irradiated dynamically (700 mA, 2 Hz, 75%), and the third one was irradiated statically at lower intensity (500 mA). The fourth solution was not irradiated. (b) Time-dependent UV-Vis spectra of* ***{Mo₃}*** *(c = 0.1 mM) in MeOH: H_2O (9 : 1, v : v) under static irradiation (700 mA, 465 nm).*

Next, we examined the rate of absorption change at comparable photon fluence rate (*i.e.*, 700 mA, 2 Hz, 75%, q_{Ph} = 37 nmol s^{-1} cm^{-2}, and 500 mA static, q_{Ph} = 38 nmol s^{-1} cm^{-2}). Here, we observe that the change in absorption is in a comparable range (within the error margins), suggesting that catalyst deactivation is linked to photon fluence rate, and is not significantly affected by the dynamic irradiation conditions. This is in line with our

hypothesis that irradiation induces structural changes in **{Mo_3}** which eventually result in formation of the inactive $[Mo_3S_7(H_2O)_6]^{4+}$. These changes are mainly driven by photonic excitation and therefore the deactivation rate increases with increasing photon fluence rate. Detailed analysis of the data also shows that the absorbance of this band reaches a maximum after ~4 h under 700 mA static irradiation conditions and subsequently decreases, which may indicate two competitive processes, such as formation of the observed species and subsequent photobleaching at high irradiation intensities.

In sum, these data show that PS and catalyst degradation are controlled by photon fluence rate and increase with increasing photon fluence rate (*i.e.*, energy input); however, they are not directly linked to the dynamic irradiation conditions. Thus, further experimental studies using time-resolved spectroscopy, as well as theoretical calculations and computational modelling of mass transport within the system are required to establish the principal mechanisms of dynamic irradiation.

Conclusions

In sum, we report first insights into the influence of dynamic irradiation on the HER activity of thiomolybdate clusters. Systematic analyses based on Design of Experiments show that the irradiation intensity has the biggest effect on the catalytic activity (based on TON assessment), followed by duty cycle and on/off frequency. Under TON-optimized conditions, we were able to increase the TON by +102% using 25% less energy compared with the static reference conditions. Also, optimization of the photonic efficiency was possible, leading to an approximately threefold increase in TON normalized to the energy input. Initial mechanistic studies shed light on the dependency of photosensitizer and catalyst deactivation on photon fluence rate, and reveal that total photon fluence rate, rather than dynamic conditions controls the system stability. In future, these insights can be used to determine how dynamic irradiation can be used to enable more efficient hydrogen evolution conditions, resulting in more energy- and resource-efficient photocatalysis.

Supporting Information

Instrumentation

Thermogravimetric analysis (TGA) was performed on METTLER TOLEDO TGA 2 STARe system under air flow with a flow rate of 60 mL min^{-1}. A polycrystalline aluminum oxide crucible (PCA) was used. Samples were analyzed in a temperature range of 303.15−823.15 K. A heating rate of 10 K min^{-1} was applied.

Attenuated total reflectance-Fourier-transformed infrared spectroscopy (ATR-FT-IR) was performed using a Bruker Alpha II equipped with an ATR Platinum Diamond unit. The data were recorded with 24 scans at a resolution of 4 cm^{-1}. All spectra were background-corrected within the Bruker OPUS 8.1 program suite.

UV/Vis/NIR spectroscopy was performed on a Cary 3500 UV/Vis/NIR spectrophotometer equipped with a Xenon flash lamp (250 Hz). Measurements were performed in screw cap quartz glass cuvettes (d = 10.0 mm) with rubber septa.

Gas chromatography was performed on a Shimadzu Nexis GC-2030 equipped with a dielectric-barrier discharge ionization detector and a split injection unit with a split ratio of 1:20. Helium was chosen as the carrier gas. The column was heated to a constant temperature of 80 °C.

Chemicals: All chemical reagents were obtained commercially and used as received unless stated otherwise. $(NH_4)_2[Mo_3S_{13}]\cdot 2H_2O$ was prepared according to the literature.[1]

Vials: All vials were purchased from Biotage with crimp caps made of aluminum with silicone rubber/Teflon septa. Outer diameter: 17 mm, inner diameter: 15 mm, length: 85 mm total volume: ~11.0 mL

https://selekt.biotage.com/hubfs/PPS449.v1%20-%20Microwave%20Reaction%20Vials.pdf c)

Experimental data

Synthesis of $(NH_4)_2[Mo_3S_{13}]\cdot 2H_2O$

Synthesis was performed by Moritz Jahn and Laura Haxha.

The thiomolybdate $(NH_4)_2[Mo_3S_{13}]\cdot 2H_2O$ was synthesized using a modified method based on the work of MÜLLER et al.[172] $(NH_4)_6[Mo_7O_{24}]\cdot 4\ H_2O$ (4.0 g, 3.2 mmol) was dissolved in 20 mL of water in a round-bottom flask. An ammonium polysulfide ($(NH_4)_2S_x$) solution (120 mL, 25 wt.-%) was added, and the flask was covered with a watch glass. The solution was heated to 96 °C for five days without stirring. Dark-red crystals of $(NH_4)_2[Mo_3S_{13}]\cdot 2H_2O$ formed, which were collected by filtration, then washed with water, ethanol, carbon disulfide and ether. The final product was air-dried.

Yield: 5.5 g (7.04 mmol; 91.4 % based on Mo)

UV-VIS bands (nm): λ_{max} = 451

ATR-FTIR bands (cm^{-1}): 1478 (s), 537 (s) ,511 (s)

TGA: **(1)** Temp: 30 °C – 295 °C, calculated mass loss: 6.2 %, possible loss: 2 H_2O

(2) Temp: 295 °C – 550 °C, calculated mass loss: 31.5 %, possible loss: 2 NH_3, 6 S

Experimental Plan

The following experiment plan was created by Minitab for a full factorial screening approach with three factors. Since only the same frequency and duty cycle but all LED currents could be measured on the same day, blocks were created manually. Every factor setting combination was measured on three individual days (triplicate) and on each day three samples were prepared.

Table 5: Experiment plan created by Minitab and adapted to use.

Measurement day	Frequency (Hz)	LED current (mA)	Duty cycle (%)
1	2	350, 500, 700	25
2	50	350, 500, 700	75
3	2	350, 500, 700	75
4	50	350, 500, 700	25
5	2	350, 500, 700	75
6	50	350, 500, 700	75

7	2	350, 500, 700	75
8	2	350, 500, 700	25
9	50	350, 500, 700	25
10	50	350, 500, 700	25
11	2	350, 500, 700	25
12	50	350, 500, 700	75

Sample preparation

GC measurements: Stock solutions for the catalyst $(NH_4)_2[Mo_3S_{13}]$ (c = 3 · 10^{-4} M), the photosensitizer (c = 1 · 10^{-5} M) and the sacrificial electron donor (sodium ascorbate and ascorbic acid, molar ratio: 4:5 ; c = 1 · 10^{-1} M in water) were prepared for the catalytic systems. The catalyst solution was prepared by dissolving $(NH_4)_2[Mo_3S_{13}]$ in degassed methanol and was afterwards stored under N_2 atmosphere. The photo sensitizer $[Ru(bpy)_3](PF_6)_2$ was dissolved in methanol. For the SED solution, sodium ascorbate and ascorbic acid were dissolved in water. The stock solutions were stored while keeping them protected from light.

Before mixing the individual components, the catalyst solution was diluted with methanol by a factor of 100, resulting in a concentration of c = 1 · 10^{-6} M. The stock solutions for the PS and the SED, the solvent as well as the diluted catalyst solution were combined in crimp vials with a total volume of 4 mL per vial. The vials were sealed with crimper lids equipped with silicone septa and purged with nitrogen for one hour. Additionally, the septa were covered with clear nail polish after being pierced by the syringes to prevent leakage. Before measurements, the nail polish was removed to allow sampling of the gas headspace.

UV/Vis measurements: For determination of the quantum yield of the photosensitizer, stock solutions were prepared analogously to the GC measurements sample preparation. The cuvettes were sealed with silicon septa equipped screw caps and then purged for 10 min with nitrogen before measurements were performed.

For determination of the photodegradation of the **{Mo_3}** cluster, the solid was weighed into screw cap vials and then dissolved in a degassed MeOH:H_2O (9:1, v:v) mixture. The solution was then put in an ultrasonic bath for 15 min and transferred in the cuvettes. The cuvettes were sealed with silicone septa equipped screw caps and purged with nitrogen for 10 min.

Procedure of GC measurements

After successful preparation, the samples were placed in the photoreactor. The photoreactor was equipped with a hexagonal holding unit with six individual spots for the crimp vials. For every hydrogen measurement, at least three individual samples were prepared. Before the hydrogen measurement started, the GC was checked with three air measurements to obtain a reproducible baseline. The samples were measured at the beginning of the irradiation, and at the respective time intervals of irradiation.

Photoreactor setup

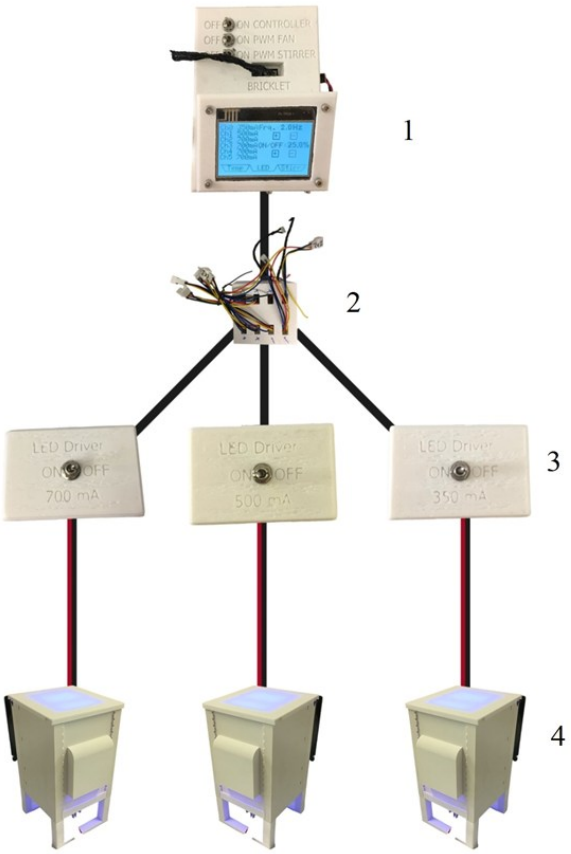

Figure 18: Photograph of the photoreactor setup, with a controller module (1), an In/Out-Bricklet (2), three LED drivers (3) and three photoreactors (4).

The controller module enables the control of the duty cycle and the frequency. The In/Out bricklet forwards the signal to the individual LED-Drivers which determine the LED current and therefore indirectly the light power. The LED is positioned at the bottom of the photoreactor. The whole design was created by Kowalzcyk et al.[144]

The 90x90x140 mm modular photoreactor was chosen for these experiments and printed with white PLA. The vial holder was placed in the 10th vertical holder slot above the LED and the lower distance between the bottom of the reactor and the vials bottom was 22 mm. The radius of the holder was 43 mm.

An instruction manual and CAD files to print the reactor and controller units as well as the python script that was used in the controller unit to set frequency and duty cycle can be found here:

https://github.com/photonZfeed/modularPhotoreactor

Information about the used LED:

https://look.ams-osram.com/m/6208f3ef096a8da0/original/LZ1-10B202.pdf

https://look.ams-osram.com/m/77b624bf9a989535/original/LZ1-00B202.pdf

LED Driver:

https://www.meanwellusa.com/webapp/product/search.aspx?prod=LDD-L OSRAM

LED Engin LZ1-00B202:

https://www.mouser.de/datasheet/3/5912/1/LZ1_00B202_EN.pdf

The sample positions of the vials were chosen randomly to eliminate the systematic error of heterogeneous irradiation conditions in a photoreactor.

LED Power Determination

To measure the power of the LED a PM400 Optical Power Meter by Thorlabs was used. Power was measured at five or six positions of the photoreactor for different currents in duplicate or triplicate. The chosen positions were in radial order and at a height comparable to bottom of the sample flasks.

Table 6: Measured LED power P for different positions 1-6 in the photoreactor with individual measurement error. Red fields represent outliers which were rejected when calculating averages and standard deviations.

I_{LED}	P1 (mW)	P2 (mW)	P3 (mW)	P4 (mW)	P5 (mW)	P6 (mW)
350 mA (1)	7.6 ± 0.3	7.0± 0.3	6.5 ± 0.3	5.3 ± 0.3	7.0 ± 0.2	7.4 ± 0.3
350 mA (2)	7.4 ± 0.2	7.4 ± 0.3	6.8 ± 0.3	6.0 ± 0.3	7.2 ± 0.3	7.3 ± 0.3
350 mA (3)	7.5 ± 0.3	6.9 ± 0.2	6.2 ± 0.3	5.6 ± 0.3	7.4 ± 0.3	7.7 ± 0.3
500 mA (1)	9.6 ± 0.2	10.7 ± 0.3	10.6 ± 0.4	7.6 ± 0.3	6.4 ± 0.3	--
500 mA (2)	9.3 ± 0.3	10.8 ± 0.3	10.8 ± 0.3	8.4 ± 0.3	7.0 ± 0.3	--
700 mA (1)	14.4 ± 0.4	13.5 ± 0.3	14.1 ± 0.3	11.6 ± 0.4	13.1 ± 0.3	--
700 mA (2)	13.2 ± 0.3	13.7 ± 0.2	12.2 ± 0.3	12.0 ± 0.3	12.4 ± 0.3	--

Table 7: Average LED power for different current supplies and the corresponding photon fluence rates q (calculated using equation 13). All values are only given for the area of 1 cm^2 of the detector.

I_{LED} (mA)	P_{LED} (mW)	ΔP_{LED} (mW)	q (nmol s^{-1} cm^{-2})	Δq (nmol s^{-1} cm^{-2})
350	6.9	± 1.0	27	± 4
500	9.4	± 1.0	37	± 4
700	13.0	± 1.0	51	± 4

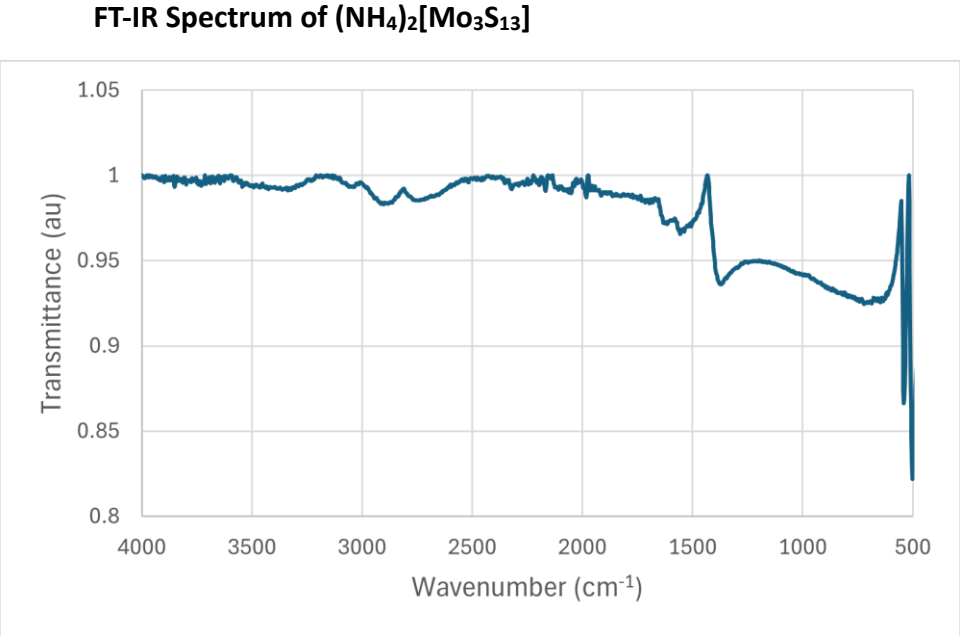

Figure 19: FT-IR spectrum of $(NH_4)_2[Mo_3S_{13}]\cdot 2H_2O$.

TGA Analysis

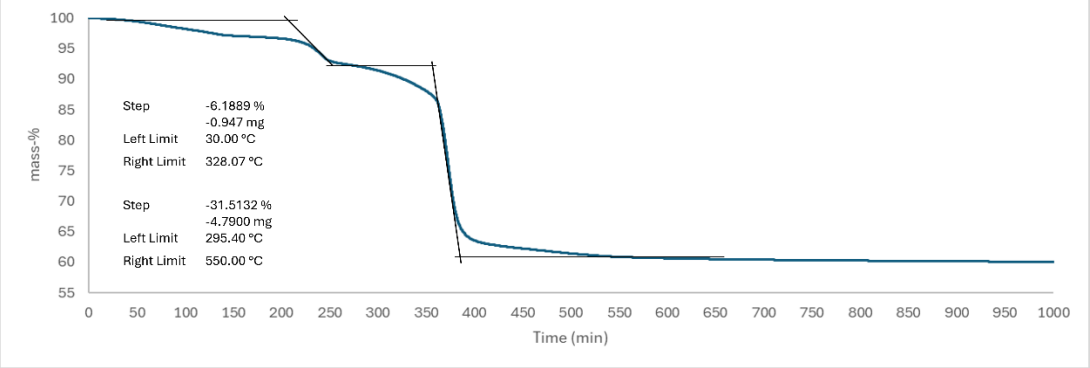

Figure 20: TGA of $(NH_4)_2[Mo_3S_{13}]\cdot 2H_2O$.

Calculation of TON

To determine the TON, the volume of the gas phase in the vial was calculated using the following equation:

$$V_{gas} = V_{vial} - V_{sol} \quad [9]$$

V_{gas}: gas volume of the vial. V_{vial}: total volume of the vial. V_{sol}: volume of the catalytic solution. The sample volume taken is 100 µL. To calculate the absolute amount of hydrogen evolved a vial specific factor k_{vial} must be calculated using equation 10:

$$k_{vial} = \frac{V_{gas}}{100\ \mu L} \quad [10]$$

The absolute amount of hydrogen evolved $n_{H2,abs}$ can then be determined with the with the measured amount of hydrogen $n_{measured}$ per 100 µL, using the following equation:

$$n_{H_2,abs} = n_{measured} \cdot k_{vial} \quad [11]$$

The TON is the ratio of the absolute amount of hydrogen $n_{H2,abs}$ and the amount of catalyst in the solution n_{cat}:

$$TON = \frac{n_{H_2,abs}}{n_{cat}} \quad [12]$$

Table 8: Measured TON for experimental plan and DoE. Red fields represent outlier measurements with high errors that were not used when calculating averages and standard deviations.

50 Hz, 25%			50 Hz, 75%			2 Hz, 25%			2 Hz, 75%		
TON 350 mA	**TON 500 mA**	**TON 700 mA**	**TON 350 mA**	**TON 500 mA**	**TON 700 mA**	**TON 350 mA**	**TON 500 mA**	**TON 700 mA**	**TON 350 mA**	**TON 500 mA**	**TON 700 mA**
92	693	773	495	999	1360	491	267	480	950	980	1310
430	642	810	717	1110	1220	270	658	738	651	1110	1040
12	599	579	849	1170	1560	528	708	477	867	906	1420
361	394	429	62	623	603	207	482	666	314	755	1330
68	305	344	430	473	724	286	282	570	545	1220	999
99	321	415	363	568	600	338	521	14	430	1110	1130
140	61	812	359	144	*	195	309	418	380	607	850
361	600	779	329	232	547	263	223	517	300	766	838
300	586	653	236	390	867	194	346	446	765	873	1190

Table 9: TON for 350 mA static irradiation.

Number	TON	Number	TON
1	447	12	437
2	245	13	498
3	219	14	678
4	219	15	501
5	396	16	826
6	123	17	415
7	70	18	233
8	104	19	277
9	116	20	210
10	115	21	101
11	509	22	359

Table 10: TON for optimized irradiation settings:700 mA, 2 Hz, 75%.

Number	TON
1	1520
2	1430
3	1600
4	1190
5	1370
6	1290
7	1600
8	1350
9	1230
10	1210
11	1110

Table 11: TON at 700 mA static irradiation.

Vial number	TON
1	430
2	988
3	831
4	601
5	500
6	665

Time-dependent TON

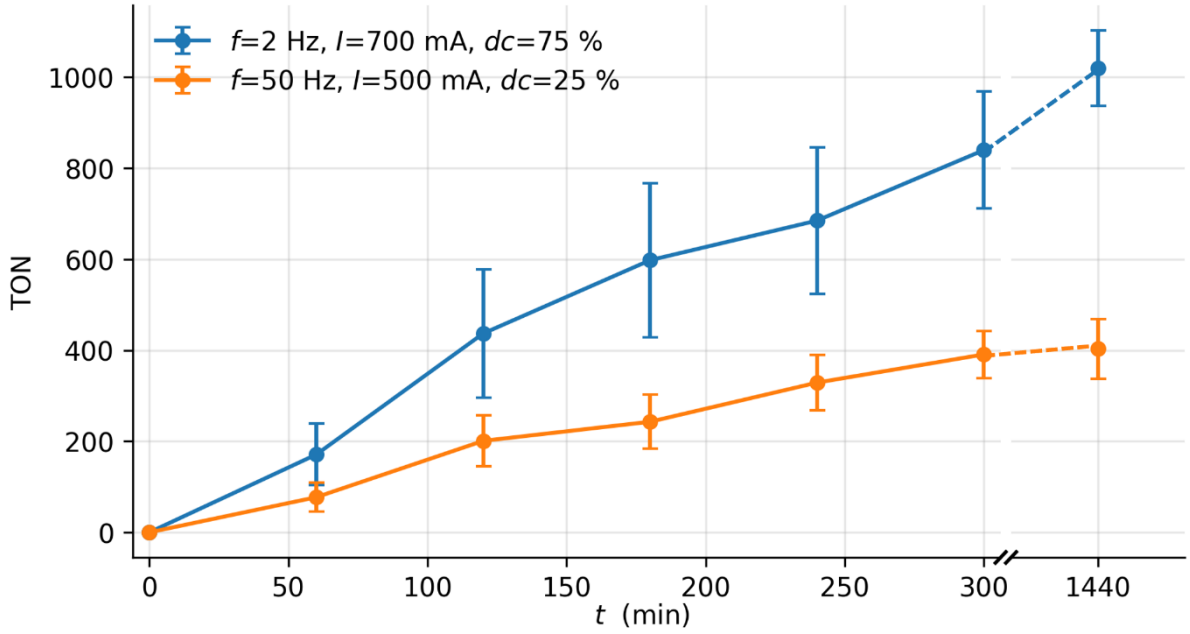

Figure 21: Time dependent TON for optimized irradiation conditions.

Since the system is close to an end after 5 hours, the overall performance is represented at the measurements taken once after 5 h of irradiation.

Calculation of photonic efficiency (PE)

The photonic efficiency PE is determined using the photon fluence rate q which is calculated based on the experimentally determined power P of the LED, the emission wavelength λ, the Planck constant h, the speed of light c and the Avogadro constant N_A.[173]

$$q = \frac{P \cdot \lambda}{h \cdot c \cdot N_A} \qquad [13]$$

The total number of photons n_{ph} can be calculated by multiplying the photon fluence rate q with the time t, the duty cycle (0.25 or 0.75) and the area A_{Vial} of the vial (= 1.227 cm^2).

$$n_{ph} = q \cdot t \cdot \mathrm{dc} \cdot A_{Vial} \qquad [14]$$

The PE is calculated using equation [15].

$$PE = \frac{n_{H_2,abs}}{n_{ph}} \quad [15]$$

Table 12: PE calculated based on averaged TONs. The last two rows represent static irradiation.

LED current (mA)	Frequency (Hz)	Duty cycle (%)	PE ($\cdot 10^{-3}$)
350	50	25	1.7 ± 1.4
500			3.0 ± 1.1
700			2.6 ± 0.8
350	50	75	0.9 ± 0.5
500			0.9 ± 0.4
700			0.9 ± 0.3
350	2	25	2.5 ± 1.4
500			2.5 ± 1.1
700			2.3 ± 0.8
350	2	75	1.7 ± 0.6
500			1.8 ± 0.4
700			1.9 ± 0.3
350	0 (static conditions)	100 (static conditions)	0.7 ± 0.4
700	0 (static conditions)	100 (static conditions)	0.7 ± 0.2

UV/Vis Spectroscopy

All cuvettes were placed in holders so that the bottom of the cuvettes was 22 mm above the LED.

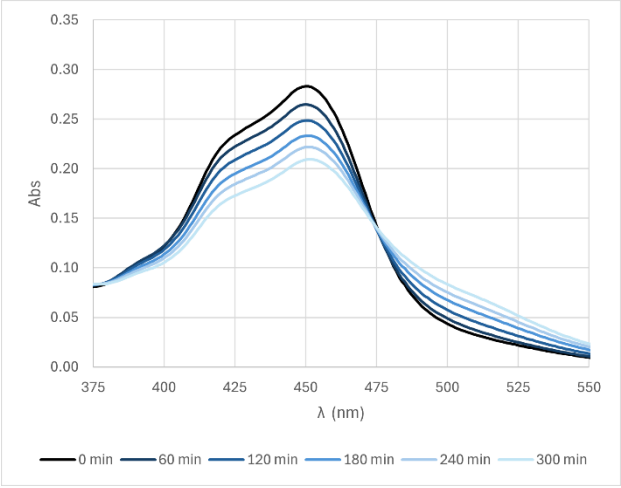

Figure 22: UV/Vis spectra over time for Ru (c = 20 µM in MeOH) irradiated under 700 mA static conditions.

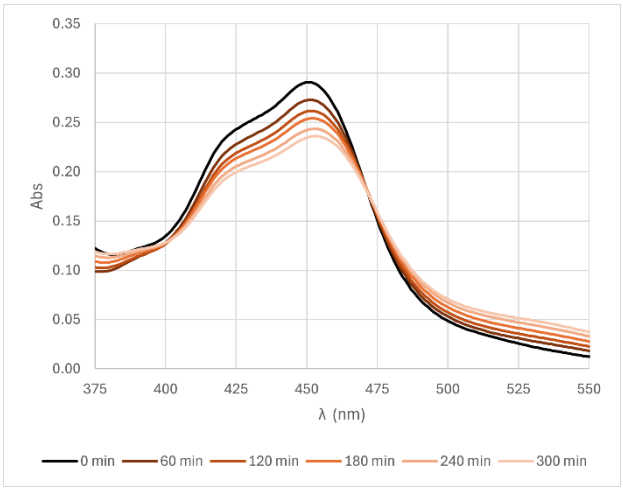

Figure 23: UV/Vis spectra over time for RuSEDCat (c_{Ru}= 20 µM, c_{Mo3}= 0.3 µM, c_{SED}= 100 µM in MeOH:H_2O; 9:1; v:v) irradiated under 700 mA static conditions.

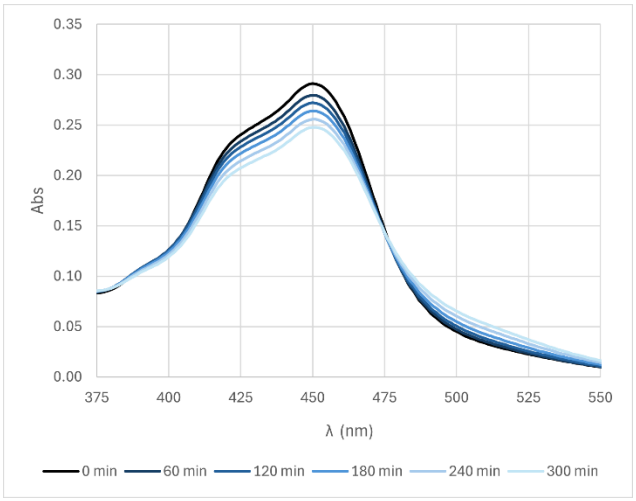

Figure 24: UV/Vis spectra over time for Ru (c = 20 µM in MeOH) irradiated under 500 mA static conditions.

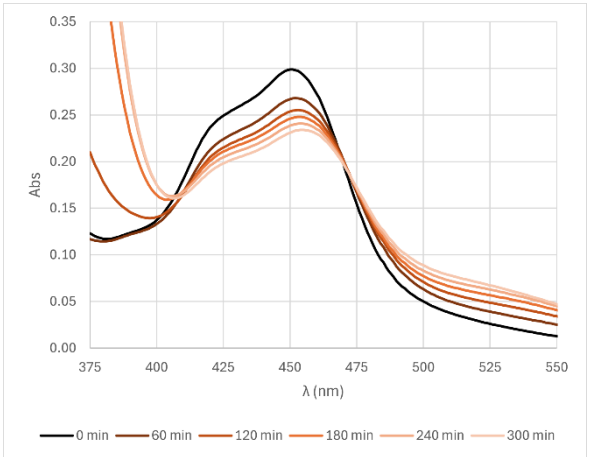

Figure 25: UV/Vis spectra over time for RuSEDCat (c_{Ru}= 20 µM, c_{Mo3}= 0.3 µM, c_{SED}= 100 µM in MeOH:H2O; 9:1; v:v) irradiated under 500 mA static conditions.

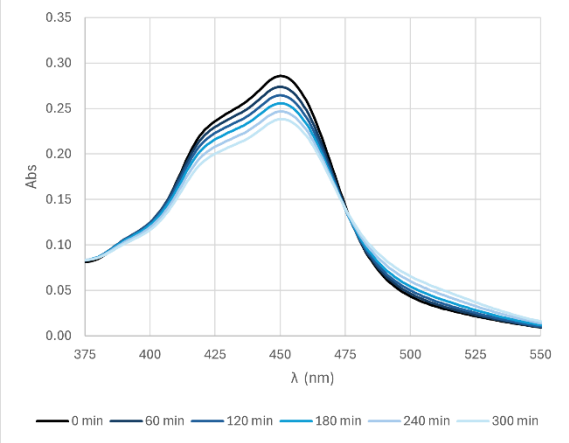

Figure 26: UV/Vis spectra over time for Ru (c = 20 µM in MeOH) irradiated under 700 mA, 2 Hz, 75% conditions.

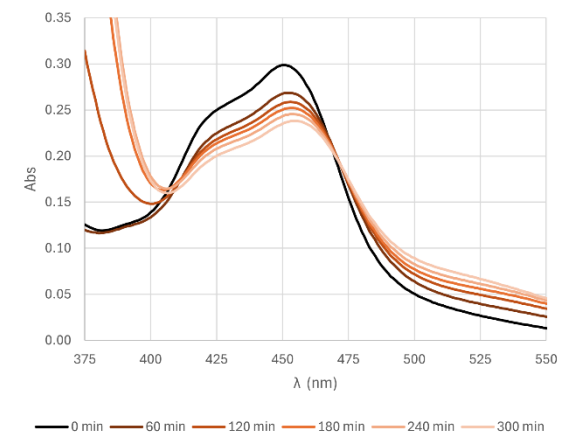

Figure 27: UV/Vis spectra over time for RuSEDCat (c_{Ru}= 20 µM, c_{Mo3}= 0.3 µM, c_{SED}= 100 µM in MeOH:H_2O; 9:1; v:v) irradiated under 700 mA, 2 Hz, 75% conditions.

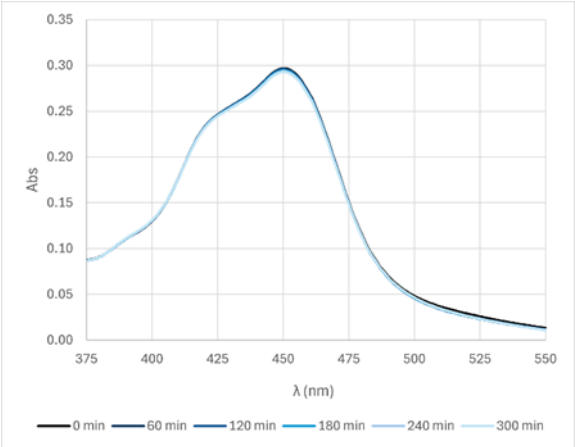

Figure 28: UV/Vis spectra over time for Ru (c = 20 µM in MeOH) irradiated under 500 mA, 50 Hz, 25% conditions.

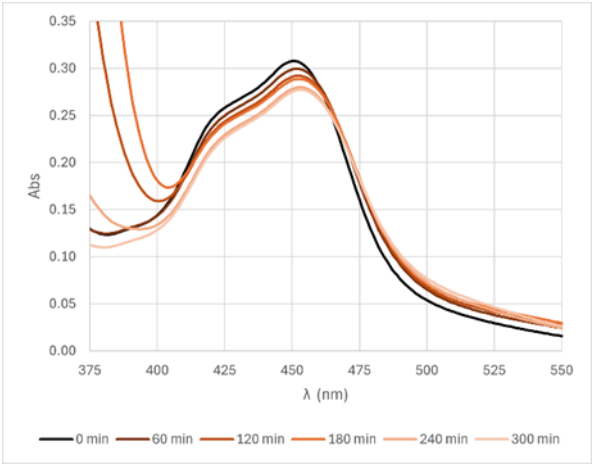

Figure 29: UV/Vis spectra over time for RuSEDCat (c_{Ru}= 20 µM, c_{Mo3}= 0.3 µM, c_{SED}= 100 µM in MeOH:H_2O; 9:1; v:v) irradiated under 500 mA, 50 Hz, 25% conditions.

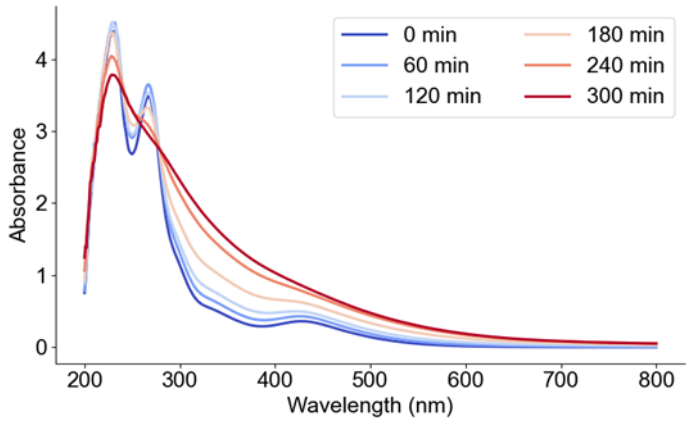

*Figure 30: UV/Vis spectra over time for **{Mo₃}** (c = 0.1 mM) in MeOH:H_2O (9:1, v:v) irradiated under 700 mA, 2 Hz, 75% conditions.*

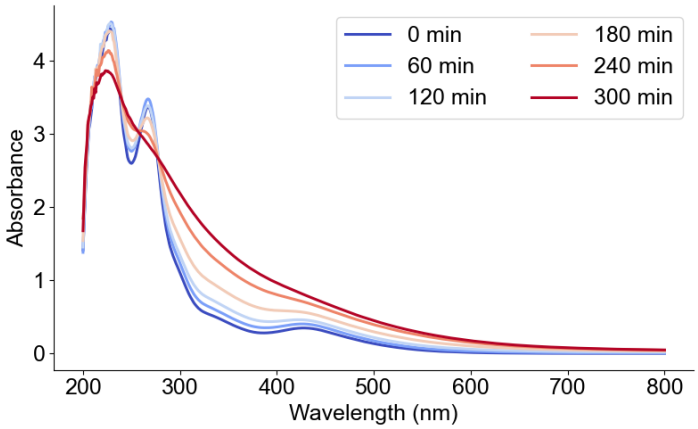

*Figure 31: UV/Vis spectra over time for **{Mo₃}** (c = 0.1 mM) in MeOH:H_2O (9:1, v:v) irradiated under 700 mA, 2 Hz, 75% conditions.*

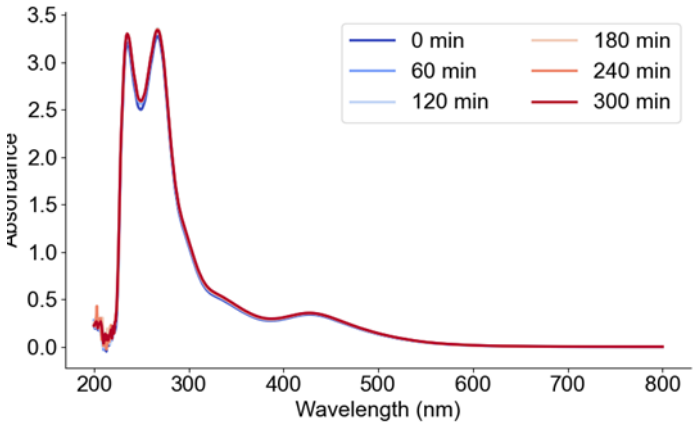

*Figure 32: UV/Vis spectra over time for **{Mo₃}** (c = 0.1 mM) in MeOH:H_2O (9:1, v:v) without irradiation.*

Calculation of quantum yields

Based on the time dependent absorbance *A* of the 452 nm band the decay rate of the concentration of $[Ru(bpy)_3]^{2+}$ was determined. Concentration was calculated using Beer-Lambert law:[174]

$$c(t) = \frac{A(t)}{\varepsilon \cdot d} \tag{16}$$

Here ε is the absorption coefficient of 14 600 L mol^{-1} cm^{-1},[98] *d* is the thickness of the cuvette (1 cm).

The values for the concentration can be found in the supporting data. The slope of the concentration against time was calculated and represents the changing rate *r* of the $[Ru(bpy)_3]^{2+}$ concentration. Here we assume a pseudo-first order for the degradation of the **PS**.

$$r = \frac{\Delta c}{\Delta t} \tag{17}$$

With the incident photon fluence rate *q* (equation 13), the transmission of the sample *T* (0.26 for a path length of 20 mm in the cuvette (filling height) and therefore an absorbance of 0.58), the volume *V* of the sample (2 mL) and the changing rate of the concentration *r* the quantum yield is calculated using the following equation:

$$\Phi = \frac{r * V}{q * T} \tag{18}$$

Computational Data

The ORCA 6.1.[175] computational software was used to carry out optimization and TD-DFT UV-Vis calculations. This work used the Becke 3-Parameter Lee-Yang-Parr (B3LYP)[176] at the hybrid level of theory. This functional was chosen based on previous studies.[148] The **def2-type** basis set of triple-zeta quality within the valence region, with an additional polarization function (**def2-TZVP**)[177], was employed together with **Grimme's D3BJ dispersion correction**, as implemented in the ORCA 6.1. software package to account for any longer-range interactions.[178,179] The **effective core potentials (ECPs)** for molybdenum were likewise taken from the ORCA 6.1 implementation.[180] For the TD-DFT calculations specifically, 100 transitions are calculated per geometry.

Simulated UV/Vis spectra

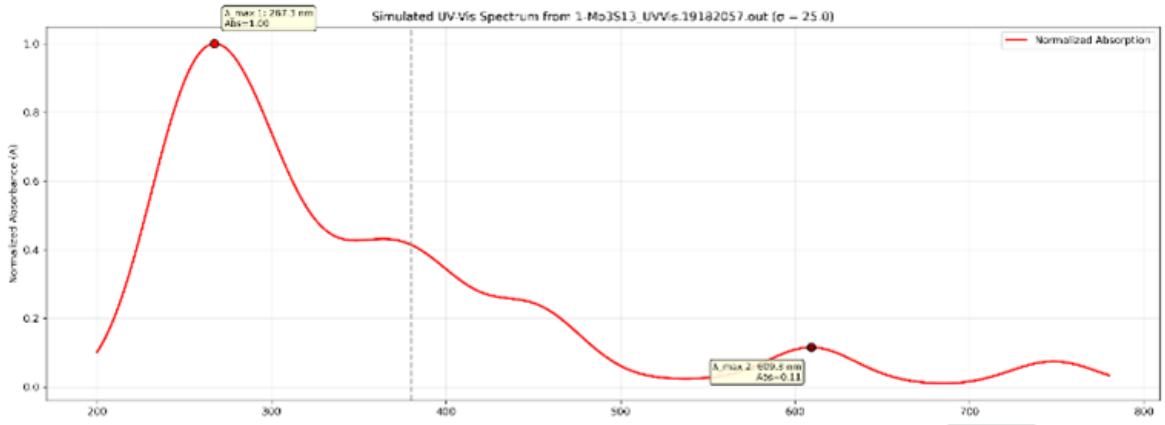

*Figure 33: DFT-simulated UV/Vis spectrum of the **{Mo_3}** cluster.*

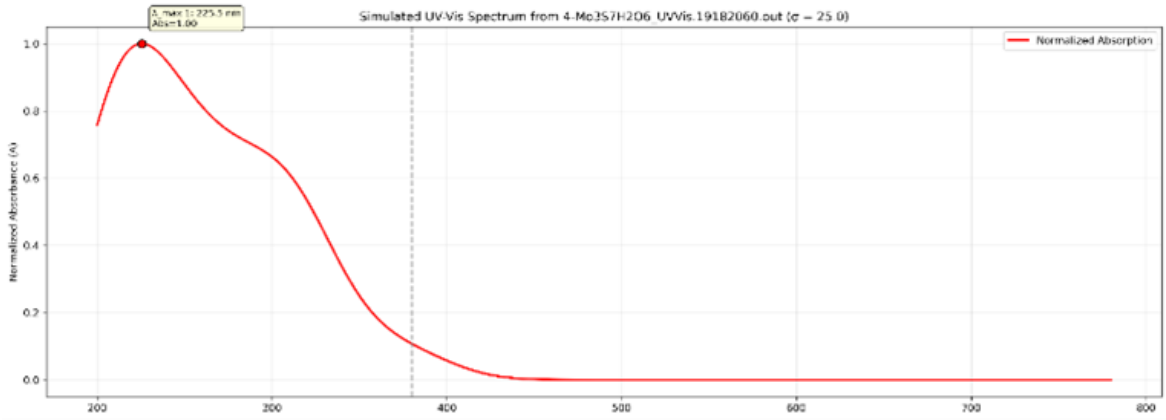

Figure 34: DFT-simulated UV/Vis spectrum of $[Mo_3S_7(H_2O)_6]^{4+}$.

Over the course of ligand exchange the change and reduction of transitions involving ligand centers is assumed. Those transition states may correlate to LMCT states or similar

mixed states. The respective transition bands may be around 750 nm, 610 nm, 450 nm, 380 nm. In the final species, $[Mo_3S_7(H_2O)_6]^{4+}$, a new mixed transition state around 300 nm was calculated, which involves the bridging disulfide ligands, which had not been involved for most of the significant LMCT states mentioned above.

3.2 {Mo_2} can do it too – Dynamic irradiation increases efficiency of light-driven hydrogen evolution by $[Mo_2S_{12}]^{2-}$

The results presented in this chapter are based on a manuscript that is intended for publication and has already been submitted to *Sustainable Energy & Fuels* and as a preprint to ChemRxiv (DOI https://doi.org/10.26434/chemrxiv-2025-m020t). The manuscript is available for reproduction under a Creative Commons Attribution 4.0 International License (CC BY 4.0). As the manuscript had not yet been accepted for publication at the time this thesis was submitted, its contents are reproduced here. Minor adaptations were made for inclusion in this thesis, and the contributions of the co-authors are acknowledged after the abstract. The supporting information to the manuscript can be found directly after the manuscript's conclusion.

Abstract

Molecular thiomolybdate clusters are promising earth-abundant catalysts for light-driven hydrogen evolution, yet their performance can strongly depend on irradiation conditions. Here we assess dynamically modulated irradiation for homogeneous photocatalytic hydrogen evolution reaction (HER) using $[Mo_2S_{12}]^{2-}$ (**{Mo_2}**) with $[Ru(bpy)_3]^{2+}$ and ascorbic acid/ascorbate in methanol irradiated using a 465 nm LED. A Design-of-Experiments (DoE) approach quantifies the effects of LED current, on/off frequency, and duty cycle. Duty cycle and current dominate turnover, with significant interactions involving duty cycle. DoE predicts an optimum at 700 mA, 2 Hz, and 75% duty cycle, giving a slightly higher normalized turnover number (TON;1.04 ± 0.09) while reducing energy input by 25% versus static irradiation. Normalized photonic efficiency is maximized at lower average photon input (500 mA, 2 Hz, 25% duty cycle). Time-resolved UV–Vis spectroscopy – interpreted via TD-DFT calculations - indicate slow ligand exchange (245 nm decay with ~212 nm growth) under light exclusion and a distinct photoinduced evolution under irradiation, including formation of a band near ~227 nm. Although 245 nm decay kinetics are similar under static and dynamic irradiation, dynamic protocols improve energy and photon utilization, highlighting irradiation engineering as a practical lever to optimize molecular photocatalytic HER.

Author contributions

S. H. Kolbinger	Conceptualization, methodology, investigation, formal analysis, data processing, writing original draft, visualization, discussion and revision
K. Krauchanka	Methodology, formal analysis
D. Kowalczyk	Methodology, resources, discussion and revision
L. Schleicher	Methodology, formal analysis, computational simulations, synthesis
L. Senz	Methodology, validation, resources
S. Kupfer	Discussion and revision
D. Ziegenbalg*	Conceptualization, supervision, funding acquisition, writing original draft, discussion and revision
C. Streb*	Conceptualization, supervision, funding acquisition, writing original draft, discussion and revision

* Corresponding author

Introduction and Motivation

Molybdenum sulfides have attracted considerable attention as earth-abundant, noble-metal-free catalysts for the HER.[156–159] In particular, molecular molybdenum sulfide clusters (thiomolybdates) have emerged as key molecular prototypes for studying reactivity and elucidating the mechanisms that govern HER activity and catalyst stability.[72, 116, 148,160]

Recently, the thiomolybdate cluster (**{Mo_2}**, Figure 7 right) has shown promising potential as a homogeneous catalyst for the light-driven HER, reaching TONs exceeding 1000 under optimized conditions.[72,148]

However, mechanistic studies suggest, that thiomolybdates are highly sensitive to the reaction conditions and change behaviour under catalytic operation, so that predictive reactivity tuning is challenging.[72,148] This dynamic behaviour has previously been observed for the thiomolybdate HER-catalyst (**{Mo_3}**).[72, 148,181] It is caused by disulfide ligand exchange, thereby generating mixtures of structurally related species in solution, so that structure–reactivity-function relationships are obscured.[72,161] Furthermore, **{Mo_3}** absorbs visible light and recent studies showed that irradiating the cluster in

solution (λ = 465 nm) leads to photodegradation.[182] Dynamic effects were also observed for the **{Mo$_2$}** cluster in earlier studies.[127] However, these effects were not investigated in detail, leaving a knowledge gap for further development. This gap is addressed and further investigated in this work.

Recent studies on **{Mo$_3$}** have also demonstrated a major impact of the external irradiation conditions on the observed HER activity.[182] In particular, the use of dynamic irradiation protocols in **{Mo$_3$}** homogeneous HER was used to limit catalyst degradation and consequently, increase catalytic performance. For **{Mo$_3$}**, suitable combinations of irradiation intensity, frequency, and duty cycle led to a twofold increase in hydrogen evolution while reducing the overall energy input by 25% compared to static irradiation.[182] Mechanistic studies highlighted that a reduced photoinduced degradation of **{Mo$_3$}** is the underlying reason for the reactivity improvements observed.[182] These findings illustrate that even well-studied light-driven catalytic systems still offer significant potential for performance gains by detailed mechanistic study and rational control of external parameters such as irradiation conditions, making this insight highly relevant for technological implementation. To-date, there is no information on whether similar considerations are held for other molecular molybdenum sulfide clusters, such as **{Mo$_2$}**. This work aims to close this mechanistic knowledge gap using a synergetic experimental-theoretical approach.

Here, we report how dynamically modulated irradiation affects the light-driven HER activity of **{Mo$_2$}** when used in homogeneous solution together with the PS $[Ru(bpy)_3]^{2+}$ and ascorbic acid/ascorbate as SED. We apply a statistical DoE approach to quantify the impact of irradiation intensity (determined by the LED current, on/off frequency (number of complete on off cycles per second), and duty cycle (percentage of time when the LED is turned on) on catalytic performance. Based on analysis of key correlations between these parameters we identify optimized reaction conditions for enhanced HER.[153] In addition, combined experimental and theoretical mechanistic studies provide initial insights into the molecular processes that govern the reactivity and stability of this system.

Results and discussion

Homogeneous light-driven HER in a protonic solvent requires three main components: a photosensitizer, a catalyst, and a sacrificial electron donor. In this study, $[Ru(bpy)_3](PF_6)_2$

was used as the PS (c = 20 µM), $(NH_4)_2$**{Mo_2}** as the catalyst (c = 0.5 µM), and a buffer solution of ascorbic acid and sodium ascorbate (pH 4, c = 10 mM, molar ratio 5:4) as the SED. Previous studies showed that this system performs best in methanol, and pure methanol was therefore chosen as solvent.[127] All experiments were performed using LED irradiation at λ_{max} = 465 nm. The catalytic system remains highly sensitive to the reaction conditions, such that minor differences in sample preparation can lead to major variations in hydrogen evolution. To minimize day-to-day variations in catalytic performance, a benchmark experiment was carried out on each experimental day, and all TONs were normalized to the corresponding benchmark value.

Photocatalysis was performed in custom-built 3D printed modular photoreactors with reproducible irradiation conditions,[144], thereby reducing experimental errors. As benchmark, a static irradiation at an LED current of 700 mA was chosen, corresponding to a photon irradiance of 51 nmol s^{-1} cm^{-2}. For simplicity, only LED currents are given in the following (for details see SI). After 5 h of irradiation, the amount of hydrogen evolved was quantified by gas chromatography. On each experimental day, four photoreactors were operated in parallel, each with three identically prepared samples (triplicates). One reactor was run under the static benchmark conditions, while the remaining three reactors were used to evaluate different irradiation settings based on a randomized DoE experimental plan.

Dynamic irradiation in this study is defined by three experimental parameters. The first is the LED current, which determines the photon irradiance (350 mA, 500 mA, or 700 mA, photon irradiance can be found in Table S4). The second parameter is the pulse frequency, i.e., the number of complete on/off cycles per second (2 Hz or 50 Hz). The third parameter is the duty cycle, defined as the fraction of time the LED is switched on during each cycle (25% or 75%).

Traditionally, the influence of multiple experimental factors is often investigated using a one-factor-at-a-time (OFAT) approach.[154,167] However, OFAT suffers from several drawbacks: it requires a large number of experiments and does not provide information on possible interdependencies between single parameters. Statistical DoE overcomes these limitations by using structured experimental plans and analysis of variance (ANOVA) to quantify both individual parameter effects and their interdependencies.[153,167]

In this project, a DoE methodology was employed, and experiments were carried out according to a randomized experimental plan. Photocatalytic HER experiments were performed in nine replicates in total for each parameter combination to ensure sufficient statistical robustness. The resulting data set was analyzed using *Minitab 22*.[155,183] As a first step, the influence of LED current, pulse frequency, and duty cycle (dc) on HER performance was evaluated using a main effect diagram (Figure 35).

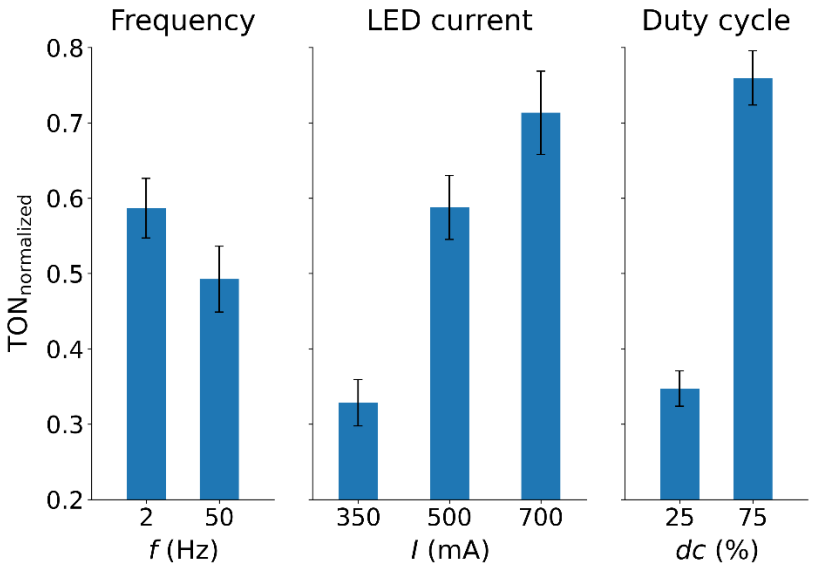

Figure 35: Main effect diagram for the individual parameters on/off frequency, LED current and duty cycle. Plot of the average normalized TON vs. frequency, LED current and duty cycle. Error bars represent standard error of mean.

The main effect diagram illustrates the relative influence of each irradiation parameter on the response TON across its investigated range. In this system, the duty cycle exerts the largest effect, closely followed by the LED current, while the pulse frequency shows the smallest, yet still significant, influence. Increased energy input, realized through higher LED currents and longer duty cycles, correlates with higher TONs. In contrast, shorter pulse frequencies are favoured under the conditions investigated. Note that for **{Mo$_3$}**, previous studies identified the LED current as the dominant factor, followed by the duty cycle, with the on/off frequency exerting the weakest influence on the system. This confirms that, while the relative ranking of duty cycle and LED current differs between **{Mo$_2$}** and **{Mo$_3$}**, the pulse frequency consistently has the lowest impact.[182] In addition to the individual effects of each parameter, interdependencies (also called interactions) between factors may also occur. In this context, interdependency means that the effect

of one parameter on the response depends on the level of another parameter.[155] Such interactions can be identified and visualized using an interaction diagram (Figure 36).

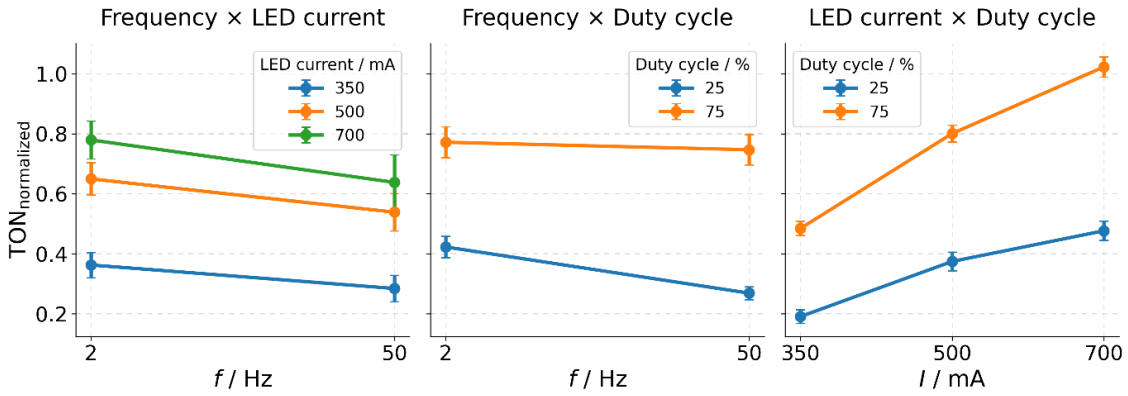

Figure 36: Interaction diagram to explore interdependence of two parameters. Left: average normalized TONs vs. on/off frequency for different LED currents; center: average normalized TONs vs. on/off frequency for different duty cycles; Right: average normalized TONs vs. LED current for different duty cycles. Error bars represent standard error of mean.

In an interaction diagram, the response (TON) is plotted as a function of one parameter at the different levels of a second parameter. If the lines in such a plot are parallel, no interaction between the two parameters is present. In contrast, converging, diverging, or intersecting lines indicate a statistically relevant interaction. In the present system, clear interactions are observed between pulse frequency and duty cycle, as well as between LED current and duty cycle.

The combination of frequency and duty cycle determines the absolute lengths of the light and dark periods. At 2 Hz, the total cycle length is 500 ms. With a duty cycle of 25%, the LED is switched on for 125 ms and off for 375 ms, whereas at 75% duty cycle it is on for 375 ms and off for 125 ms. At 50 Hz, the cycle length is 20 ms, resulting in 5 ms light and 15 ms dark at 25% duty cycle and 15 ms light and 5 ms dark at 75% duty cycle. These results demonstrate that not only the average energy input but also the temporal structure of light and dark phases has a measurable influence on the catalytic system. A comparable interaction between frequency and duty cycle was previously observed for the **{Mo$_3$}** system as well.[182]

The combination of LED current and duty cycle defines the time-averaged photon flux and thus the total energy input into the system. As expected, higher overall energy input generally correlates with higher TONs. However, the significant interaction between LED current and duty cycle shows that their effects are not simply additive. Some degradation

pathways might be enabled with longer photon irradiance (like two electron steps) at a time and therefore the normalized TONs are not in a linear correlation with the energy input.

An important measure of how much of the variation in TON can be explained by the chosen factors and their interactions is the coefficient of determination R^2, which reflects how well the statistical model fits the data.[155] In this work, R^2 was 90.41%, indicating that most of the observed variation in TON is accounted for by the irradiation parameters and their interdependencies. This supports that normalizing each experimental day to the static benchmark effectively minimizes day-to-day fluctuations due to unknown experimental errors (fluctuations are seen in the SI Table 15). The remaining ≈10% of the variation is most likely due to residual experimental variability, such as minor differences in sample preparation or reactor operation.

Analysis of the experimental design also allows identification of parameter settings that maximize TON. For the present data set, an LED current of 700 mA, a pulse frequency of 2 Hz, and a duty cycle of 75% were predicted as the optimum. The corresponding TON is expected to be only about 4% higher than under static benchmark conditions. Nevertheless, this setting improves the energy efficiency of the system, because a duty cycle of 75% reduces the energy input by 25% compared to continuous irradiation at 700 mA while still yielding more hydrogen. The resulting ratio of hydrogen evolved vs energy input is summarized in Table 13 and shows that the TON-optimized parameter set is more energy-efficient than the static benchmark experiment. The same parameter combination was previously identified as the TON optimum for the **{Mo_3}** system as well.[182]

Table 13: Normalized TON, energy input and TON-energy-ratio for standard and optimized irradiation settings.

Irradiation setting	**700 mA static**	**700 mA, 2 Hz, 75%**
$TON_{normalized}$	1.0	1.04 ± 0.09
Energy Input	65 mWh	48.75 mWh
$TON_{normalized}$ / Energy Input	0.15 mWh^{-1}	0.21 mWh^{-1}

To validate the optimization, three additional photocatalytic experiments were carried out under the predicted optimum irradiation conditions and again normalized to the static benchmark. The corresponding relative TON values are summarized in Table 16(SI). All

three values lie within the 95% prediction interval (0.84–1.24) obtained from the *Minitab 22* model, confirming the statistical robustness of the DoE-based prediction.

For assessing catalytic performance, not only the relative TON but also the efficient use of incident photons is relevant. Therefore, the PEs of the system under the different irradiation conditions were calculated. Here again, the PE was normalized to the measured benchmark experiment of the same day. The normalized PEs for the TON-optimized conditions and for the parameter set with the highest normalized PE are listed in Table 14; all remaining values are given in Table 17(SI). The absolute PEs obtained for **{Mo$_2$}** are on the order of 10^{-3} (see SI).

Table 14: Calculated normalized PEs for standard, TON-optimized irradiation settings and the irradiation setting with the highest PE found.

Setting	**PE$_{normalized}$**
700 mA static	1.0
700 mA, 2 Hz, 75%	1.4 ± 0.1
500 mA, 2 Hz, 25%	2.6 ± 0.4

Again, dynamic irradiation yields higher photonic efficiencies than static irradiation. However, the parameter set with the highest relative photonic efficiency is the combination of 500 mA LED current, 2 Hz pulse frequency, and a 25% duty cycle. Under these conditions, the relative photonic efficiency is more than doubled compared to the static benchmark experiment. For the **{Mo$_3$}** system, an analogous parameter combination was previously identified as optimal for maximizing photonic efficiency; the only difference is the pulse frequency, which was 50 Hz in that case.

While it is attractive from an application-oriented perspective that reduced energy input can still lead to higher TONs, this immediately raises the question of why this is the case. One working hypothesis is that the catalyst undergoes less photodegradation under dynamic irradiation due to the reduced effective photon flux. This mechanism was also proposed for the improved performance of the **{Mo$_3$}** system under dynamic irradiation.[182] Streb and colleagues used Raman spectroscopy to suggest that **{Mo$_2$}** does not appear to undergo the same disulfide ligand exchange processes as **{Mo$_3$}**.[116] However, in that study the samples were not irradiated during the Raman experiments.

In the present work, we investigated whether a light-induced ligand exchange or other structural changes occur for the **{Mo_2}** cluster, analogous to the behaviour previously observed for **{Mo_3}**.[148,182] UV–Vis spectroscopy was employed to monitor structural changes under irradiation. Degassed methanolic solutions of **{Mo_2}** were irradiated under static and dynamic conditions, and corresponding non-irradiated solutions were measured as controls. The time-dependent UV–Vis spectra show two isosbestic points under all conditions at $\lambda_{isos1} \approx 235$ nm and $\lambda_{isos2} \approx 260$ nm. This indicates that only one process is occurring. At the beginning of the measurements an absorption maximum is observed at 245 nm. Based on TD-DFT calculations of the **{Mo_2}** cluster, this band is linked to a ligand-to-ligand charge transfer (LLCT) from the bridging disulfide toward the terminal disulfide. The non-irradiated solution showed a decrease of the 245 nm signal with time, and an increase in absorption at ~212 nm. This indicates that even without irradiation, the cluster undergoes changes on the timescale of minutes to hours. The most plausible explanation for this observation is that the cluster undergoes an exchange of the terminal disulfide ligands for solvent (MeOH) ligands. DFT and TD-DFT calculations were carried out to assess the spectral properties of the ligand exchanged species $[Mo_2S_{12-x}(MeOH)_x]^{(2-x)-}$ (x= 2, 4, 6, 8). This data indicates the appearance of an absorption band at lower wavelengths compared to the initial **{Mo_2}** cluster, which is in line with the observed behaviour (see SI for details). The decay of the 245 nm absorption band and the increase of the 212 nm band over time is visualized in Figure 37.

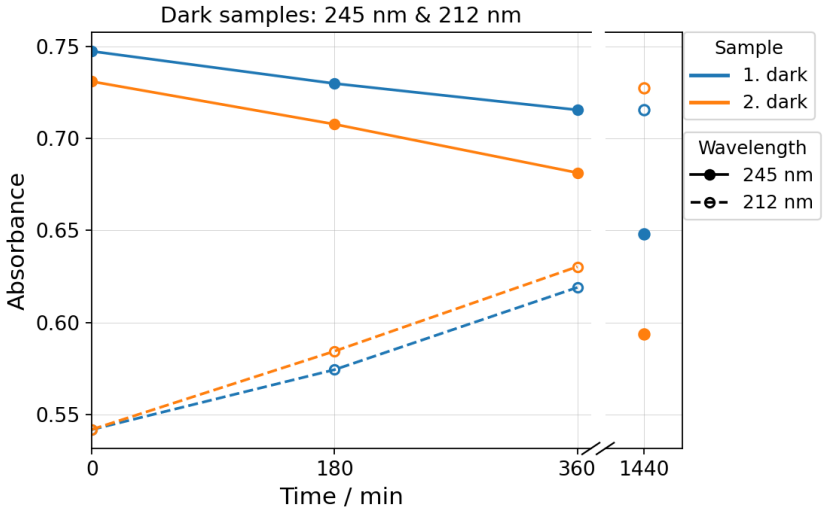

*Figure 37: Absorbance of non-irradiated **{Mo₂}** (c = 25 µM in MeOH) samples over time at detection wavelengths 245 nm and 212 nm.*

The new absorption band at 212 nm is building up in a similar way as the decrease of the 245 nm band. Assumed that the extinction coefficients are similar for the initial cluster and the ligand exchanged species, this supports the hypothesis that a ligand exchange is slowly happening. Rajagopal et al. already investigated possible terminal ligand exchange in earlier studies.[127] Using Raman spectroscopy they found that **{Mo₂}** undergoes ligand exchange very slowly.[127]

In contrast, the irradiated samples displayed a more rapid decrease of the absorption maximum at 245 nm and the growth of a new band at ca. 227 nm. The formation of new and different absorption maxima, depending on sample irradiation, indicates that the cluster undergoes different structural changes when irradiated. For both cases, the appearance of new bands gives evidence for electronic changes of the cluster and the different band positions indicate that different species are formed with and without irradiation. After 24 h an decrease of absorption over all wavelengths can be observed, indicating complete photodegradation of the cluster. It appears that this is a subsequent process following the initial structural changes. Based on the consideration that species with different electronic properties are formed upon irradiation, it can also be hypothesized that the cluster collects charges in form of electrons when it is irradiated and excited. Irradiation for extended periods might lead to increased charge-accumulation at the catalyst which in turn accelerate loss or degradation of terminal

disulfide ligands, resulting in faster deactivation. A similar behaviour was found for the **{Mo$_3$}** cluster in similar studies.[182] This hypothesis is in line with the observed interdependency between the LED current (photon irradiance) and the duty cycle (irradiation period) found under catalytic conditions. With high photon irradiance for a longer time charges accumulate and lead to cluster degradation. Sufficiently long dark times in between irradiation periods might avoid too much accumulated charges. Therefore, photonic efficiencies are also higher with lower photon irradiance. For TiO_2 a similar photo charging behaviour is known as well and for this semiconductor the number of stored charges reaches a limit after a certain time. For long irradiation times the charging and discharging processes are equally fast, eventually leading to a loss of efficiency.[184]

To rationalize if the decay of the 245 nm band is influenced by different irradiation conditions and if this might explain the results found for improved catalytic performance under dynamic irradiation, the decay of the 245 nm band and the increase of the 227 nm band were plotted as a function of time (Figure 38).

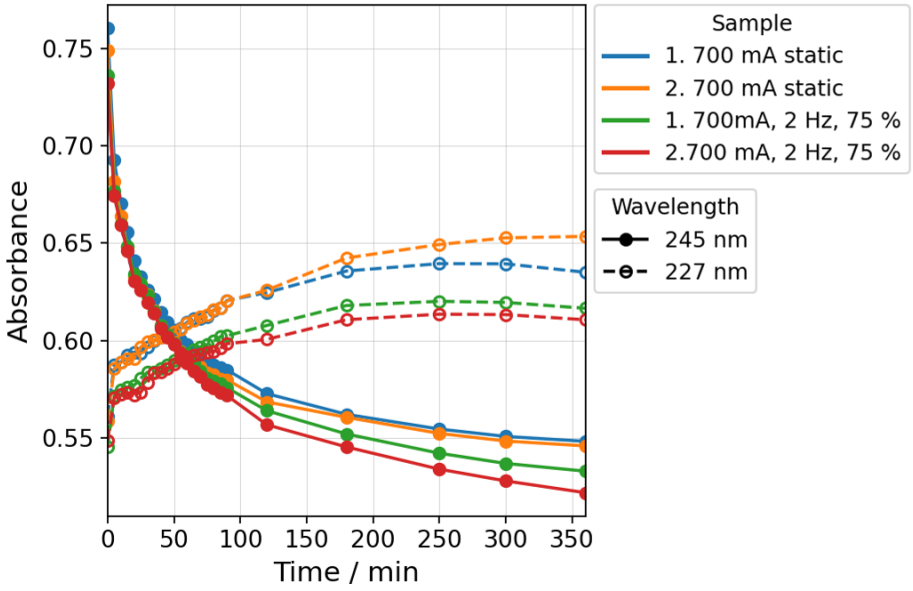

*Figure 38: Time dependent absorbances of **{Mo$_2$}** (c = 25 µM in MeOH) under static and dynamic irradiation for 245 nm and 227 nm.*

No significant differences in the decay behaviour were observed between static and dynamic irradiation. This indicates that dynamic irradiation does not substantially alter the overall photodegradation pathway of **{Mo$_2$}**. This finding is consistent with the observation

that the TON remains comparable under static and dynamic irradiation. For the 227 nm band a consistently higher absorbance is observed for the static irradiation in comparison to the dynamic one, while the general trend mirrors the decay of the 245 nm band. This difference for the different irradiation conditions hints on a slightly lower mean concentration of the traced species during dynamic irradiation. This observation supports the hypothesis outlined above that the **{Mo$_2$}** is charged upon irradiation, which eventually opens an electron loss channel. Thus, limiting the number of accumulated charges by lowering the time-averaged absorbed number of photons, by either reducing the photon irradiance or increasing the length of dark periods, leads to a more efficient use of photons, i.e. a higher photonic efficiency.

Conclusion

This study closes a key knowledge gap by demonstrating that dynamically modulated irradiation protocols can beneficially tune the performance metrics of the homogeneous **{Mo$_2$}** light-driven HER system. Using a DoE strategy, we quantitatively identified duty cycle and LED current as the primary drivers of catalytic turnover, with pulse frequency exerting a smaller but measurable influence. Importantly, significant interactions between duty cycle and both frequency and LED current indicate that not only the average energy input, but also the temporal structure of light and dark phases, governs the observed activity. Under the DoE-predicted TON optimum (700 mA, 2 Hz, 75% duty cycle), **{Mo$_2$}** reaches a slightly higher normalized TON than static irradiation while requiring 25% less energy input, resulting in a clearly improved TON-to-energy ratio. In parallel, dynamic conditions can substantially increase photonic efficiency, with the best normalized PE found at lower average photon input (500 mA, 2 Hz, 25% duty cycle). Mechanistically, time-resolved UV–Vis spectroscopy reveals that **{Mo$_2$}** undergoes chemical changes even without irradiation, consistent with slow solvent-induced ligand exchange as supported by TD-DFT-derived spectral trends. Under irradiation, the spectral evolution differs (formation of a band at ~227 nm), pointing to a distinct photoinduced pathway and/or electronic-state changes. However, the similar decay behaviour at 245 nm under static and dynamic irradiation suggests that—unlike in related **{Mo$_3$}** systems—dynamic irradiation does not strongly suppress the dominant degradation/activation pathway of **{Mo$_2$}** under the conditions studied, which rationalizes the comparatively modest TON

gain. Based on the changes of the UV-Vis spectra, the observed increase in photonic efficiency was reasoned by an accumulation of charges on the cluster, which leads to cluster degradation when a too high charging state is reached.

Overall, our results establish dynamic irradiation as a practical handle to improve energy and photon utilization in **{Mo_2}** based HER without requiring changes to catalyst structure. Future work should focus on identifying the molecular nature of the photo-generated species responsible for the ~227 nm band, and on operando/in situ spectroscopy under catalytic conditions to directly

Supporting Information

Instrumentation

Attenuated total reflectance-Fourier-transformed infrared spectroscopy (ATR-FT-IR) was performed using a Bruker Alpha II equipped with an ATR Platinum Diamond unit. The data were recorded with 24 scans at a resolution of 4 cm^{-1}. All spectra were background-corrected within the Bruker OPUS 8.1 program suite.

UV/Vis/NIR spectroscopy was performed on a Cary 3500 UV/Vis/NIR spectrophotometer equipped with a Xenon flash lamp (250 Hz). Measurements were performed in screw cap quartz glass cuvettes (d = 10.0 mm) with rubber septa.

Gas chromatography was performed on a Shimadzu Nexis GC-2030 equipped with a BID detector and a split injection unit with a split ratio of 1:20. Helium was chosen as the carrier gas. The column was heated to a constant temperature of 80℃.

Chemicals: All chemical reagents were obtained commercially and used as received unless stated otherwise. $(NH_4)_2[Mo_2S_{12}]$ was prepared according to the literature.[172]

Vials: glass vials for catalytic measurements were purchased from Biotage with crimp caps made of aluminum with silicon rubber/PTFE septa. Outer diameter: 17 mm, inner diameter: 15 mm, length: 85 mm, volume: ~11.0 mL

Experimental Data

Synthesis of $(NH_4)_2[Mo_2S_{12}]$

The synthesis of $(NH_4)_2[Mo_2S_{12}]$ is based on a procedure by MÜLLER et al.[172]

$(NH_4)_6[Mo_7O_{24}]\times 4H_2O$ (2.18 g, 1.78 mmol) was dissolved in 20 mL of deionized water and $NH_2OH\times HCl$ (1.55 g, 22 mmol) was dissolved in 15 ml of water. Both solutions were combined, which formed a yellow solution to which 20 mL of ammonium polysulfide (22 wt% aq) were added. The mixture was stirred at 50 °C for one hour. During heating the yellow mixture gained a dark red color. After cooling the reaction mixture to room temperature, the solution was filtered and transferred to a Schlenk-flask and heated to 90 °C for five hours under nitrogen. After cooling the dark brown solution was stirred

overnight under nitrogen during which a black precipitate was formed. The solid was filtered and washed with 20 mL ice-cold water and 60 mL isopropanol. In order to remove the excess sulfur, the product was washed with 20 mL of carbon disulfide solution and 40 mL of diethylether.

Yield: 1.04 g (1.60 mmol, 26% based on Mo-atoms)

UV-Vis bands (nm in MeOH): λ_{max} = 270 nm

$\lambda_{shoulder}$ = 380 nm

ATR-FTIR bands (cm-1): 520 (s), 1370(s)

Sample preparation

HER Catalysis: For each component a stock-solution with set concentrations was prepared: the catalyst $(NH_4)_2[Mo_2S_{12}]$ (c = $5 \cdot 10^{-4}$ M), the photosensitizer $[Ru(bpy)_3](PF_6)_2$ (c = $1 \cdot 10^{-5}$ M), and the sacrificial electron donor (SED) (sodium ascorbate and ascorbic acid, molar ratio: 4:5, c = $1.25 \cdot 10^{-2}$ M). The stock solutions were prepared in methanol. Before preparation of the catalytic reaction mixture, the catalyst stock solution was diluted with methanol or water respectively by a factor of 100. The diluted catalyst solution, along with the respective stock solutions of the PS and SED and the appropriate solvents, were combined in crimp vials resulting in a total solution volume of 4 mL per vial. The resulting concentrations of the compounds were: c(CAT) = 0.5 µM, c(PS) = 20 µM, c(SED) = 10 mM. The vials were sealed using aluminum crimp caps with silicone/PTFE septa and purged with nitrogen for 60 min. To prevent leakage, the septa were sealed with clear nail polish.

UV/Vis Measurements: The samples for the UV/Vis measurements were prepared by dissolving the catalyst (25 µM) in 2.5 mL methanol in a 4 mL quartz cuvette. The resulting solution was purged with N_2-gas for approximately 15 min before being transferred to the spectrometer for analysis or to the photoreactor for irradiation. For the first 90 min, every five minutes a spectrum was recorded and later only after 120, 180, 240, 300 and 360 min of irradiation.

Gas chromatographic measurements

HER Catalysis: The respective samples were placed in a custom-designed photoreactor,[144] and irradiated using a LED (λ_{max} =465 nm). Twelve samples were prepared each day. Three

samples went into each photoreactor and each irradiation setting was repeated three times, so that for each parameter combination nine values were measured to ensure reproducibility and allow statistic error determination. Before starting the GC measurements, at least two air measurements were conducted to verify a stable baseline. Sample collection was carried out using a Model 710 RN syringe from Hamilton. The nail polish covering the septum was removed using a spatula before inserting the syringe through the septum to withdraw 100 µL of gas. A single measurement was taken after 300 min of irradiation.

Irradiation setup

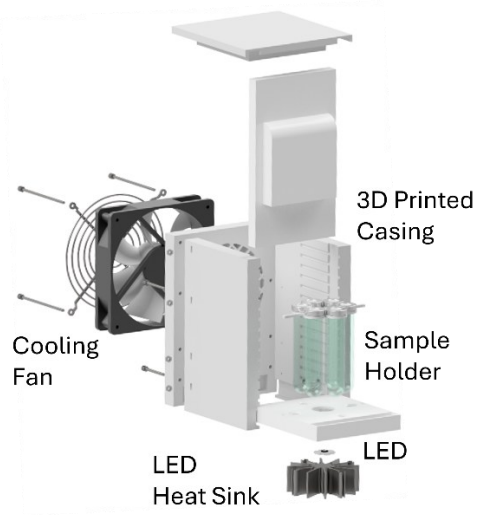

Figure 39: Illustration of the photoreactor.

All samples were irradiated in modular 3D printed photoreactors (Figure 39) designed by Kowalczyk et al.[144] The LED (λmax = 465 nm) is connected with a LED driver which determines the current powering the LED. Attached to the driver is a power supply unit and an In/Out-bricklet. The In/Out-bricklet enables to send different signals to different outlets and the inlet is a masterbrick which is connected to a laptop. On the laptop a self-written python script is run and controls the frequency and the duty cycle of the pulsed signals.

The 90x90x140 mm modular photoreactor was chosen for these experiments and printed with white PETG. The vial holder was placed in the 10th vertical holder slot above the LED and the lower distance between the bottom of the reactor and the vials bottom was 22 mm. The radius of the holder was 43 mm.

An instruction manual and CAD files to print the reactor and controller units as well as the python script that was used in the controller unit to set frequency and duty cycle can be found here:

https://github.com/photonZfeed/modularPhotoreactor

Information about the used LED:

https://look.ams-osram.com/m/6208f3ef096a8da0/original/LZ1-10B202.pdf

https://look.ams-osram.com/m/77b624bf9a989535/original/LZ1-00B202.pdf

Data Processing

Turnover number (TON):

To determine the TON, the volume of the gas phase in the vial was calculated using the following equation:

$$V_{gas} = V_{vial} - V_{sol} \quad [19]$$

V_{gas}*:* gas volume of the vial. V_{vial}: total volume of the vial. V_{sol}: volume of the catalytic solution. The sample volume taken is 100 µL. To calculate the absolute amount of hydrogen evolved a vial-specific factor k_{vial} is calculated using equation 20 (to account for the amount of gas extracted for the GC-measurement):

$$k_{vial} = \frac{V_{gas}}{100\ \mu L} \quad [20]$$

The absolute amount of hydrogen evolved $H_{2,abs}$ can then be determined using the determined amount of hydrogen $n_{measured}$ per 100 µL, using the following equation:

$$n_{H_2,abs} = n_{measured} \cdot k_{vial} \quad [21]$$

The TON is the ratio of the amount of hydrogen formed $H_{2,abs}$ and the amount of catalyst in the solution n_{CAT}:

$$TON = \frac{n_{H_2,abs}}{n_{CAT}} \quad [22]$$

To diminish day-to-day fluctuations the TON of the individual settings were normalized to the average TON of the benchmark experiment of that day:

$$\mathrm{TON}_{\mathrm{normalized}} = \frac{\mathrm{TON}_{\mathrm{individual\ setting,day}}}{\mathrm{TON}_{\mathrm{700mA,static,day}}} \qquad [23]$$

Table 15: Normalized TON for each measurement day and individual irradiation settings. The three $TON_{normalized}$ represent the three individual samples in a photoreactor. The average TON of the bench-mark experiment for the individual days are also given.

	Day 1 TON(700 mA stat) = 673			Day 2 TON(700 mA stat) = 929		
Setting	500 mA, 2 Hz, 25%	700 mA, 2 Hz, 25%	700 mA, 50 Hz, 75%	700 mA, 50 Hz, 75%	500 mA, 0 Hz, 100%	500 mA, 50 Hz, 25%
$TON_{normalized}$ 1	0.516	0.697	0.887	1.210	1.020	0.307
$TON_{normalized}$ 2	0.504	0.503	0.881	0.970	0.974	0.401
$TON_{normalized}$ 3	0.210	0.471	0.895	1.172	0.959	0.224
	Day 3 TON(700 mA stat) = 895			Day 4 TON(700 mA stat) = 1018		
Setting	500 mA, 50 Hz, 75%	700 mA, 2 Hz, 75%	500 mA, 2 Hz, 75%	500 mA, 50 Hz, 75%	700 mA, 2 Hz, 75%	500 mA, 2 Hz, 75%
$TON_{normalized}$ 1	1.156	1.130	1.220	0.759	0.714	0.940
$TON_{normalized}$ 2	0.854	1.219	1.013	0.830	1.037	0.823
$TON_{normalized}$ 3	0.939	1.309	0.315	0.889	0.968	0.802
	Day 5 TON(700 mA stat) = 978			Day 6 TON(700 mA stat) = 966		
Setting	700 mA, 50 Hz, 25%	500 mA, 2 Hz, 25%	700 mA, 2 Hz, 25%	500 mA, 50 Hz, 25%	700 mA, 50 Hz, 25%	500 mA, 0 Hz, 100%
$TON_{normalized}$ 1	0.506	0.654	0.646	0.252	0.273	0.804
$TON_{normalized}$ 2	0.620	0.440	0.502	0.202	0.356	0.679
$TON_{normalized}$ 3	0.336	0.477	0.546	0.259	0.379	0.769
	Day 7 TON(700 mA stat) = 1273			Day 8 TON(700 mA stat) = 1286		
Setting	500 mA, 2 Hz, 75%	500 mA, 0 Hz, 100%	500 mA, 2 Hz, 25%	500 mA, 50 Hz, 75%	700 mA, 2 Hz, 25%	700 mA, 2 Hz, 75%
$TON_{normalized}$ 1	0.780	0.733	0.474	0.855	0.532	0.974
$TON_{normalized}$ 2	0.763	0.819	0.411	0.651	0.592	0.948

$TON_{normalized}$ 3	0.787	1.043	0.360	0.703	0.700	1.007
	Day 9 TON(700 mA stat) = 370			Day 10 TON(700 mA stat) = 317		
Setting	700 mA, 50 Hz, 25%	500 mA, 50 Hz, 25%	500 mA, 50 Hz, 75%	350 mA, 2 Hz, 75%	350 mA, 50 Hz, 25%	350 mA, 0 Hz, 100%
$TON_{normalized}$ 1	0.355	0.379	0.672	0.576	0.251	0.270
$TON_{normalized}$ 2	0.365	0.242	0.554	0.565	0.119	0.205
$TON_{normalized}$ 3	0.345	0.263	0.337	0.374	0.108	0.279
	Day 11 TON(700 mA stat) = 468			Day 12 TON(700 mA stat) = 405		
Setting	350 mA, 2 Hz, 25%	350 mA, 50 Hz, 75%	350 mA, 0 Hz, 100%	350 mA, 2 Hz, 25%	350 mA, 50 Hz, 75%	350 mA, 50 Hz, 25%
$TON_{normalized}$ 1	0.153	0.359	0.572	0.093	0.000	0.166
$TON_{normalized}$ 2	0.075	0.434	0.481	0.203	0.005	0.087
$TON_{normalized}$ 3	0.246	0.423	0.564	0.397	0.005	0.000
	Day 13 TON(700 mA stat) = 462			Day 14 TON(700 mA stat) = 398		
Setting	350 mA, 50 Hz, 25%	350 mA, 0 Hz, 100%	350 mA, 50 Hz, 75%	350 mA, 2 Hz, 75%	350 mA, 2 Hz, 25%	350 mA, 2 Hz, 75%
$TON_{normalized}$ 1	0.079	0.532	0.457	0.691	0.190	0.470
$TON_{normalized}$ 2	0.231	0.439	0.471	0.519	0.317	0.381
$TON_{normalized}$ 3	0.232	0.503	0.563	0.451	0.293	0.533

Due to delayed hardware delivery all measurements for a 350 mA LED current were performed later in time. Values marked in red cells represent values that were identified as outliers by the *Minitab 22* software.

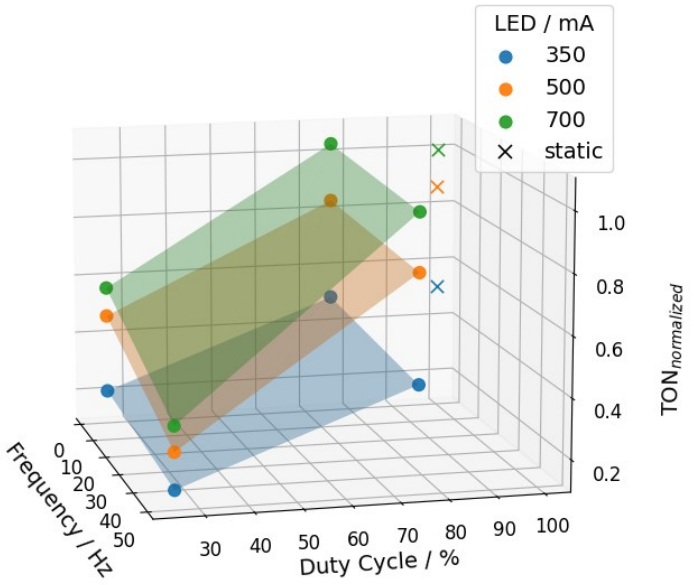

Figure 40: Additional 3D-plot of the TON vs. Duty cycle and frequency for different LED currents for visualization.

Table 16: Normalized TONs measured to verify predicted values under TON optimized irradiation setting.

	700 mA, 2 Hz, 75%
$TON_{normalized}$ 1	1.219
$TON_{normalized}$ 2	1.002
$TON_{normalized}$ 3	0.977

Photonic Efficiency

The photonic efficiency PE is determined using the photonic irradiance q which is calculated based on the experimentally determined power P of the LED, the emission wavelength λ, the Planck constant h, the speed of light c and the Avogadro constant N_A.[173]

$$q = \frac{P \cdot \lambda}{h \cdot c \cdot N_A} \qquad [24]$$

The total number of photons n_{ph} can be calculated by multiplying the photonic irradiance q with the time t and the duty cycle (0.25 or 0.75) and the area A_{Vial} of the vial (= 1.227 cm^2).

$$n_{ph} = q \cdot t \cdot \mathrm{dc} \cdot A_{\mathrm{Vial}} \qquad [25]$$

The PE is calculated using equation [26].

$$\mathrm{PE} = \frac{n_{\mathrm{H_2,abs}}}{n_{\mathrm{ph}}} \qquad [26]$$

The PE was then normalized analogous to the TON to diminish day-to day differences by dividing with the benchmark experiment performed on that same day:

$$\mathrm{PE_{normalized}} = \frac{\mathrm{PE_{individual\ setting,day}}}{\mathrm{PE_{700mA,static,day}}} \qquad [27]$$

Table 17: Normalized PE for each measurement day and individual irradiation settings. The three $PE_{normalized}$ represent the three individual samples in a photoreactor. The values that were identified as outliers before were not considered here.

	Day 1 PE(700mA stat) = 1.33 ·10^{-3}			Day 2 PE(700mA stat) = 1.74 ·10^{-3}		
Setting	500 mA, 2 Hz, 25%	700 mA, 2 Hz, 25%	700 mA, 50 Hz,75 %	700 mA, 50 Hz, 75%	500 mA, 0 Hz, 100%	500 mA, 50 Hz, 25%
$PE_{normalized}$ 1	2.70	2.63	1.12	1.61	1.11	1.70
$PE_{normalized}$ 2	2.63	1.90	1.11	1.29	0.94	2.22
$PE_{normalized}$ 3	-	1.78	1.13	1.56	1.06	1.24
	Day 3 PE(700mA stat) = 1.68 ·10^{-3}			Day 4 PE(700mA stat) = 1.86 ·10^{-3}		
Setting	500 mA, 50 Hz, 75%	700 mA, 2 Hz, 75%	500 mA, 2 Hz, 75%	500 mA, 50 Hz, 75%	700 mA, 2 Hz, 75%	500 mA, 2 Hz, 75%
$PE_{normalized}$ 1	-	1.51	-	1.40	-	1.73
$PE_{normalized}$ 2	1.57	1.62	1.87	1.53	1.38	1.52
$PE_{normalized}$ 3	1.73	-	-	1.64	1.29	1.48
	Day 5 PE(700mA stat) = 1.83 ·10^{-3}			Day 6 PE(700mA stat) = 1.76 ·10^{-3}		
Setting	700 mA, 50 Hz, 25%	500 mA, 2 Hz, 25%	700 mA, 2 Hz, 25%	500 mA, 50 Hz, 25%	700 mA, 50 Hz, 25%	500 mA, 0 Hz, 100%
$PE_{normalized}$ 1	1.98	3.54	2.53	1.39	1.09	1.41
$PE_{normalized}$ 2	-	2.38	1.96	1.12	1.42	1.35
$PE_{normalzed}$ 3	1.31	2.58	2.14	1.43	1.51	1.33
	Day 7 PE(700mA stat) = 2.83 ·10^{-3}			Day 8 PE(700mA stat) = 2.41 ·10^{-3}		

Setting	500 mA, 2 Hz, 75%	500 mA, 0 Hz, 100%	500 mA, 2 Hz, 25%	500 mA, 50 Hz, 75%	700 mA, 2 Hz, 25%	700 mA, 2 Hz, 75%
$PE_{normalized}$ 1	1.44	1.01	2.62	1.58	2.13	1.30
$PE_{normalized}$ 2	1.41	1.13	2.27	1.20	2.37	1.26
$PE_{normalized}$ 3	1.45	1.44	1.99	1.30	2.80	1.34
	Day 9 PE(700mA stat) = $0.72 \cdot 10^{-3}$			Day 10 PE(700mA stat) = $0.59 \cdot 10^{-3}$		
Setting	700 mA, 50 Hz, 25%	500 mA, 50 Hz, 25%	500 mA, 50 Hz, 75%	350 mA, 2 Hz, 75%	350 mA, 50 Hz, 25%	350 mA, 0 Hz, 100%
$PE_{normalized}$ 1	1.38	2.03	1.20	1.45	1.89	-
$PE_{normalized}$ 2	1.42	1.30	0.99	1.42	0.90	-
$PE_{normalized}$ 3	1.34	1.41	-	0.94	0.81	-
	Day 11 PE(700mA stat) = $0.88 \cdot 10^{-3}$			Day 12 PE(700mA stat) = $0.77 \cdot 10^{-3}$		
Setting	350 mA, 2 Hz, 25%	350 mA, 50 Hz, 75%	350 mA, 0 Hz, 100%	350 mA, 2 Hz, 25%	350 mA, 50 Hz, 75%	350 mA, 50 Hz, 25%
$PE_{normalized}$ 1	1.15	0.90	1.08	0.70	-	1.25
$PE_{normalized}$ 2	0.57	1.09	0.91	1.53	-	0.66
$PE_{normalized}$ 3	1.85	1.06	1.06	2.99	-	-
	Day 13 PE(700mA stat) = $0.85 \cdot 10^{-3}$			Day 14 PE(700mA stat) = $0.73 \cdot 10^{-3}$		
Setting	350 mA, 50 Hz, 25%	350 mA, 0 Hz, 100%	350 mA, 50 Hz, 75%	350 mA, 2 Hz, 75%	350 mA, 2 Hz, 25%	350 mA, 2 Hz, 75%
$PE_{normalized}$ 1	0.60	1.00	1.15	1.74	1.43	1.18
$PE_{normalized}$ 2	1.74	0.83	1.18	1.30	2.39	0.96
$PE_{normalized}$ 3	1.75	0.95	1.41	1.13	2.21	1.34

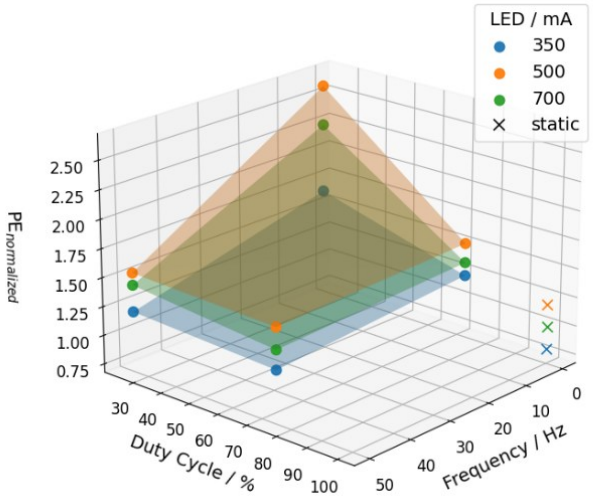

Figure 41: Additional 3D-plot of the PE vs. Duty cycle and frequency for different LED currents for visualization.

LED Power Determination

To measure the power of the LED a PM400 Optical Power Meter by Thorlabs was used. Power was measured at five or six positions of the photoreactor for different currents in duplicate or triplicate. The chosen positions were in radial order and at a height comparable to bottom of the sample flasks.

Table 18: Average LED power for different current supplies and the corresponding photon irradiance q (calculated using equation 24). All values are only given for the area of 1 cm^2 of the detector.

I_{LED} (mA)	P_{LED} (mW)	ΔP_{LED} (mW)	q (nmol s^{-1} cm^{-2})	Δq (nmol s^{-1} cm^{-2})
350	6.9	± 1.0	27	± 4
500	9.4	± 1.0	37	± 4
700	13.0	± 1.0	51	± 4

UV-Vis spectroscopy

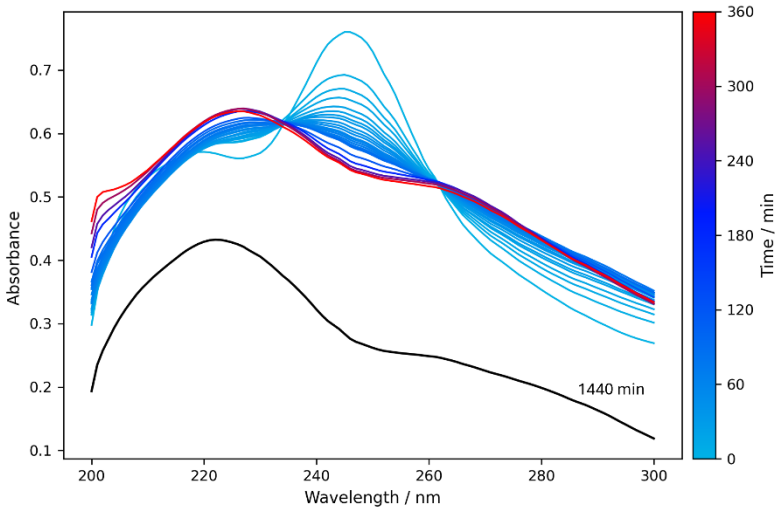

Figure 42: First time-dependent UV-Vis spectra of ***{Mo₂}*** *(c = 25 µM) in MeOH irradiated under 700 mA, static condition.*

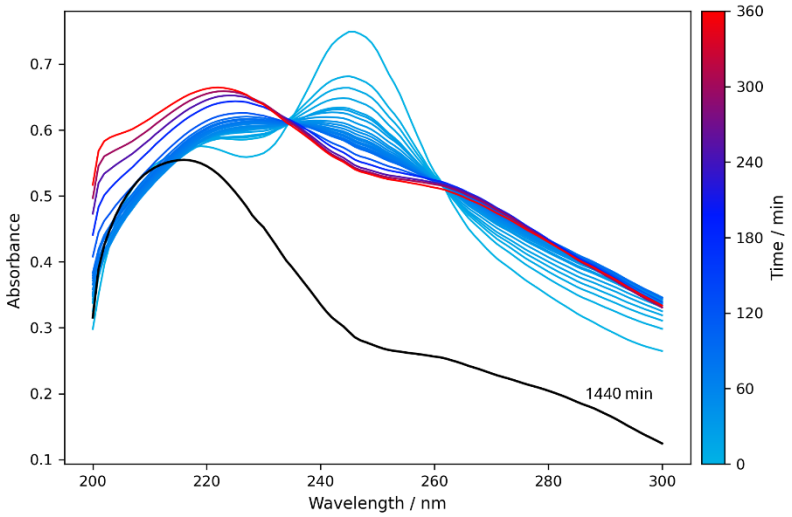

Figure 43:Second time-dependent UV-Vis spectra of ***{Mo₂}*** *(c = 25 µM) in MeOH irradiated under 700 mA, static condition.*

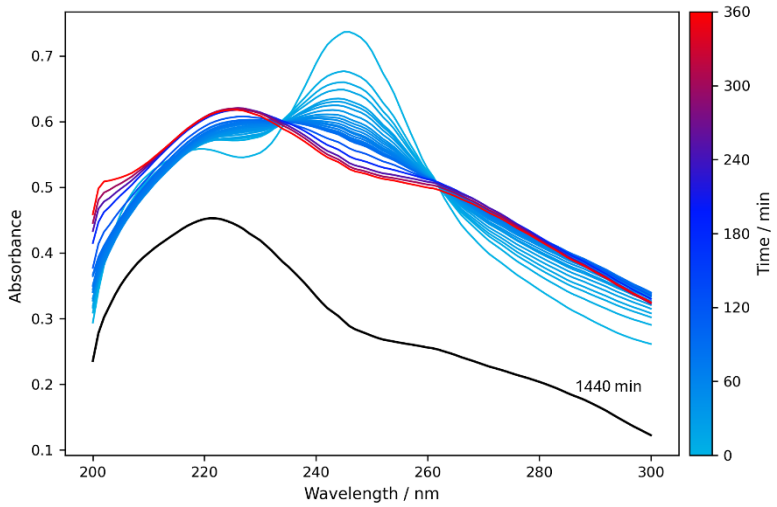

Figure 44: First time-dependent UV-Vis spectra of ***{Mo$_2$}*** *(c = 25 µM) in MeOH irradiated under 700 mA, 2 Hz, 75 % condition.*

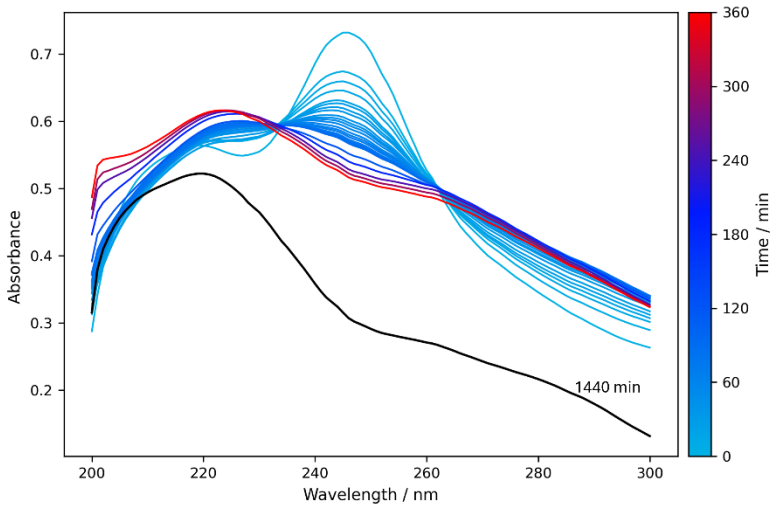

Figure 45: Second time-dependent UV-Vis spectra of ***{Mo$_2$}*** *(c = 25 µM) in MeOH irradiated under 700 mA, 2 Hz, 75 % condition.*

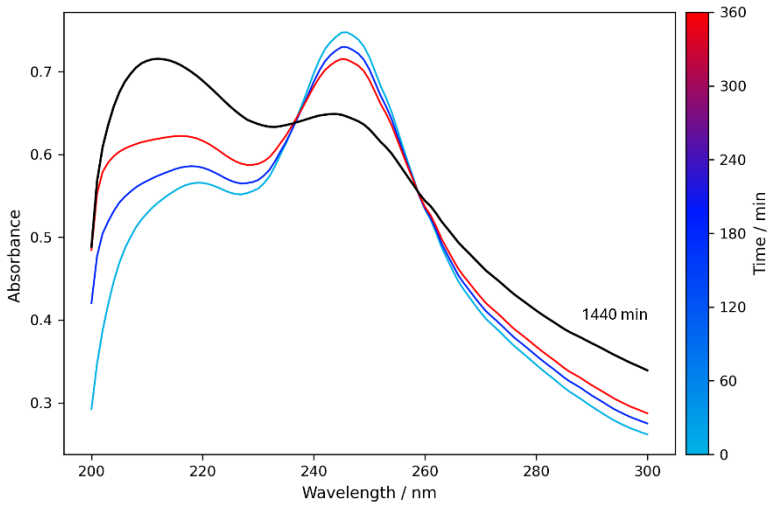

*Figure 46: First time-dependent UV-Vis spectra of **{Mo₂}** (c = 25 µM) in MeOH not irradiated.*

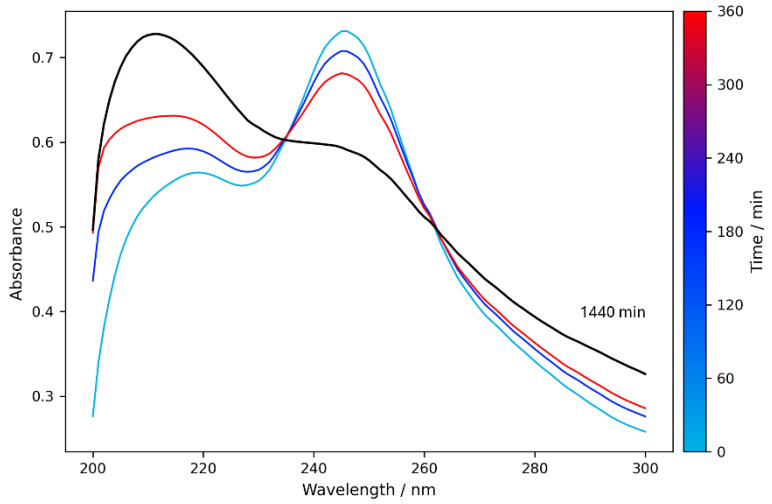

*Figure 47: Second time-dependent UV-Vis spectra of **{Mo₂}** (c = 25 µM) in MeOH not irradiated.*

Computational Data

The ORCA 6.1.[175] computational software was used to evaluate the structural and electronic properties of **{Mo₂}**, $[Mo_2S_{10}(MeOH)_2]^0$, $[Mo_2S_8(MeOH)_4]^{2+}$, $[Mo_2S_6(MeOH)_6]^{4+}$, $Mo_2S_4(MeOH)_8]^{6+}$ in the singlet state, as well as subsequently the photophysical properties associated with the (dipole-allowed) transitions underlying the UV-Vis bands. This work used the Becke 3-Parameter Lee-Yang-Parr (B3LYP)[176] at the hybrid level of theory for all ground state calculations, i.e., optimization and frequency analysis. This functional was chosen based on previous studies of similar systems.[148] The **def2 type**basis set of triple-zeta quality within the valence region, with an additional polarization function (**def2-**

TZVP)[177], was employed together with **Grimme's D3BJ dispersion correction** to account for longer-range interactions.[178,179] The **effective core potentials (ECPs)** for molybdenum were likewise taken from the ORCA 6.1 implementation.[180] Implicit solvation effects in **water** and **methanol** were included in all calculations using the **CPCM continuum model**[185], which treats the bulk solvent as a conductor-like polarizable continuum with the defined dielectric constant of methanol. For the TD-DFT calculations specifically, the lowest energy singlet-singlet 100 transitions are calculated per structure. The excited states obtained from the TD-DFT calculations were analyzed using the TheoDORE program package.[186] A chemically motivated, user-defined fragmentation scheme was employed to decompose the excited states, distinguishing metal centers, bridging disulfide ligands, and terminal disulfide or methanol ligands. The excited states were divided into metal-centered, ligand-centered, and ligand-to-ligand or metal–ligand charge-transfer contributions. Within the ligand-to-ligand charge-transfer (LLCT) contributions, LLCT1 corresponds to charge transfer from the bridging disulfide ligands to the terminal methanol ligands, whereas LLCT2 denotes charge transfer from the terminal disulfide or methanol ligands to the bridging disulfide units. Analogous definitions apply to the MLCT and LMCT contributions.

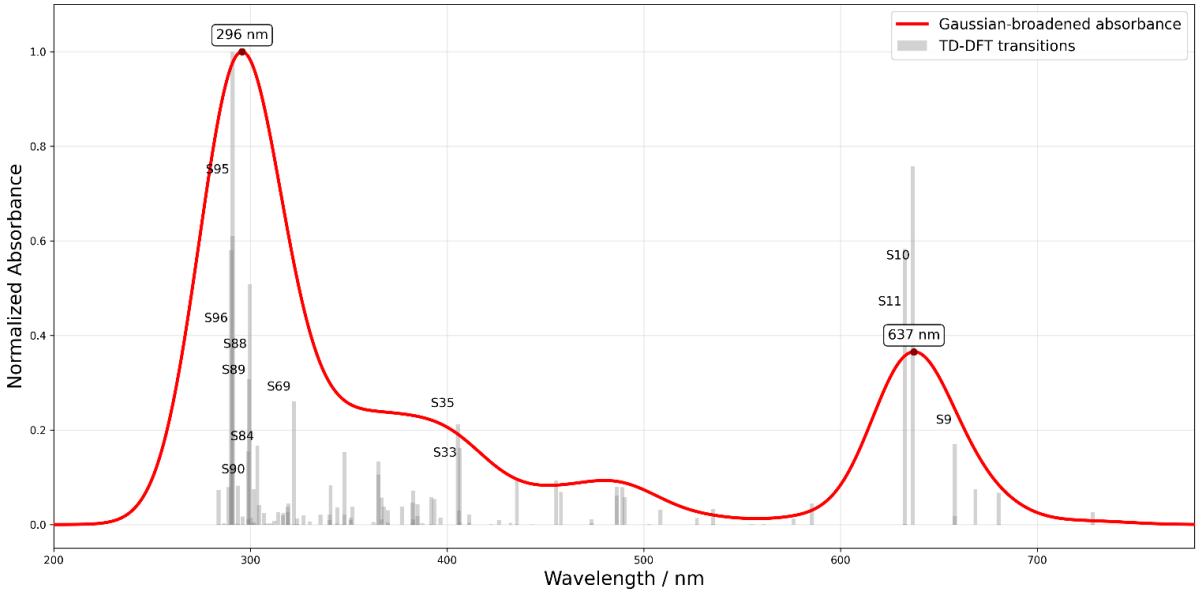

*Figure 48: TD-DFT-simulated UV–Vis spectrum of the **{Mo₂}** and corresponding vertical electronic transitions. The spectrum was generated by Gaussian broadening of the TD-DFT stick spectrum using oscillator-strength-weighted Gaussians (σ = 20 nm).*

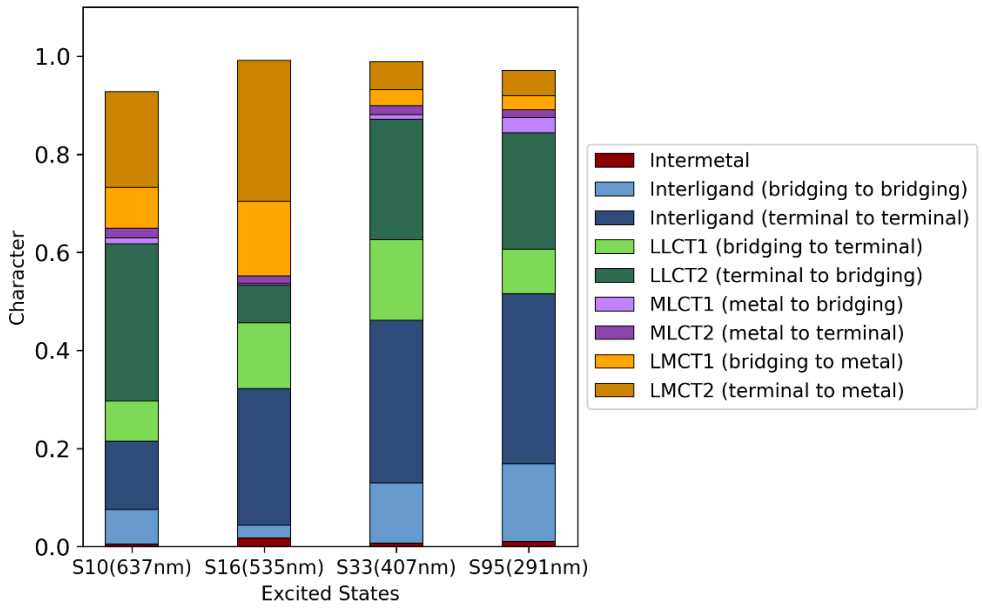

*Figure 49: Decomposition of the most relevant excited states of **{Mo₂}**[SK7.1]. The excited-state wave functions were decomposed into metal-centered, ligand-centered, and charge-transfer (LLCT, MLCT, LMCT) contributions using TheoDORE based on a chemically motivate.*

*Table 19: Electronic character of selected singlet excited states of **{Mo₂}**. Charge-density difference plots were generated for individual TD-DFT excitations, with each image depicting one excited state. Electron den-sity depletion and accumulation upon excitation are shown in purple and red, respectively.*

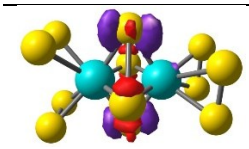	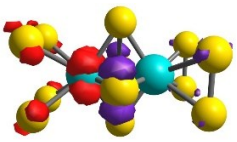	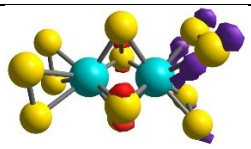	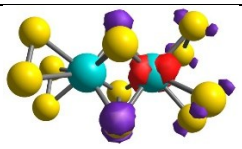
S_{10}, LLCT	S_{16}, LMCT	S_{33}, LLCT	S_{95}, LLCT

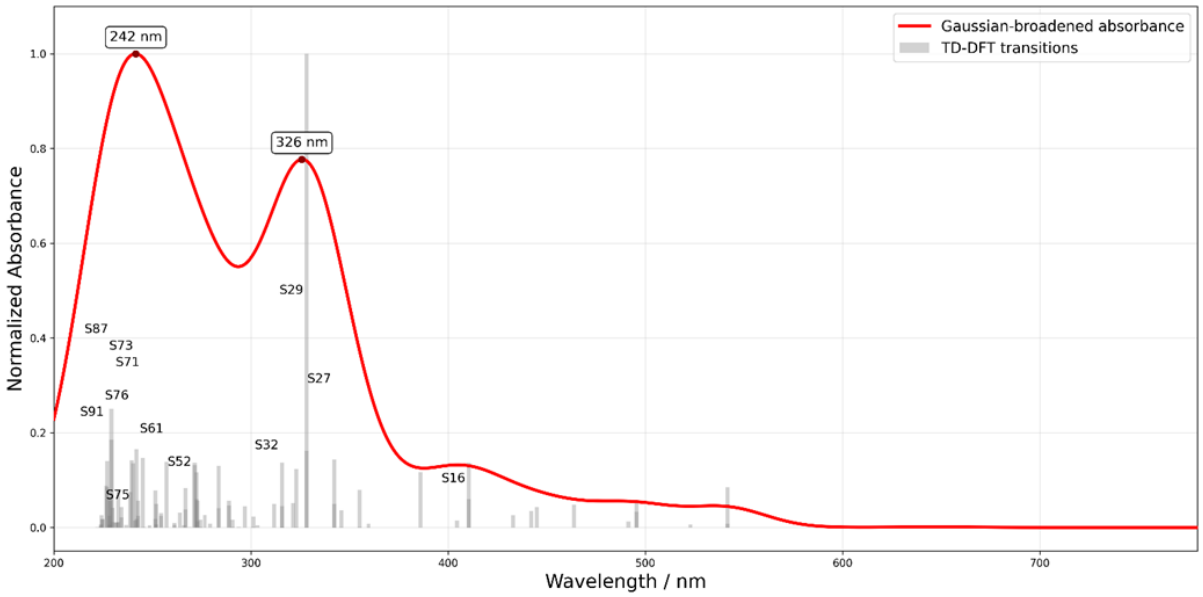

Figure 50: TD-DFT-simulated UV–Vis spectrum of $[Mo_2S_4(MeOH)_8]^{6+}$ and corresponding vertical electronic transitions. The spectrum was generated by Gaussian broadening of the TD-DFT stick spectrum using oscillator-strength-weighted Gaussians (σ = 20 nm).

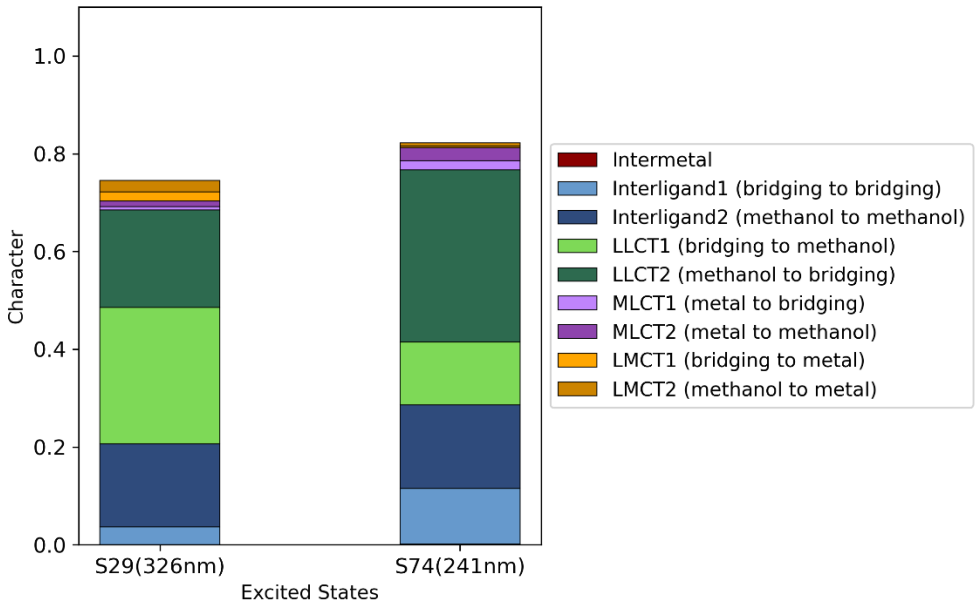

Figure 51: Decomposition of the most relevant excited states of $[Mo_2S_4(MeOH)_8]^{6+}$. The excited-state wave functions were decomposed into metal-centered, ligand-centered, and charge-transfer (LLCT, MLCT, LMCT) contributions using TheoDORE based on a chemically motivated fragmentation scheme. Bars indicate the relative weights of the individual excitation categories.

Table 20: Electronic character of selected singlet excited states of $[Mo_2S_4(MeOH)_8]^{6+}$. Charge-density difference plots were generated for individual TD-DFT excitations, with each image depicting one excited state. Electron density depletion and accumulation upon excitation are shown in purple and red, respectively.

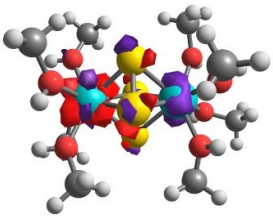	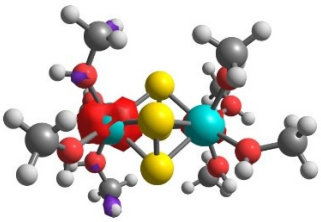
S_{29}, Interligand Transfer	S_{74}, Interligand Transfer

3.3 Light-driven hydrogen evolution reactivity of molecular thio-oxo-molybdate catalysts

The results presented in this chapter are based on an accepted manuscript under the Creative Commons Attribution 4.0 International License (CC BY 4.0). The accepted manuscript was published as "*Light-driven hydrogen evolution reactivity of molecular thio-oxo-molybdate catalysts*", Luca T. Schleicher[‡], S. Henriette Kolbinger[‡], Akuila Edwards, Kristin Sellmann, Luis Senz, Stephan Kupfer, Michale Schmitt,* Jürgen Popp, and Carsten Streb,* *Sustainable Energy Fuels*, **2026**, DOI: 10.1039/D6SE00061D. The numbering of tables, figures, equations and references was adapted for inclusion in this thesis. No other adaptations were made. The contributions of the co-authors are acknowledged after the abstract. The supporting information to the manuscript can be found directly after the manuscript's conclusion.

Abstract

Heterogeneous molybdenum sulfides are widely used noble metal-free hydrogen evolution reaction (HER) catalysts. Thiomolybdates, their molecular analogues have been developed as viable minimal models to study reactivity at the molecular level. Here, we explore the light-driven HER reactivity and stability of the mixed thio-oxo-molybdate prototype $[Mo_2O_2S_6]^{2-}$ in homogeneous solution. In combination with the photosensitizer $[Ru(bpy)_3]^{2+}$, $[Mo_2O_2S_6]^{2-}$ shows promising HER performance (turnover number TON > 500), as well as strong reactivity dependence on the reaction conditions. Mechanistic experimental studies combined with density functional theory computations reveal complex speciation of the catalyst in solution, as well as light-induced and light-independent reaction pathways for catalyst and photosensitizer which are in line with disulfide-for-solvent ligand exchange reactions. These structure–reactivity insights outline design rules for more robust, solvent-tolerant thiomolybdate HER catalysts.

Authors contribution

L. T. Schleicher[‡]	Conceptualization, methodology, investigation, formal analysis, data processing, synthesis, writing original draft, visualization, discussion and revision
S. H. Kolbinger[‡]	Conceptualization, methodology, investigation, formal analysis, data processing, writing original draft, visualization, discussion and revision
A. Edwards	Methodology, investigation, formal analysis of Raman measurements
K. Sellmann	Methodology, investigation, formal analysis, writing original manuscript
L. Senz	Resources, validation
S. Kupfer	Conceptualization, supervision, funding acquisition, writing original draft, discussion and revision
M. Schmitt*	Conceptualization, supervision, funding acquisition, writing original draft, discussion and revision
J. Popp	Supervision, funding acquisition, writing original draft
C. Streb*	Conceptualization, supervision, funding acquisition, writing original draft, discussion and revision

‡ Authors contributed equally to this work.

* Corresponding author

Motivation & Introduction

The development of sustainable catalysts for green hydrogen production is a major global research goal. Molybdenum sulfides have emerged as promising candidates for the hydrogen evolution reaction (HER), since they are earth-abundant and noble-metal-free.[116, 149,150,187,188] Molecular molybdenum sulfides, so-called thiomolybdates are ideal

models to rationalize HER reactivity and have been investigated as homogeneous and heterogenized catalysts for photochemical and electrochemical HER.[127, 148, 159,189–191] The prototype thiomolybdate cluster $[Mo_3S_{13}]^{2-}$ (Figure 52) is the most studied system to-date. When operated in homogeneous MeOH:H_2O solution in combination with $[Ru(bpy)_3]^{2+}$ as photosensitizer (**PS**) and ascorbic acid as electron/proton donor, TONs >20 000 have been achieved after 6 h of visible light-irradiation.[148] Note that the catalytic performance depends strongly on the reaction conditions including solvent, reagent concentrations and sample preparation. Concerning solvent dependent performance, a mixture of methanol and water (10:1, v:v) was found to be optimal in terms of TON and TOF.[148]

Experimental and theoretical mechanistic studies revealed that under reaction conditions (in a MeOH:H_2O mixture (1:1, v:v)), $[Mo_3S_{13}]^{2-}$ undergoes substitution of terminal disulfide ligands for solvent ligands L (L = MeOH, H_2O) on a timescale of less than one hour.[148] These studies also showed that partially ligand-exchanged species featured higher HER-catalytic activity than the native catalyst, while full exchange of all three terminal disulfide ligands leads to a species with low HER-activity.[148] More recent studies suggest that ligand exchange is accelerated upon irradiation with visible light.[182]

These dynamic effects and complex (light-induced) speciation equilibria make mechanistic studies challenging. Similar observations on solvent-dependent HER-activity were made for the thiomolybdate $[Mo_2S_{12}]^{2-}$ (Figure 52): highest HER-activity was observed in pure methanol, and when combined with the PS $[Ru(bpy)_3]^{2+}$ and ascorbic acid as electron/proton donor, TONs >1500 were observed.[127] Here, Raman spectroscopy revealed that ligand exchange occurs on a much slower timescale (>12 h) compared with $[Mo_3S_{13}]^{2-}$ indicating that cluster structure significantly affects ligand-exchange and HER reactivity.[127]

Inspired by these studies, we hypothesized that structure modification on the Mo_2-framework could have significant impact on HER activity. To this end, this study reports the first experimental and theoretical insights into the homogeneous, light-driven HER reactivity of thio-oxo-molybdates. Thio-oxo-molybdates are structurally related to thiomolybdates and have so far received little attention, despite their potential as noble metal-free HER catalysts where reactivity can be tuned by modification of the oxo-to-(di)sulfide ligand environment.[110,181]

Keita et al. reported that a mixed thio-oxo-molybdates based on $[Mo_2O_2S_2]^{2+}$ building blocks can be used as efficient electrocatalysts for the HER.[192] In an exemplary study, Miras and co-workers showed that the thio-oxo-molybdate $[Mo_2O_2S_6]^{2-}$ (Figure 1) features significant electrocatalytic HER activity.[152] Briefly, $[Mo_2O_2S_6]^{2-}$ is composed of two Mo(V) centers are linked by two bridging sulfides (μ-S^{2-}). Each metal center is additionally coordinated by one terminal disulfide ligand (η^2-S_2^{2-}) and one terminal oxo ligand. In contrast, the pure thiomolybdate $[Mo_2S_{12}]^{2-}$ is based on two Mo(V) linked by two bridging disulfide ligands (μ-S_2^{2-}). Each Mo also features two terminal disulfide ligands (Figure 52). To-date, there is virtually no information on the behavior of thio-oxo-molybdates such as $[Mo_2O_2S_6]^{2-}$ under light-driven homogeneous HER catalytic conditions.

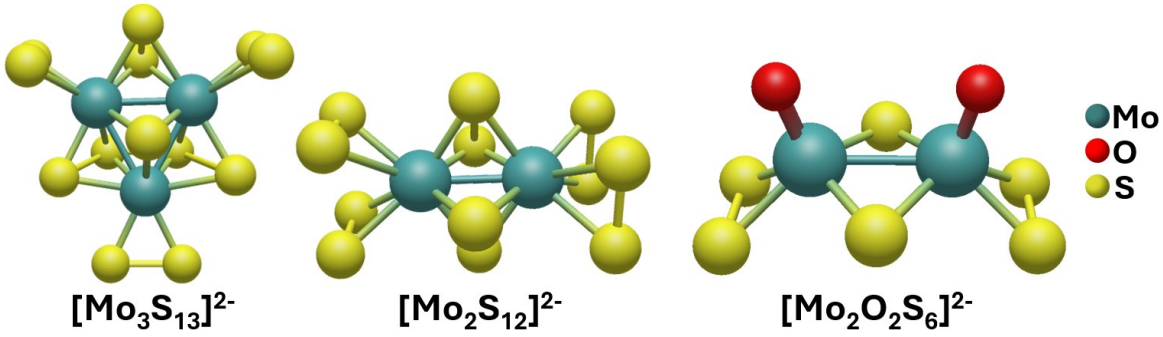

Figure 52: Ball-and-stick representations of the molecular structure of the thiomolybdates $[Mo_3S_{13}]^{2-}$ (left), $[Mo_2S_{12}]^{2-}$ (center) and the thio-oxo-molybdate $[Mo_2O_2S_6]^{2-}$.

Previous investigations have used DFT calculations to study the HER energetics for $[Mo_3S_{13}]^{2-}$, $[Mo_2S_{12}]^{2-}$ and $[Mo_2O_2S_6]^{2-}$.[148, 152,193] These studies suggested a Volmer–Heyrovsky-type mechanism as energetically most favourable for all three catalysts. In the case of $[Mo_3S_{13}]^{2-}$ and $[Mo_2S_{12}]^{2-}$, calculations have shown the sulfur-centered mechanism, involving one of the bridging disulfide ligands as active site to be energetically favoured.[148,193] However, in $[Mo_2O_2S_6]^{2-}$, where no bridging disulfide is present, the active site is assumed to be a terminal disulfide ligand which presumably undergoes a proton-coupled reductive (reversible) cleavage of the S–S bond, resulting in the formation of a protonated sulfide as reactive intermediate.[152] In sum, research on thio(oxo)molybdate has demonstrated that changes to the ligand environment of these species have major effects on stability and HER-reactivity.

The present study takes inspiration from these studies and aims to address knowledge gaps regarding the light-driven homogeneous HER activity of the thio-oxo-molybdate

$[Mo_2O_2S_6]^{2-}$. Based on catalytic studies, *in-situ* Raman spectroscopy and quantum chemical calculations at the density functional level of theory (DFT), we provide understanding into HER activity, plausible reaction pathways and the impact of ligand exchange on this cluster prototype, thereby guiding future catalyst development efforts.

Results and discussion

Initially, we explored the homogeneous HER activity of $[Mo_2O_2S_6]^{2-}$ when used with $[Ru(bpy)_3]^{2+}$ as photosensitizer (PS) and ascorbic acid/ascorbate as sacrificial electron donor (SED) in homogeneous MeOH:H_2O mixtures, inspired by earlier studies on thiomolybdates.[127,148] Briefly, the thio-oxo-molybdate $(NMe_4)_2[Mo_2O_2S_6]$ was synthesized based on a reported method, for details see SI.[172]

The standard reaction setup contained $(NMe_4)_2[Mo_2O_2S_6]$ (0.5 µM), the PS, i.e., $[Ru(bpy)_3](PF_6)_2$ (20 µM) and the sacrificial electron donor ascorbic acid / sodium ascorbate (buffered, aqueous solution, total concentration 10 mM, pH 4) First, we determined the solvent conditions under which $[Mo_2O_2S_6]^{2-}$ exhibits optimum light-driven HER performance. To this end, four different solvent ratios were tested: pure methanol, pure water and two MeOH:H_2O mixtures (9:1 and 1:1, v:v). These conditions are similar to those used in experiments performed for thiomolybdates.[127,148] All samples were irradiated for 300 min in a custom-built modular photoreactor[144] using LED irradiation (λ_{max} = 465 nm, P = 13 mW cm^{-2}, q = 51 nmol cm^{-2} s^{-1}). Hydrogen evolution was determined by using gas chromatography. Each experiment was carried out in triplicate, and the average turnover number and standard deviation were determined (see Figure 53). Blank reference experiments performed in the absence of the catalyst showed only low levels of hydrogen evolution (see ESI, Table 22).

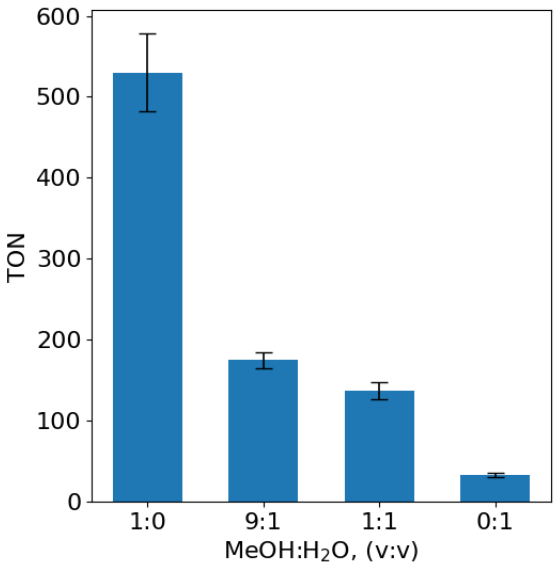

Figure 53: TON of the $[Mo_2O_2S_6]^{2-}$ system in MeOH:H_2O solvent mixtures. Catalytic conditions: c($[Mo_2O_2S_6]^{2-}$) = 0.5 µM, c(PS) = 20 µM, c(SED) = 10 mM, pH 4.

Figure 53 illustrates the TONs obtained after 300 min irradiation. The data show that highest HER performance is observed in pure methanol (TON *ca.* 530). For comparison: reference experiments using $[Mo_3S_{13}]^{2-}$ as catalyst under similar conditions gave a TON of 670.[194] Increasing the water content leads to a continuous TON decrease, with the lowest activity observed in pure water (TON ≈ 33). This behavior is similar to the solvent-dependent HER performance of $[Mo_2S_{12}]^{2-}$.[127] One hypothesis to explain this behavior is the rapid degradation of the photosensitizer in aqueous solutions. In the 1:1 mixture and pure water, discoloration of the solution was observed upon irradiation, which might also be a reason for the lower catalytic activity of the system. The formation of $[Ru(bpy)_2(H_2O)_2]^{2+}$ in aqueous solutions has been previously reported in the literature.[195] PS degradation was further studied by monitoring changes of the characteristic PS MLCT absorption band (452 nm) using time-lapse UV-Vis spectroscopy. Here, we studied the impact of different solvent mixtures as well as presence/absence of catalyst on PS degradation (ESI, see Figure 66). Analysis of these data shows that PS degradation kinetics are not affected by the catalyst, and the rate of PS bleaching is dominantly controlled by the solvent composition. Higher water concentrations significantly increase PS degradation.

To determine whether ligand exchange processes occur for $[Mo_2O_2S_6]^{2-}$, time-resolved Raman spectroscopy was performed. Raman spectroscopy offers high molecular selectivity and can be applied *in situ* under catalytic conditions; however, the intrinsically low Raman scattering cross-section necessitates comparatively high analyte concentrations for sufficient signal-to-noise ratios. Accordingly, due to the low catalyst concentrations used in the light-driven HER experiments, Raman measurements were performed at elevated catalyst concentrations (2.5 mM). The Raman spectrum of $[Mo_2O_2S_6]^{2-}$ exhibits two characteristic vibrational bands, which were identified using DFT frequency calculations (see ESI). The band at 530 cm^{-1} corresponds to vibrations of the bridging sulfide ligands, while the band at 560 cm^{-1} is assigned to the terminal disulfide ligands. Raman experiments were conducted in pure methanol, pure water and MeOH:H_2O (1:1, v:v). Representative Raman spectra recorded for the catalyst in pure methanol are shown in Figure 54. The Raman data for the other solvent conditions are shown in the SI.

Monitoring the two characteristic Raman signals of $[Mo_2O_2S_6]^{2-}$ over a period of five hours revealed that the intensity of the 530 cm^{-1} band remains relatively stable, whereas the 560 cm^{-1} band shows a steady decrease in intensity. This trend indicates that under the given reaction conditions, the terminal disulfide ligands undergo exchange for solvent molecules. Also, comparison of the different solvent conditions revealed that the decay rates are of the same order of magnitude ($\approx 10^{-2}$ min^{-1}), suggesting that ligand exchange is not strongly solvent-dependent and occurs at similar rates in methanol and water. It cannot be excluded that under catalytic conditions at lower optical densities and with active photosensitizer present, photochemical processes may contribute differently.

To further corroborate these findings, and to study the impact of irradiation on the proposed MeOH for disulfide ligand exchange, we performed time-lapse UV-Vis-spectroscopy. Here, we studied solutions of the catalyst in pure MeOH or MeOH:H_2O (1:1, v:v) for periods of 300 min under continuous LED irradiation at 465 nm. For both solvent conditions, we observe nearly identical spectral changes of the characteristic catalyst signals under irradiation, while the non-irradiated samples show no significant spectral changes (Figure 54b, and ESI, Figure 67-69). In detail, for the measurements in methanol (Figure 54b), we observe the loss of several characteristic peaks (270 nm, 375 nm, 470

nm), while two new signals (385 nm, 440 nm) emerge after 30 min of irradiation. Upon prolonged irradiation, these two signals continuously decrease and disappear after 300 min irradiation. This observation is in line with a two step-process, where first, the native catalyst is converted into an intermediate species which then undergoes a second conversion step. Note that for MeOH:H_2O (1:1, v:v) mixtures, we observe virtually identical UV-Vis signal changes, indicating a similar mechanism (ESI, Figure S9). In sum, Raman spectroscopy and UV-Vis-spectroscopy both indicate significant structural changes of $[Mo_2O_2S_6]^{2-}$ in solution. While Raman data indicate the replacement of terminal disulfide ligands on a 0 – 60 min timescale, UV-Vis spectroscopy indicates two processes on a 0 – 180 min timescale, resulting in changes of the electronic structure of the catalyst. This complex behaviour is in line with previous reports on thiomolybdate ligand exchange under irradiation. [148,182]

To further study the electrochemical behaviour of $[Mo_2O_2S_6]^{2-}$, we used cyclic voltammetry analyses. Measurements were performed in acetonitrile containing molar ratios of $[Mo_2O_2S_6]^{2-}$: MeOH ranging from 0 to 20 (see SI). As a general trend, we observe that increasing MeOH concentrations lead to changes of the CV signals of the catalyst: for the one-electron reduction process at -1.1 V, we observe a minor cathodic shift (< 50 mV) upon methanol addition, which might be indicative of structural changes of the catalyst, or changes induced by the changing solvent compositions. Note that this reduction potential indicates that both oxidative quenching (E = -1.23 V) as well as reductive quenching (E = -1.72 V) of the catalyst by the photosensitizer is in principle feasible.[196] Also, we note the observation of an irreversible oxidation peak at approximately +1.1 V, which is assigned to oxidation of the cluster-bound disulfide ligands,[197] indicating that oxidative decomposition of the cluster occurs under these conditions.

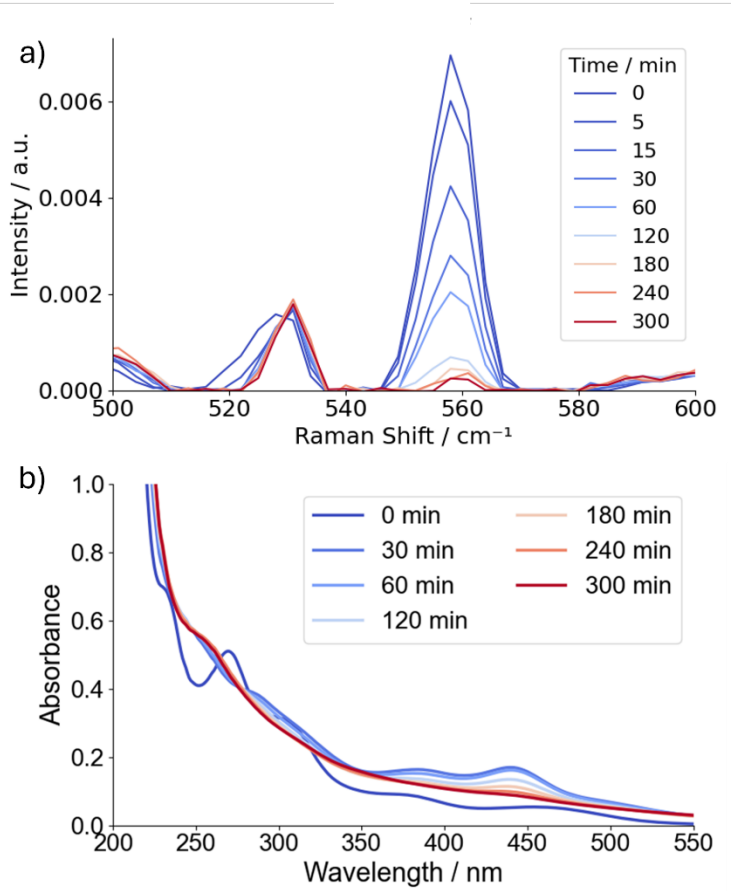

Figure 54: Time-dependent Raman spectra of $[Mo_2O_2S_6]^{2-}$ in MeOH (c = 2.5 mM). b) Time-dependent UV-Vis spectra of $[Mo_2O_2S_6]^{2-}$ (c = 50 µM) in MeOH.

Next, we analyzed the time-dependent turnover frequency (TOF) of HER catalysis to gain further understanding of the proposed structural changes and ligand exchange proposed for $[Mo_2O_2S_6]^{2-}$. Specifically, we studied the standard reaction systems using MeOH or MeOH:H_2O (1:1) as solvents and monitored the hydrogen evolution over five hours using the standard catalytic system described in Figure 53.

The resulting TOF profiles are shown Figure 55. The TOF data reveal two major trends. First, the overall catalytic activity is higher in pure methanol, consistent with the solvent-dependence observed for the TON (Figure 53). Second, the TOF time-dependency differs between the two solvent systems: in the MeOH:H_2O mixture, the TOF shows a modest increase during the initial phase of the reaction, followed by a steady decrease at longer reaction times. This behavior is consistent with the stepwise formation of a catalytically more active species, followed by a second, subsequent deactivation. This is also in line with similar stepwise deactivation processes reported previously for $[Mo_3S_{13}]^{2-}$.[148] In

contrast, in pure methanol, the maximum TOF is already reached at the earliest recorded data point (30 minutes), followed by continuous decrease of TOF. Note that due to experimental procedures, there is a delay of approximately 60 min between catalyst dissolution and the start of irradiation. This period provides sufficient time for initial ligand exchange before catalysis is initiated. Consequently, it cannot be excluded that a ligand-exchanged species, rather than the pristine $[Mo_2O_2S_6]^{2-}$ cluster, represents the catalytically active form present at the first data points under the given conditions. Also note that catalytic and Raman data can only qualitatively be compared since the systems were operated at different catalyst concentrations as described in the Raman section above.

Also, differences in the observed kinetic behavior between pure methanol and the MeOH:H_2O mixture may also reflect differences in the equilibration dynamics of ligand exchange: in mixed solvents, the presence of multiple equilibria could lead to slower establishment of a catalytically relevant species. Furthermore, the dynamics of other mechanistic steps which may be solvent-dependent such as PS quenching by the electron donor, need to be taken into account, as these steps are also affected by the reaction conditions.[197,198] Nevertheless, overall, the kinetic observations support the notion that ligand substitution leads to the generation of distinct catalytic species with different reactivity profiles. However, the data also show that in future work, more detailed, time-resolved *operando* studies are required to gain further molecular-level insights into this complex reaction system.

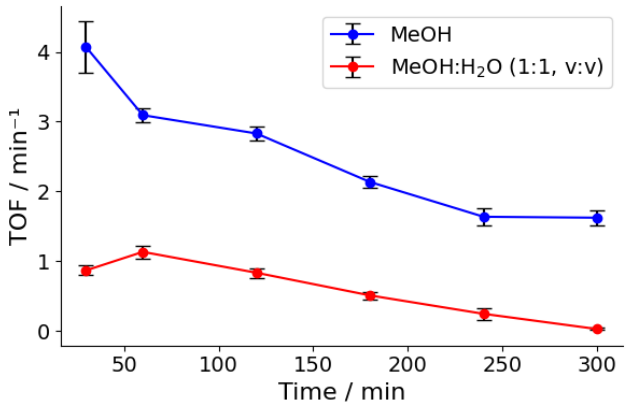

Figure 55: TOF for the light-driven hydrogen evolution by $[Mo_2O_2S_6]^{2-}$ during 300 min irradiation in pure methanol as well as in MeOH:H_2O 1:1, v:v.

To provide further evidence for the underlying causes of structural changes to the catalytic system, we performed reference experiments which were kept under light or dark conditions: we studied three catalytic systems: (I), a freshly prepared catalyst stock solution ($[Mo_2O_2S_6]^{2-}$ (c = 0.5 mM) in MeOH) which was used immediately; (II) the same catalyst stock solution which was stored under inert conditions for 90 min under dark conditions: (III) the same catalyst stock solution which was stored under inert conditions while being irradiated with a 465 nm LED for 90 min. As shown in Figure 56, we observe that for the irradiated solution, we observe significantly higher TONs compared to the two reference systems. These data further support our hypothesis that light-irradiation initiates structural changes to the catalyst which result in the (initial) formation of a more active HER catalyst species.[195] The findings are also in line with previous studies which reported similar activation/deactivation cascades for thiomolybdate HER catalysts.[148,152]

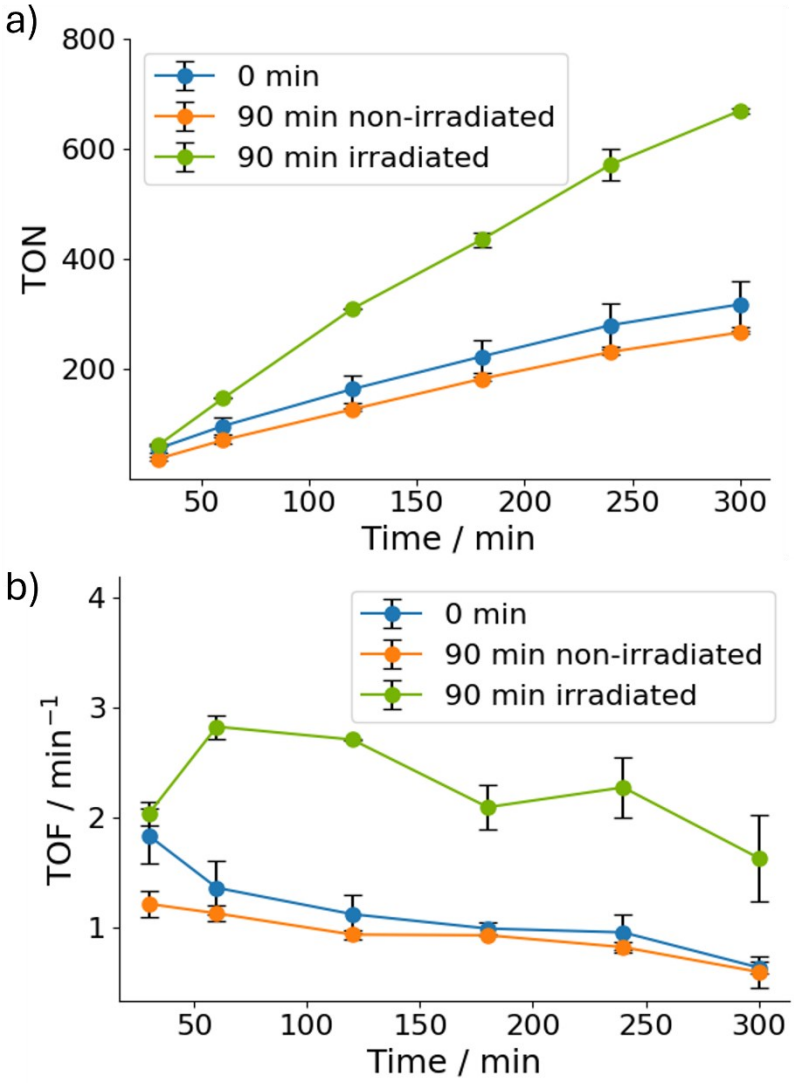

Figure 56: a) Time-dependent TON and b) TOF for the photocatalytic system (c($[Mo_2O_2S_6]^{2-}$) = 0.5 µM, c(PS) = 20 µM, c(SED) = 10 mM, pH 4 in MeOH) for three different catalyst stock solutions: blue = freshly dissolved stock solution, orange = stock solution was left under non-irradiated conditions for 90 min, green = stock solution was irradiated for 90 min (λ = 465 nm).

Quantum chemical analysis of catalytic activity

To rationalize the experimental observations and the apparent role of ligand substitution in catalytic activation, computational analysis of the catalytic activity was performed. Similar to investigations concerning $[Mo_3S_{13}]^{2-}$, DFT calculations (details see ESI) aimed to assess the thermodynamics of the various intermediates on the HER activity of $[Mo_2O_2S_6]^{2-}$.[148] Based on prior studies, the HER active sites are assumed to be the terminal disulfide ligands in $[Mo_2O_2S_6]^{2-}$.[152,188] Although a variety of different processes appear feasible during HER catalysis, the following key mechanisms involving the terminal

disulfide ligands are primarily considered in the present study: proton-coupled electron transfer (PCET), electron transfer/reduction (ET), proton transfer (PT), and finally hydrogen release. Hydrogen release is evaluated based on the difference in Gibbs free energy between two adsorbed hydrogen atoms (H^0) and a hydrogen molecule (H_2). In line with Sabatier's principle, the most plausible reaction pathways are expected to involve predominantly exergonic steps, moderate energy differences, and PCET steps with ΔG values near 0 kcal/mol (see Figure 57).[199]

Based on the data presented in Figure 57a, thermodynamically plausible reaction pathways can be identified under the previously outlined assumptions. The sequence is expected to begin with a slightly endergonic PCET step (ΔG = +2.0 kcal/mol), forming $H_1[Mo_2O_2S_6]^{2-}$. In contrast, the competing one-electron reduction pathway was calculated to be significantly more endergonic (ΔG = +26.1 kcal/mol) and is therefore thermodynamically disfavored under the applied conditions. The intermediate, $H_1[Mo_2O_2S_6]^{2-}$, is then reduced via an exergonic electron transfer (ΔG = −7.6 kcal/mol) followed by a strongly exergonic PT (ΔG = −26.2 kcal/mol). The resulting species, $H_2[Mo_2O_2S_6]^{2-}$, subsequently undergoes endergonic hydrogen release (ΔG = +3.6 kcal/mol). This proposed mechanism, which includes a PCET step, is in reasonable agreement with recent findings in literature.[152] However, it is important to emphasize that the pathway involves a slightly endergonic PCET step, substantial energy differences, and an endergonic hydrogen release step, deviating from the features outlined for an ideal HER process. Notably, the performed quantum chemical calculations merely account for implicit solvent-solvate interactions. Thus, energy of the final product $[Mo_2O_2S_6]^{2-}$ species is likely overestimated.

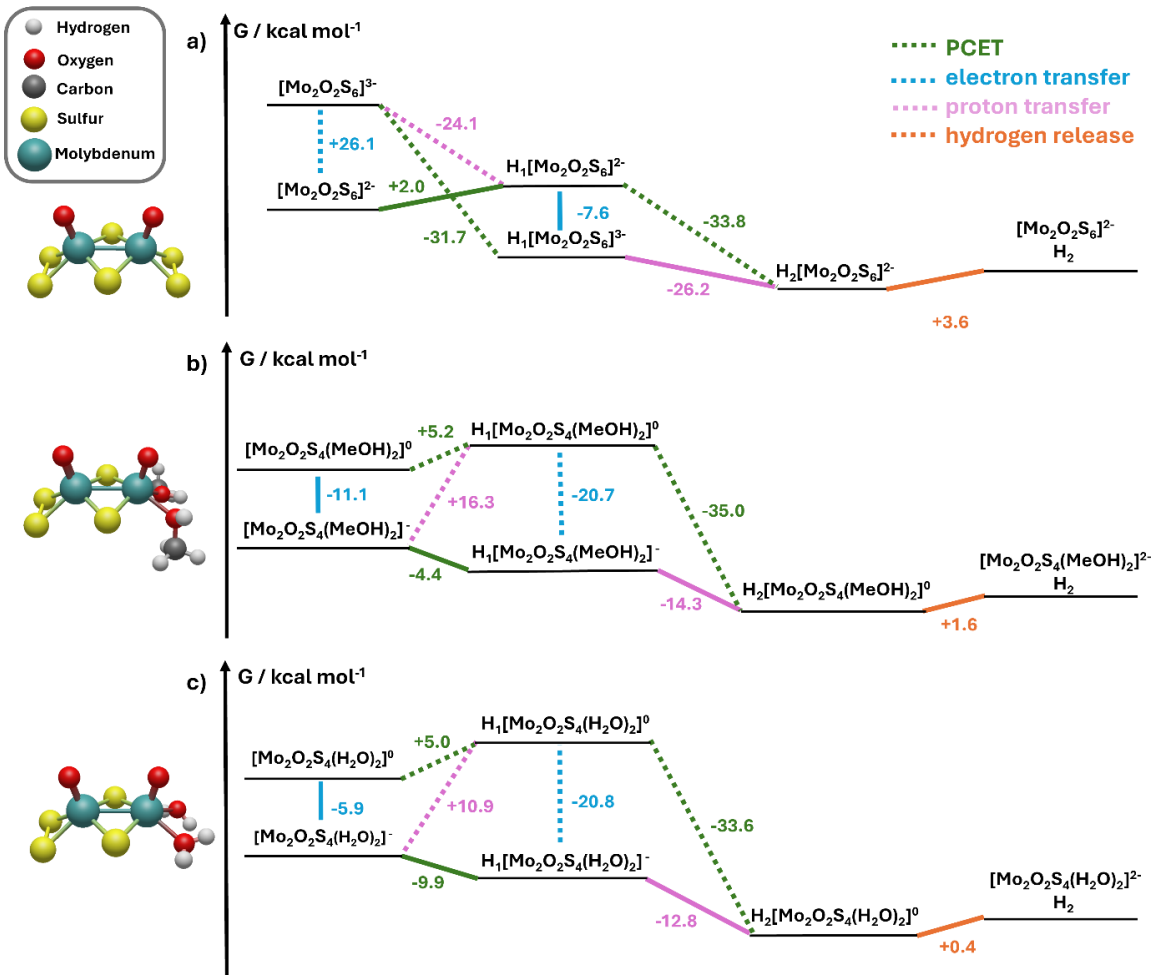

Figure 57: Calculated Gibbs free energies (G) for structures involved in the HER process in methanol: a) $[Mo_2O_2S_6]^{2-}$, b) $[Mo_2O_2S_4(MeOH)_2]^0$, c) $[Mo_2O_2S_4(H_2O)_2]^0$. Solid lines represent the favoured pathways, while dashed lines represent alternative, less favoured pathways. All calculations were performed under consideration of the underlying catalytic system (see ESI).

Two ligand exchange products which were considered in this study involve aquo or methanol ligands replacing one of the original terminal disulfide ligands, see Figure 57b and c. The products of two ligand exchange processes with either solvent are considered to possess no HER active sites. Based on the criteria for identifying favorable reaction pathways, both ligand exchange products show similar sequences. In contrast to the parent catalyst (Figure 57a), both reaction pathways are expected to begin with an exergonic electron transfer (b: ΔG = −11.1 kcal/mol; c: ΔG = −5.9 kcal/mol), as the rivaling reaction pathway is an endergonic PCET (b: ΔG = +5.2 kcal/mol; c: ΔG = +5.0 kcal/mol. This reduction is then followed by an exergonic PCET step (b: ΔG = −4.4 kcal/mol; c: ΔG = −9.9 kcal/mol), and an exergonic PT (b: ΔG = −14.3 kcal/mol; c: ΔG = −12.8 kcal/mol). In both cases, the final step is a slightly endergonic hydrogen release (b: ΔG = +1.6 kcal/mol;

c: ΔG = +0.4 kcal/mol). However, the product species is likely stabilized by explicit solvent effects, i.e., hydrogen bonds, which were not accounted for by the current computational approach.

A direct comparison with the unmodified catalyst, $[Mo_2O_2S_6]^{2-}$, reveals notable differences. First, the pathways for the ligand-exchanged species (Figure 57b, c) follow a different overall mechanism than that of the parent compound (Figure 57a), and they exhibit smaller energy differences between steps. Additionally, the HER pathways of $[Mo_2O_2S_4(MeOH)_2]$ and $[Mo_2O_2S_4(H_2O)_2]$ involve only one slightly endergonic step, being hydrogen release, whereas the pathway for $[Mo_2O_2S_6]^{2-}$ includes two endergonic steps, with the hydrogen release posing a significantly higher energy barrier. In this context, the ligand-exchanged species is proposed to undergo an initial reduction step prior to PCET, whereas the unmodified $[Mo_2O_2S_6]^{2-}$ catalyst is expected to initiate the process via PCET. This behavior is consistent with their respective charge states as the neutral ligand-exchanged species is more prone to reduction than the doubly negatively charged parent complex. Although the precise contribution of each individual step as well as their exact influence on overall hydrogen evolution remains difficult to quantify, these findings suggest improved catalytic properties upon ligand exchange with methanol or water. Moreover, these findings highlight the dynamic structural and electronic transformations occurring under catalytic conditions in both solvents. Notably, this trend parallels previously reported observations for $[Mo_3S_{13}]^{2-}$.

Conclusion

Raman spectroscopy, quantum chemical simulations, UV-Vis spectroscopy and gas chromatography were combined to elucidate key processes occurring during catalytic hydrogen evolution using $[Mo_2O_2S_6]^{2-}$. In particular, light-induced ligand exchange processes were proposed to play a crucial role in the activation of the catalytic cycle. The collected data allowed the development of a proposed overall mechanistic pathway and the connection to HER activity, as illustrated in Figure 58.

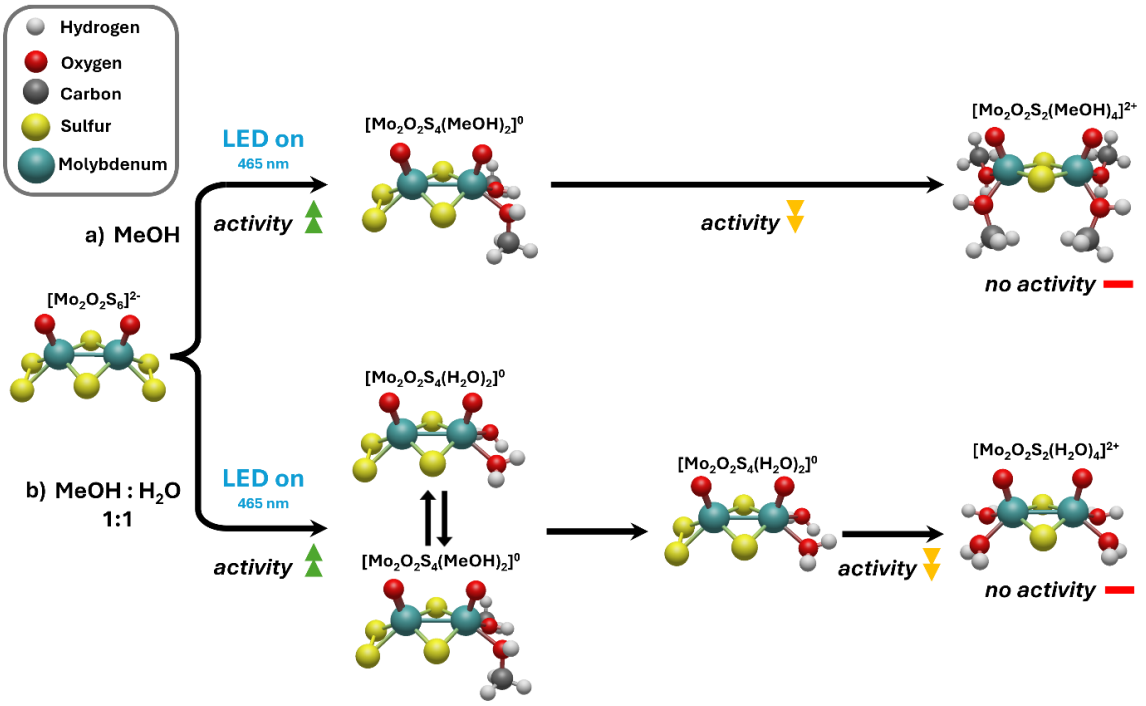

Figure 58: Schematic illustration of the proposed ligand exchange processes of $[Mo_2O_2S_6]^{2-}$ and the respective influences on the catalyst's HER activity in a) methanol and b) 1:1 methanol–water (v:v), involving the influence of the irradiation via LED.

Based on the findings of the catalytic activity measurements, it is evident that HER catalysis is significantly more efficient in pure methanol compared to aqueous environments.

Raman spectroscopic monitoring of the catalyst solutions suggests that for $[Mo_2O_2S_6]^{2-}$, an initial ligand exchange, where one disulfide ligand is replaced by two methanol or water ligands, occurs rapidly. UV-Vis spectroscopic investigation shows that this ligand-exchange is however mainly light-induced. Both computational and experimental findings indicate that the resulting partially substituted species is more catalytically active than the original complex. This finding supports the proposal of distinct mechanistic pathways for catalysis in methanol (Figure 58a) and in aqueous solution (Figure 58b).

Supplementary Information

Instrumentation

Attenuated total reflectance-Fourier-transformed infrared spectroscopy (ATR-FT-IR) were performed using a Bruker Alpha II equipped with an ATR Platinum Diamond unit. The data were recorded with 24 scans at a resolution of 4 cm^{-1}. All spectra were background-corrected within the Bruker OPUS 8.1 program suite.

UV/Vis/NIR spectroscopy was performed on a Cary 3500 UV/Vis/NIR spectrophotometer equipped with a Xenon flash lamp (250 Hz). Measurements were performed in screw cap quartz glass cuvettes (d = 10.0 mm) with rubber septa.

Gas chromatography was performed on a Shimadzu Nexis GC-2030 equipped with a BID detector and a split injection unit with a split ratio of 1:20. Helium was chosen as the carrier gas. The column was heated to a constant temperature of 80℃.

Chemicals: All chemical reagents were obtained commercially and used as received unless stated otherwise. $(NMe_4)_2[Mo_2O_2S_6]$ was prepared according to the literature.[172]

Raman: was performed using a NIR – excited fiber coupled Raman setup (RXN I, Kaiser Optical Systems, Ann Arbor, MI, USA). Samples were excited through a fiberoptic probe (InPhotonics, Norwood, MA, USA) which is equipped with band and long pass filters for cleanup and Rayleigh-rejection (cutoff long pass: ca.250cm^{-1}) coupled to a 785nm single-frequency laser diode (Xtra II, Topica Photonics, Munich, Germany). This system disperses the scattered Raman light passing through a holographic grating which is detected via a multi-row, thermoelectrically cooled (TOP = -60°C) CCD (Andor, Belfast, UK) resulting in spectral resolution around 4 cm^{-1}. The system was white light calibrated using a white light source prior to the measurements and data was collected from 250-3500cm^{-1}.

Vials: glass vials for catalytic measurements were purchased from Biotage with crimp caps made of aluminium with silicon rubber/Teflon septa. Outer diameter: 17 mm, inner diameter: 15 mm, length: 85 mm, volume: ~11.0 mL

Cyclovoltammetry: were carried out in an argon filled glove box using a CH Instruments potentiostat CHI 760 E with a scan rate of 100 mV s^{-1} using a glassy carbon working

electrode, a Pt wire counter electrode, and a non-aqueous $Ag/AgNO_3$ reference electrode in MeCN.

Experimental data

Synthesis of $(NH_4)_2[Mo_2S_{12}]$

The synthesis of $(NH_4)_2[Mo_2S_{12}]$ is based on a procedure by MÜLLER et al.[172]

$(NH_4)_6[Mo_7O_{24}]\times 4H_2O$ (2.18 g, 1.78 mmol) was dissolved in 20 ml of deionized water and $NH_2OH\times HCl$ (1.55 g, 22 mmol) was dissolved in 15 ml of water. Both solutions were combined, which formed a yellow solution to which 20 ml of ammonium polysulfide (22 wt% aq) were added. The mixture was stirred at 50 °C for one hour. During heating the yellow mixture gained a dark red color. After cooling the reaction mixture to room temperature, the solution was filtered and transferred to a Schlenk-flask and heated to 90 °C for five hours under nitrogen. After cooling the dark brown solution was stirred overnight under nitrogen during which a black precipitate was formed. The solid was filtered and washed with 20 ml ice-cold water and 60 ml isopropanol. In order to remove the excess sulfur, the product was washed with 20 ml of carbon disulfide solution and 40 ml of diethyl ether.

Yield: 1.04 g (1.60 mmol, 26% based on Mo-atoms)

UV-Vis bands (nm in MeOH): λ_{max} = 270 nm

$\lambda_{shoulder}$ = 380 nm

ATR-FTIR bands (cm^{-1}): 520 (s), 1370(s)

Synthesis of $(NMe_4)_2[Mo_2O_2S_6]$

The compound $[Mo_2O_2S_6]^{2-}$ was synthesized according to the method reported by MÜLLER et al. involving slight modifications.[172] $(NH_4)_2[Mo_2S_{12}]$ (2.10 g, 3.24 mmol) was dissolved in 250 ml of 25% ammonia-solution and stirred for 17 hours during which time the solution changed from yellow to orange in color. After stirring, $C_4H_{12}NCl$ (4.60 g, 41.97 mmol) were added to the solution and left at room temperature without stirring. After two hours the solution was filtered and an orange crystalline solid was isolated. The solid was then washed with 20 ml of ice-cold water, 60 ml of isopropanol and 60 ml of diethyl ether.

Yield:	0.67 g (1,18 mmol, 74%)	
UV-Vis bands (nm in MeOH):	λ_{max} =	250 nm, 270 nm, 455 nm
	$\lambda_{shoulder}$ =	310 nm, 395 nm
ATR-FTIR bands (cm-1):	463 (s), 512 (s), 926 (s), 1278 (s), 1477 (s)	

Catalyst sample preparation

HER Catalysis: For each component a stock-solution with set concentrations was prepared: the catalyst $(NMe_4)_2[Mo_2O_2S_6]$ (c = $5 \cdot 10^{-4}$ M), the photosensitizer $[Ru(bpy)_3](PF_6)_2$ (c = $1 \cdot 10^{-5}$ M), and the sacrificial electron donor (SED) (sodium ascorbate and ascorbic acid, molar ratio: 4:5 ; c = $1 \cdot 10^{-1}$ M in water, c= $1.25 \cdot 10^{-2}$ M in methanol when the whole system was measured in pure methanol). The stock solutions were prepared in either methanol or water, depending on the solvent ratio used. Before preparation of the catalytic reaction mixture, the catalyst stock solution was diluted with methanol or water respectively by a factor of 100. The diluted catalyst solution, along with the respective stock solutions of the PS and SED and the appropriate solvents, were combined in crimp vials resulting in a total solution volume of 4 mL per vial. The resulting concentrations of the compounds were: c(CAT) = 0.5 µM, c(PS) = 20 µM, c(SED) = 10 mM. The vials were sealed using aluminum crimp caps with silicone septa and purged with nitrogen for fifty minutes. To prevent leakage, the septa were sealed with clear nail polish.

Raman Measurements: The samples for the Raman measurements were prepared by dissolving the catalyst (2.5 mM) in 2.5 mL of the respective methanol/water mixture in a 4 ml quartz cuvette. The resulting solution was purged with argon for approximately 15 minutes before being transferred to the spectrometer for analysis.

UV/Vis Measurements:

The samples for the UV/Vis measurements were prepared by dissolving the catalyst in 2,5 mL of the respective methanol/water mixture (50 µM) within a 4 ml quartz cuvette. The resulting solution was purged with N_2-gas for approximately 15 minutes before being transferred to the spectrometer for analysis or to the photoreactor for irradiation.

Catalytic procedures

HER Catalysis: The respective samples were placed in a custom-designed photoreactor,[144] and irradiated using a LED (465 nm, 13 mW incident power at bottom of the sample vial). Each solvent mixture was prepared twice per day. The order of measurements was chosen randomly, and every experiment for each solvent mixture was repeated at least six times to ensure reproducibility and allow statistic error determination. Before starting the GC measurements, at least two air measurements were conducted to verify a stable baseline. Sample collection was carried out using a Model 710 RN syringe from Hamilton. The nail polish covering the septum was removed using a spatula before inserting the syringe through the septum to withdraw 100 µL of gas. Fresh nail polish was applied to reseal the septum after each sampling to prevent leakage. For initial catalysis experiments, a single measurement was taken after 300 min of irradiation. In contrast, for kinetic studies, measurements were performed at set time intervals: 0 min, 30 min, 60 min, 120 min, 180 min, 240 min, and 300 min after irradiation.

Time-Dependent Raman Measurements: The prepared cuvette was placed in the Raman spectrometer with direct contact to the probe-end of a 785 nm single-frequency laser diode. Before measuring the sample, the system was white light calibrated and one dark spectrum with an integration time of 5 seconds and 20 accumulations was performed. For the sample measurements the same integration times and accumulations as the dark spectrum were used and the spectrometer was set to continuous measurements, resulting in a measurement interval of 100 seconds over a duration of at least 300 minutes after which the measurement was manually terminated.

Cyclic voltammetry: All measurements were carried out in an argon filled glove box using a CH Instruments potentiostat. Each measurement was taken with concentrations of 1 mM [Mo2O2S6]2- and 0.1 M $TBAPF_6$ as supporting electrolyte at a scan rate of 100 mV s^{-1} using a glassy carbon working electrode, a Pt wire counter electrode, and an $Ag/AgNO_3$ reference electrode in MeCN.

Data processing

Turnover number (TON) and turnover frequency (TOF):

To determine the TON, the volume of the gas phase in the vial was calculated using the following equation:

$$\mathrm{V_{gas}} = \mathrm{V_{vial}} - \mathrm{V_{sol}} \qquad [28]$$

V_{gas}: gas volume of the vial. V_{vial}: total volume of the vial. V_{sol}: volume of the catalytic solution. The sample volume taken is 100 µL. To calculate the absolute amount of hydrogen evolved a vial-specific factor k_{vial} is calculated using equation 29 (to account for the amount of gas extracted for the GC-measurement):

$$\mathrm{k_{vial}} = \frac{\mathrm{V_{gas}}}{100\ \mu\mathrm{L}} \qquad [29]$$

The absolute amount of hydrogen evolved $H_{2,\,abs}$ can then be determined using the determined amount of hydrogen $n_{measured}$ per 100 µL, using the following equation:

$$n_{\mathrm{H_2,abs}} = \mathrm{n_{measured}} \cdot \mathrm{k_{vial}} \qquad [30]$$

The TON is the ratio of the amount of hydrogen formed $H_{2,abs}$ and the amount of catalyst in the solution n_{CAT}:

$$\mathrm{TON} = \frac{n_{\mathrm{H_2,abs}}}{n_{\mathrm{cat}}} \qquad [31]$$

The turnover frequency (TOF) is calculated as the TON per time (t):

$$\mathrm{TOF} = \frac{\mathrm{d\ TON}}{d\ t} \qquad [126] \qquad [32]$$

Table 21: Determined TON for individual solvents.

Measurement	TON (MeOH)	TON (MeOH: H_2O, 9:1, v:v)	TON (MeOH: H_2O, 1:1, v:v)	TON (H_2O)
1	356	251	58	25
2	328	204	95	46
3	266	92	180	28
4	391	152	151	28
5	576	149	65	38
6	546	147	51	29
7	611	148	93	-
8	652	178	83	-

9	310	-	144	-
10	392	-	143	-
11	677	-	136	-
12	781	-	131	-
13	746	-	201	-
14	785	-	149	-

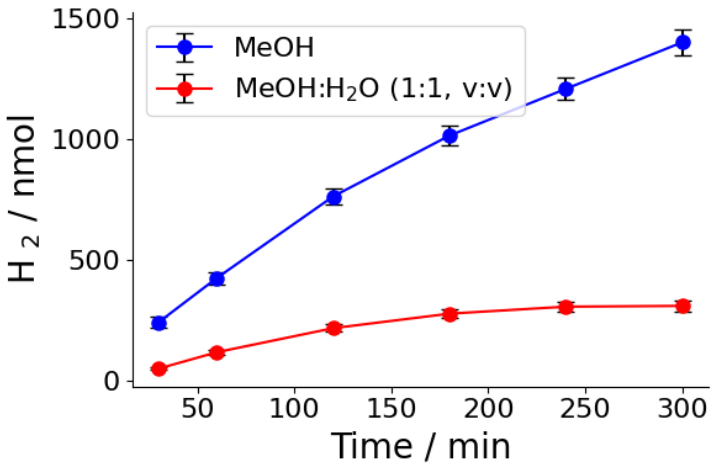

Figure 59: Amount of hydrogen evolved vs. time.

Table 22: Absolute amount of hydrogen of differently prepared stock solutions and control experiment without catalyst.

Experiment	Absolute amount H_2 / nmol
Freshly dissolved stock solution	625 ± 82
90 min ambient light irradiated	525 ± 10
90 min 465 nm irradiated	1320 ± 20
Without catalyst	60 ± 10

Normalized rate constants (from Raman Measurements):

To enable a comparative analysis of the numerous kinetic measurements, normalized rate coefficients were calculated. For the decay of the characteristic Raman signal of $[Mo_2O_2S_6]^{2-}$ at 560 cm^{-1} under different reaction conditions (solvents and irradiation) an exponential decay model was applied to fit the observed signal decay curves. Figure S3 shows an example of this approach. The corresponding decay coefficients (k_{dec}) were determined by rearranging the exponential decay equation:

$$y = y_0 + A_1 \cdot e^{-t \cdot k_{dec}} \qquad [33]$$

where y is the intensity at the characteristic wavenumber (560 cm^{-1}), y_0 is the intercept, t is the time in minutes, and A_1 is a scaling factor.

Table 23: Normalized rate constants k_{dec} for $[Mo_2O_2S_6]^{2-}$ in different solvents and under different irradiation conditions.

Solvent	k_{dec} (min^{-1}) No Irradiation
MeOH	0.04 ± 0.01
MeOH:H_2O (1:1, v:v)	0.018 ± 0.004
H_2O	0.10 ± 0.05

Measurements were performed in duplicates.

Computational Data

For each catalyst and catalyst derivative Gibbs free energy of a reduction step (ΔG_{ET}):

$$[\mathrm{CAT}]^n + e^- \rightarrow [\mathrm{CAT}]^{n-1}, \quad [34]$$

of a protonation step (ΔG_{PT}):

$$[\mathrm{CAT}]^n + H^+ \rightarrow \mathrm{H}[\mathrm{CAT}]^{n+1}, \quad [35]$$

and of a PCET (ΔG_{PCET}):

$$[\mathrm{CAT}]^n + H^0 \rightarrow \mathrm{H}[\mathrm{CAT}]^{n}, \quad [36]$$

were calculated using equations [37], [38] and [39] respectively. $[\mathrm{CAT}]^n$ was considered to be in singlet state, whereas $[\mathrm{CAT}]^{n-1}$ and $[\mathrm{CAT}]^{n+1}$ were assumed to adopt triplet spin multiplicity.

$$\Delta G_{\mathrm{ET}} = G([\mathrm{CAT}]^{n-1}) - G([\mathrm{CAT}]^n) + G(e^-) \quad [37]$$

$$\Delta G_{\mathrm{PT}} = G(\mathrm{H}[\mathrm{CAT}]^{n+1}) - G([\mathrm{CAT}]^n) - G(H^+) \quad [38]$$

$$\Delta G_{\mathrm{PCET}} = G(\mathrm{H}[\mathrm{CAT}]^{n}) - G([\mathrm{CAT}]^n) - G(H^0) \quad [39]$$

The Gibbs free energy of an electron ($G(e^-)$) was calculated by subtracting the Gibbs free energy of the oxidized PS ($G([Ru(bpy)_3]^{2+})$) from the free energy of the reduced PS ($G([Ru(bpy)_3]^{1+})$), as seen in equation [40]:

$$G(e^-) = G([\mathrm{Ru(bpy)_3}]^{1+}) - G([\mathrm{Ru(bpy)_3}]^{2+}) \quad [40]$$

The free energy of a proton is calculated using the energy of ascorbic acid (G(HAsc)) subtracted by the energy of deprotonated ascorbic acid ($G(Asc^-)$):

$$G(H^+) = G(\mathrm{HAsc}) - G(\mathrm{Asc}^-). \quad [41]$$

The energy of a hydrogen atom is calculated by adding the energies of an electron and a proton:

$$G(H^0) = G(H^+) + G(e^-). \qquad [42]$$

The hydrogen adsorption free energy for the catalysts during HER (ΔG_{ads}(H) is calculated by subtracting the energies of the initial catalyst (G(H_{n-1}[CAT])) and of a hydrogen atom (G(H^0)) from the energy of the catalyst with an adsorbed hydrogen attached (G(H_n[CAT])), as seen in equation [16]:

$$\Delta G_{\mathrm{ads.}}(\mathrm{H}) = G(\mathrm{H_n[CAT]}) - G(\mathrm{H_{n-1}[CAT]}) - G(H^0), \qquad [43]$$

where n can either be 1 or 2.

UV-Vis spectroscopy

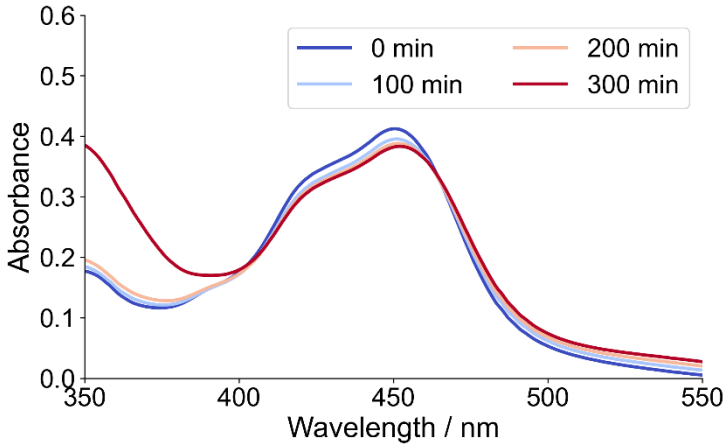

Figure 60: Time-dependent UV-Vis spectra of RuSED (c(PS) = 20 µM, c(SED) = 10 mM, pH 4) in pure methanol under irradiation with a 465 nm LED (P = 13 mW) for 5 h.

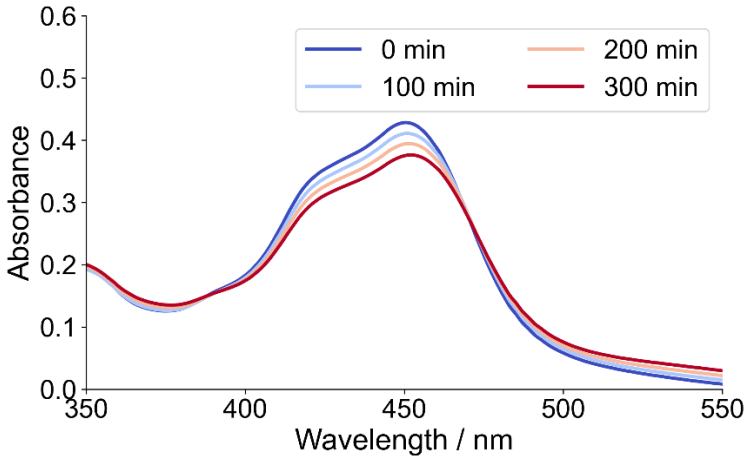

Figure 61: Time-dependent UV-Vis spectra of catalytic system (RuSEDCat: c(PS) = 20 µM, c(SED) = 10 mM, pH 4, c(Cat) = 0.5 µM) in pure methanol under irradiation with a 465 nm LED (P = 13 mW) for 5 h.

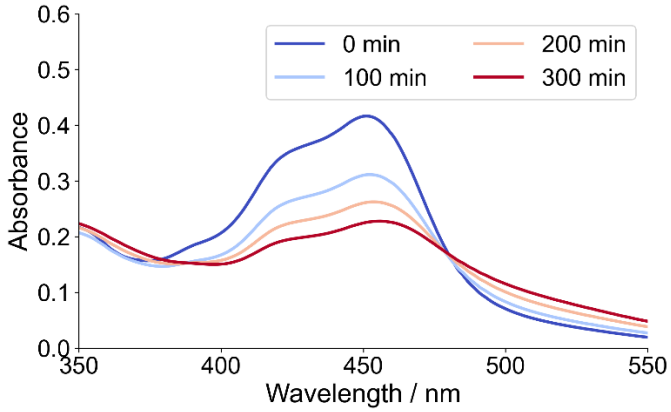

Figure 62: Time-dependent UV-Vis spectra of RuSED (c(PS) = 20 µM, c(SED) = 10 mM, pH 4) in a 1:1 mixture of water and methanol (v:v) under irradiation with a 465 nm LED (P = 13 mW) for 5 h.

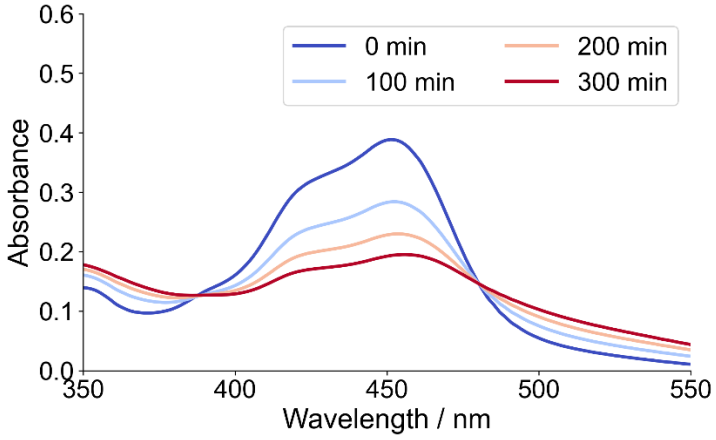

Figure 63: Time-dependent UV-Vis spectra of catalytic system (RuSEDCat: c(PS) = 20 µM, c(SED) = 10 mM, pH 4, c(Cat) = 0.5 µM) in a 1:1 mixture of water and methanol (v:v) under irradiation with a 465 nm LED (P = 13 mW) for 5 h.

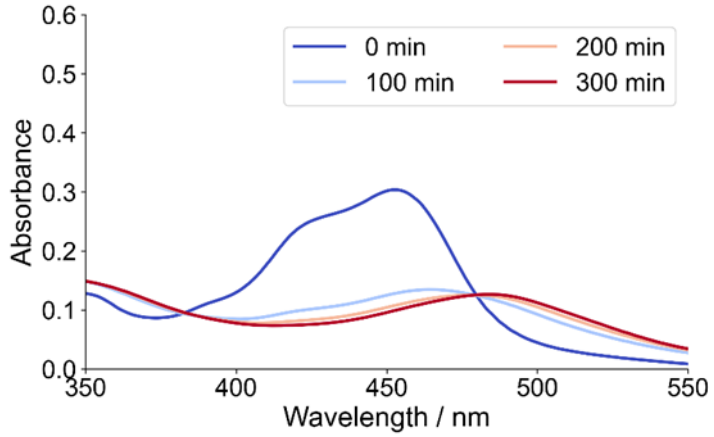

Figure 64: Time-dependent UV-Vis spectra of RuSED (c(PS) = 20 µM, c(SED) = 10 mM, pH 4) in pure water under irradiation with a 465 nm LED (P = 13 mW) for 5 h.

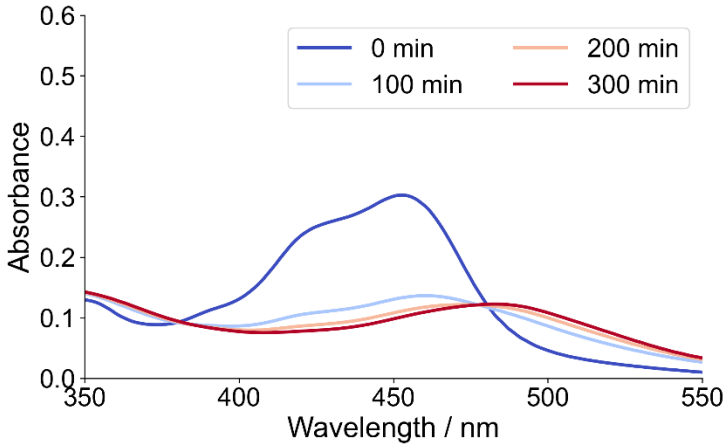

Figure 65: Time-dependent UV-Vis spectra of catalytic system (RuSEDCat: c(PS) = 20 µM, c(SED) = 10 mM, pH 4, c(Cat) = 0.5 µM) in pure water under irradiation with a 465 nm LED (P = 13 mW) for 5 h.

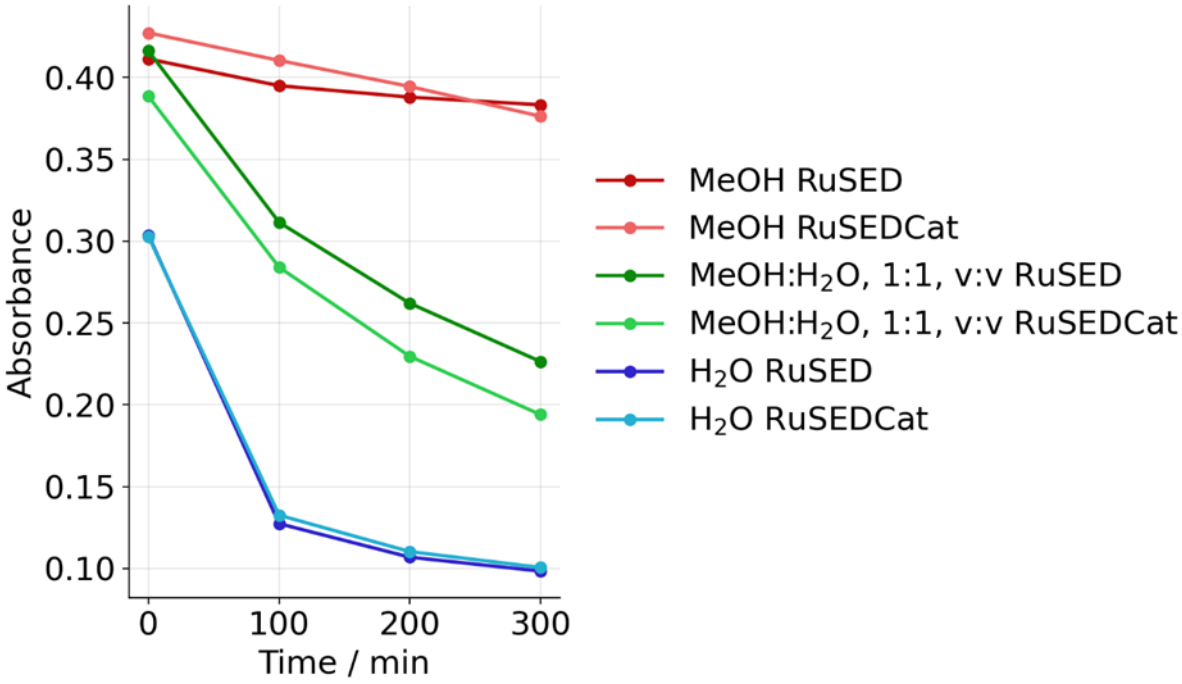

Figure 66: Absorbance of the 452 nm band of $[Ru(bpy)_3]^{2+}$ in the catalytic system (RuSEDCat: c(PS) = 20 µM, c(SED) = 10 mM, pH 4, c(Cat) = 0.5 µM) with and without catalyst system (RuSED: c(PS) = 20 µM, c(SED) = 10 mM, pH 4) in pure methanol, pure water and a 1:1 mixture of water and methanol (v:v). Irradiation for 5 h with a 465 nm LED (P = 13 mW).

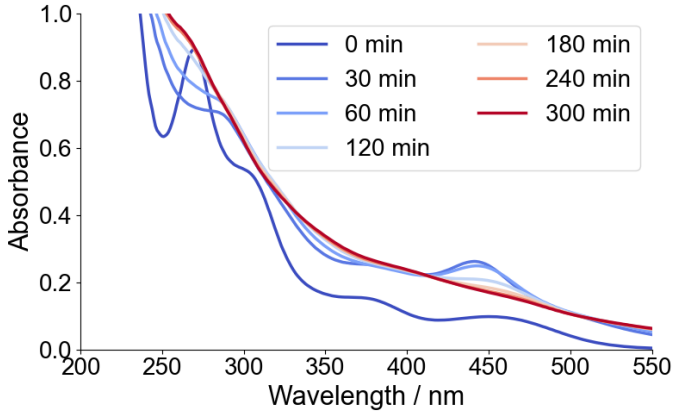

Figure 67: Time-dependent UV-Visspectra of $[Mo_2O_2S_6]^{2-}$ in MeOH:H_2O (1:1, v:v) over the course of 300 min irradiation with a 465 nm LED (P = 13 mW).

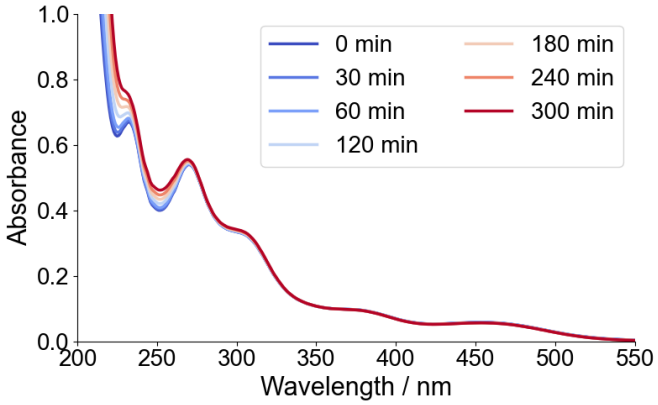

Figure 68: Time-dependent UV-Vis spectra of $[Mo_2O_2S_6]^{2-}$ in pure methanol over the course of 300 min under no irradiation.

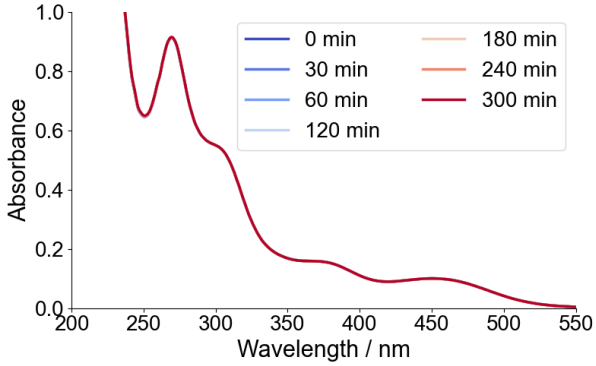

Figure 69: Time-dependent UV-Vis spectra of $[Mo_2O_2S_6]^{2-}$ in MeOH:H_2O (1:1, v:v) over the course of 300 min under no irradiation.

Computational Details

All DFT calculations in this work were performed using the **ORCA 5.0** software package[200,201]. In accordance with benchmarking the **Tao–Perdew–Staroverov–Scuseria functional** with additional incorporation of exact Hartree–Fock exchange (**TPSSh**)[202] was used for all calculations. The **def2-type** basis set of triple-zeta quality within the valence region, with an additional polarization function (**def2-TZVP**)[203], was employed together with **Grimme's D3BJ dispersion correction**, as implemented in the ORCA 5.0 software package[204,205]. The **effective core potentials (ECPs)** for molybdenum were likewise taken from the ORCA 5.0 implementation[206]. Implicit solvation effects in **water** and **methanol** were included in all calculations using the **CPCM continuum model[185]**, which treats the bulk solvent as a conductor-like polarizable continuum with the defined dielectric constant of methanol. For all **SCF processes**, convergence was set to six-digit precision (threshold of 10^{-6}) with a maximum of 250 iterations. For the computation of **analytic and numerical**

vibrational frequencies within the harmonic approximation, **ideal gas conditions** at **298.15 K** temperature and **1.01325 bar** pressure were applied. Before each frequency calculation, a **geometry optimization** was performed at the **TPSSh / def2-TZVP / D3BJ / (CPCM)** level of theory, and the resulting optimized geometry was subsequently used for the frequency calculation (see equations [37] – [39]). In order to ensure the investigation of ground-state molecules, frequency calculations were employed to confirm that a given structure does **not** represent a transition state and exhibits **no imaginary frequencies**.

Benchmarking

Benchmarking of calculation parameters was performed to evaluate the reliability of the chosen computational methods and to ensure accurate prediction of structural and spectroscopic properties. The evaluation of suitable functionals in this study was performed by comparing simulated IR spectra of $[Mo_2O_2S_6]^{2-}$ with experimental reference spectra. The scope of testing different functionals in this work is limited to a direct comparison of the results generated via the TPSSh and the B3LYP functional[207,208] to experimental data as previous considerations have been restricted to these functionals. For all calculations, the def2-TZVP basis set as well as Grimme's D3BJ dispersion correction were used in order to best compare both functionals.

Table 24: Measured, characteristic IR active vibrational frequencies of $[Mo_2O_2S_6]^{2-}$ and calculated vibrational frequencies at B3LYP-D3BJ / def2-TZVP and TPSSh-D3BJ / def2-TZVP levels of theory.

ν_{exp} / cm^{-1}	ν_{calc} (B3LYP) / cm^{-1}	ν_{calc} (TPSSh) / cm^{-1}	Characterization
463	462	468	$\nu_{asym}(Mo–S–Mo)_{bridged}$
512	507	519	$\nu_{asym}(S–S)_{terminal}$
926	986	981	$\nu_{asym}(S–S)_{terminal}$
1278	999	994	$\nu_{sym}(Mo=O)$
1477	1311	1325	$\nu_{sym}(Mo=O)$

For this molecule, it becomes apparent that the two tested functionals do not differ significantly from one another in their description of the molecular properties of thiomolybdates. Although the B3LYP functional showed results slightly more in line with the most important vibrational modes from the experimental data compared to TPSSh. However, the B3LYP functional showed inconsistent performance in further calculations. These inconsistencies became especially apparent during geometry optimization and vibrational calculations involving hydrated catalysts, as some of the equilibrium states could not be calculated reliably. To ensure consistent results, the TPSSh functional was therefore selected for further simulations.

Time-Dependent Raman Measurements

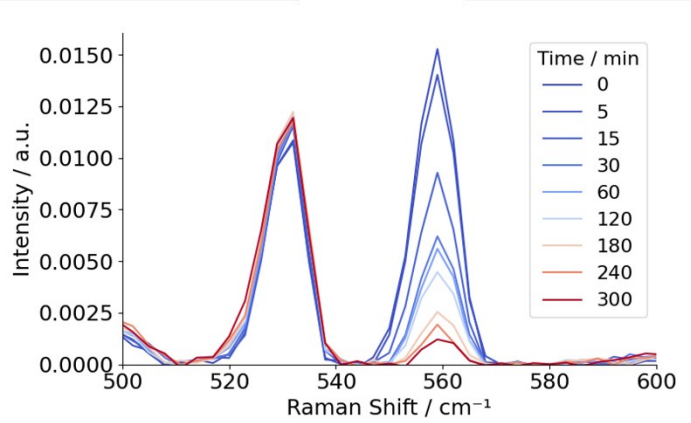

Figure 70: Normalized (to solvent) time dependent Raman spectra of $[Mo_2O_2S_6]^{2-}$ (c = 2.5 mM) in MeOH:H_2O (1:1, v:v).

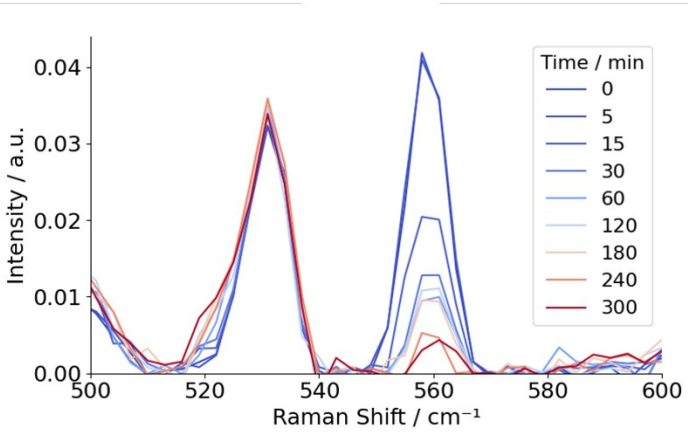

Figure 71: Normalized (to solvent) time dependent Raman spectra of $[Mo_2O_2S_6]^{2-}$ (c = 2.5 mM) in H_2O.

Another aspect to observe in the Raman spectra is the relative intensity of the 530 cm^{-1} band compared to the 560 cm^{-1} band. The higher the water content the higher the 530 cm^{-1} band is. We assign this to changes of the solvent polarity depending on the MeOH:H_2O solvent composition. This is in line with the principles of Raman spectroscopy, where Raman intensities reflect changes in molecular polarizability rather than directly corresponding to concentration changes. Thus, changes of the solvent polarity are expected to affect the polarizability of the catalyst also.

Cyclovoltammetry

Measurements were performed in the presence and absence of ascorbic acid as proton donor. The voltammogram of $[Mo_2O_2S_6]^{2-}$ (Figure 72), reveals a reduction at −1.1 V that is assigned to the one-electron reduction of the catalyst.[209] The corresponding oxidation wave is observed at −0.64 V. The peak separation between the waves indicates slow heterogeneous electron-transfer kinetics. The reduction at −2.4 V shows the highest cathodic peak current, whereas the corresponding anodic return wave exhibits a markedly smaller current. This pronounced mismatch indicates that the reduced species is not fully regenerated during the reverse scan, indicating a subsequent chemical step following the electrochemical reduction. This can be assigned to a catalytic process, or to cluster degradation. Also, two oxidation processes are observed at +0.11 V and +0.48 V. The absence of well-defined corresponding reduction peaks suggests significant structural reorganization of the oxidized species, consistent with literature reports that attribute such processes to successive oxidations of the dimolybdenum core.[210] A further

irreversible oxidation at approximately +1.1 V is assigned to oxidation of the disulfide ligands.[196] Upon addition of ascorbic acid as a proton source, only moderate changes in the voltammogram are observed. The Mo-centered one-electron reduction shifts cathodically by ~100 mV to −1.25 V. Furthermore, the two oxidation waves at +0.11 V and +0.48 V collapse into a single oxidation feature at +0.09 V, while the irreversible oxidation attributed to the disulfide ligand remains largely unaffected.

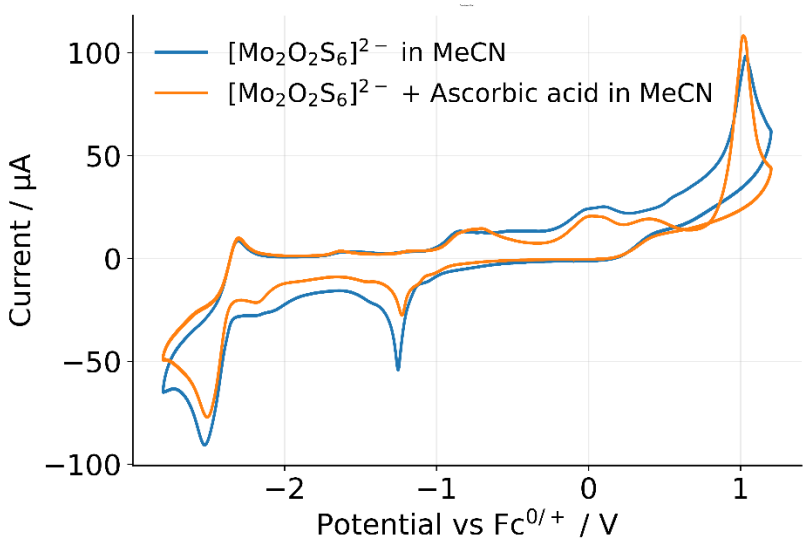

Figure 72: Cyclic voltammograms of $[Mo_2O_2S_6]^{2-}$ recorded in MeCN (0.1 M $TBAPF_6$, glassy carbon working electrode, Pt wire counter electrode, $Ag/AgNO_3$ reference electrode, scan rate 100 mV s^{-1}). The voltammogram of the parent complex (blue) is compared to measurements in the presence of ascorbic acid as a proton source (orange). Upon addition of ascorbic acid, the Mo-centered reduction shifts cathodically and the two oxidation waves observed for the parent complex collapse into a single oxidation feature, while the irreversible high-potential oxidation attributed to the disulfide ligand remains largely unchanged.

MeOH titration experiments were performed by stepwise addition of methanol in stoichiometric ratios of 1, 2, 4, 6, 10, and 20 equivalents relative to the complex, both in the absence and presence of ascorbic acid (Figure 73a, b). The titration experiments were performed as follows: a stock solution was prepared containing methanol (16 mM) in acetonitrile. Electrochemical experiments were carried out starting with a solution of $[Mo_2O_2S_6]^{2-}$ in acetonitrile (1 mM, 2 mL total volume). To this solution, aliquots of the methanol stock solution were added and CVs were measured at catalyst:MeOH ratios ranging from 0 – 20. This resulted in a final volume of 4.5 mL, corresponding to a molar ratio of catalyst:MeOH = 1:20. The resulting dilution (from 2 ml to 4.5 ml) accounts for the observed ~50% decrease in peak current.

In both series, a gradual decrease of the high-potential oxidation at +1.1 V attributed to the disulfide ligand is observed, consistent with progressive ligand exchange of the disulfide unit by methanol. In parallel, the overall anodic current at positive potentials decreases. Note that the reduction in peak currents primarily reflects dilution of the sample upon addition of methanol. These findings further support the proposed ligand exchange. For the one-electron reduction at -1.1 V a cathodic shift can be observed upon methanol addition. The current peak shifts -33 mV and -41 mV upon the presence of ascorbic acid, respectively. Note, that these measurements only show initial electrochemical properties and were performed under different reaction conditions than photocatalytic conditions.

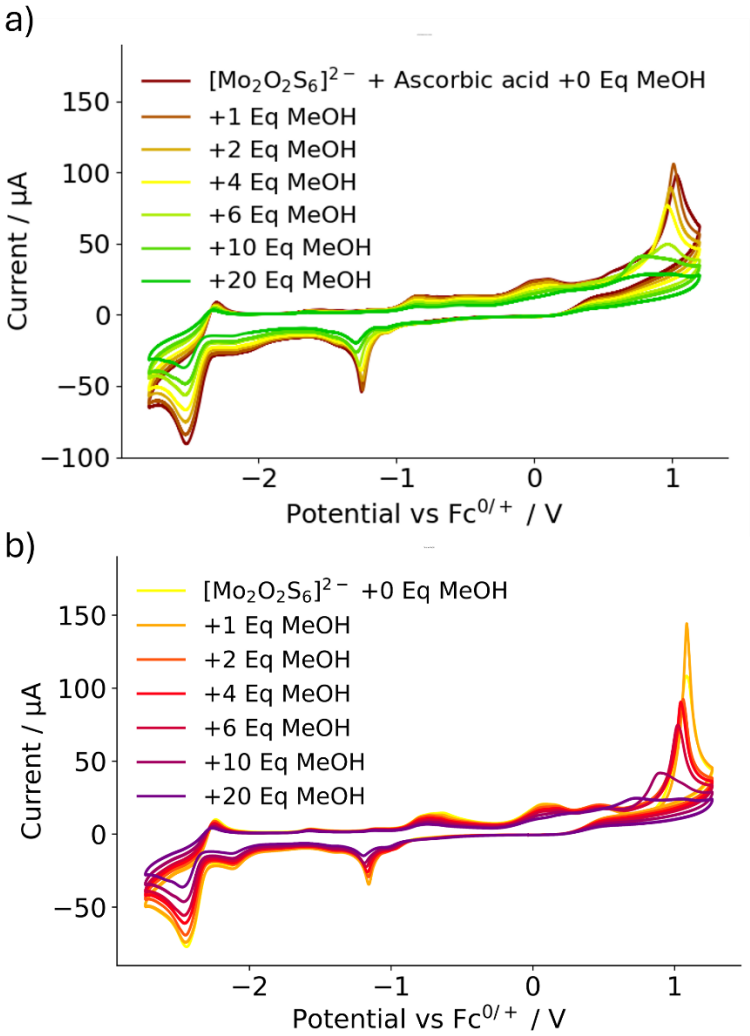

Figure 73: Cyclic voltammograms of $[Mo_2O_2S_6]^{2-}$ recorded during stepwise methanol titration (0–20 equivalents) in MeCN (0.1 M $TBAPF_6$, glassy carbon working electrode, Pt wire counter electrode, $Ag/AgNO_3$ refer-ence electrode, scan rate 100 mV s^{-1}). a) measurements in the presence of ascorbic acid. b) measurements in the absence of ascorbic acid. Increasing methanol

concentration leads to a progressive decrease of the high-potential oxidation attributed to the disulfide ligand and a general decrease in anodic current at positive potentials.

4 Summary and Perspectives

Thiomolybdate clusters are well known as promising catalysts for the light-driven HER, while thio-oxo-molybdates are considered to be potentially similarly suitable candidates. Although internal reaction conditions are often optimized in order to fully exploit the potential of a catalytic system, external reaction conditions such as irradiation are frequently neglected. The aim of this work was therefore to investigate the influence of light on homogeneous thiomolybdate and thio-oxo-molybdate systems. For thiomolybdates, the effects of dynamic irradiation on catalytic performance as well as on light-induced processes were examined. For thio-oxo-molybdates, initial catalytic and mechanistic studies on the homogeneous light-driven HER were carried out, with particular emphasis on the role of irradiation.

4.1 Influence of dynamic irradiation on the homogeneous light-driven HER using thiomolybdates

A DoE approach was used to investigate the influence of dynamic irradiation on photocatalytic systems for the light-driven HER employing either **{Mo_3}** or **{Mo_2}** as catalyst. In both studies, the individual effects of the three irradiation parameters—frequency, duty cycle, and LED current—as well as their interactions were identified. In the **{Mo_3}** system, LED current showed the strongest influence on TON, followed by duty cycle, whereas in the **{Mo_2}** system this order was reversed. In both systems, frequency had the smallest effect. Furthermore, an interaction between frequency and duty cycle was identified for both systems, while the **{Mo_2}** system exhibited an additional interaction between LED current and duty cycle.

Based on the analyzed data, a process optimization aiming to maximize TON was performed for both systems. In both cases, the optimal irradiation conditions were predicted to be a frequency of 2 Hz, a duty cycle of 75%, and an LED current of 700 mA. Under these conditions, the **{Mo_3}** system showed a 102% increase in TON compared to

the static benchmark experiment, whereas the **{Mo_2}** system exhibited a 4% increase. Notably, under the optimized dynamic irradiation conditions, 25% less energy was introduced into the system than in the corresponding static benchmark experiments. As a result, the photonic efficiencies also increased and were discussed in more detail.

Photodegradation of the PS could be excluded as the main explanation for the improved catalytic performance. Instead, UV–Vis spectroscopic investigations showed that both catalysts undergo light-induced ligand exchange in solution, which may lead to structural degradation of the clusters. The enhanced catalytic activity observed under dynamic irradiation can therefore be partially explained by reduced photodegradation of the thiomolybdate clusters. In addition, the hypothesis was proposed that hydrogen evolution may partially proceed as a dark reaction, implying that the system alternates between charging and discharging states depending on the irradiation conditions. However, this assumption requires further investigation.

From a future perspective, these studies demonstrate that the DoE approach enables a statistical identification of relevant influence factors while minimizing the number of experiments required. Its application in photocatalysis may therefore lead to faster and more robust data analysis. Both studies further show that tailored irradiation conditions can reveal previously unrecognized potential in known photocatalytic systems, thereby enabling more energy- and resource-efficient photocatalysis. Finally, an important common finding of both studies is that thiomolybdate clusters undergo light-induced ligand exchange in solution.

4.2 Catalytic and mechanistic studies on thio-oxo-molybdates for the light-driven HER

Thio-oxo-molybdates are considered promising candidates for the HER, but their application in photocatalysis has so far received only limited attention. To address this knowledge gap, the $[Mo_2O_2S_6]^{2-}$ cluster was used as a prototype catalyst to investigate both its suitability for HER catalysis and the influence of light on thio-oxo-molybdate systems. Initial catalytic studies revealed that the highest TON, approximately 530, was achieved in pure methanol due to enhanced PS stability compared to aqueous solution. This TON is of the same order of magnitude as that observed for thiomolybdates under

comparable conditions. Further investigations using Raman spectroscopy showed that the cluster undergoes ligand exchange similar to that known for thiomolybdates, in which terminal disulfide ligands are replaced by solvent ligands. UV–Vis spectroscopic studies further demonstrated that this ligand exchange is light-induced. TOF measurements and additional catalytic experiments indicated that the ligand-exchanged species is catalytically more active than the initial cluster. At the same time, degradation of the overall photochemical system appears to be the main factor limiting the system lifetime. Quantum-chemical calculations further support the hypothesis that both species, $[Mo_2O_2S_4(MeOH)_2]^0$ and $[Mo_2O_2S_4(H_2O)_2]^0$, exhibit higher catalytic activity than the $[Mo_2O_2S_6]^{2-}$ cluster.

Overall, this study demonstrates that thio-oxo-molybdates are also promising catalysts for the light-driven HER. Since the ligand-exchanged species exhibit higher catalytic activity and appear to remain stable under the reaction conditions, they may represent a more active and longer-lived alternative to the initial $[Mo_2O_2S_6]^{2-}$ cluster.

5 References

[1] V. Eyring, N. P. Gillett, K. M. Achuta Rao, R. Barimalala South Africa, M. Barreiro, L. Bock, E. Malinina, L. Ruiz, J.-B. Sallée, B. D. Santer, B. Trewin, K. Weigel, X. Zhang, A. Zhao, T. Halenka, J. A. Marengo Orsini Brazil, D. Mitchell, N. Gillett, K. Achuta Rao, R. Barimalala, M. Barreiro Parrillo, N. Bellouin, C. Cassou, P. Durack, Y. Kosaka, S. McGregor, S. Min, O. Morgenstern, Y. Sun, P. Zhai, A. Pirani, S. Connors, C. Péan, S. Berger, N. Caud, Y. Chen, L. Goldfarb, M. Gomis, M. Huang, K. Leitzell, E. Lonnoy, J. Matthews, T. Maycock, T. Waterfield, O. Yelekçi, R. Yu, B. Zhou, *Human Influence on the Climate System*, Cambridge University Press, Cambridge, United Kingdom and New York, NY, USA, **2021**.

[2] P. Friedlingstein, M. O'sullivan, M. W. Jones, R. M. Andrew, J. Hauck, P. Landschützer, C. Le Quéré, H. Li, I. T. Luijkx, A. Olsen, G. P. Peters, W. Peters, J. Pongratz, C. Schwingshackl, S. Sitch, J. G. Canadell, P. Ciais, J. Zeng, et al., *Earth Syst. Sci. Data* **2025**, *17*, 965–1039.

[3] T. Dietz, E. A. Rosa, *Proc. Natl. Acad. Sci. U. S. A.* **1997**, *94*, 175.

[4] P. Pablo-Romero, R. Pozo-Barajas, J. Sánchez, R. García, J. L. Holechek, H. M. E. Geli, M. N. Sawalhah, R. Valdez, *Sustainability* **2022**, *14*, 4792.

[5] P. J. Megia, A. J. Vizcaino, J. A. Calles, A. Carrero, *Energy and Fuels* **2021**, *35*, 16403–16415.

[6] Opio C, Gerber P, Mottet A, Falcucci A, Tempio G, MacLeod M, Vellinga T, Henderson B, Steinfeld H, *Animal Production and Health Division A Global Life Cycle Assessment Greenhouse Gas Emissions from Ruminant Supply Chains*, Rome, **2013**.

[7] W. Zhong, J. D. Haigh, *Royal Meteorological Society* **2013**, *68*, 100–105.

[8] R. T. Pierrehumbert, *Phys. Today* **2011**, *64*, 33–38.

[9] N. Mimura, *Proc. Jpn. Acad. Ser. B Phys. Biol. Sci.* **2013**, *89*, 281.

[10] R. J. Nicholls, A. Cazenave, *Science (1979).* **2010**, *328*, 1517–1520.

[11] D. Cui, S. Liang, D. Wang, *Wiley Interdiscip. Rev. Clim. Change* **2021**, *12*, e701.

[12] D. Chan, Q. Wu, *Scientific Reports 2015 5:1* **2015**, *5*, 13487-.

[13] S. M. Vicente-Serrano, S. M. Quiring, M. Peña-Gallardo, S. Yuan, F. Domínguez-Castro, *Earth. Sci. Rev.* **2020**, *201*, 102953.

[14] E. L. Williams, J. T. Abatzoglou, K. C. Hegewisch, A. P. Williams, *Communications Earth & Environment 2024 5:1* **2024**, *5*, 546-.

[15] K. J. E. Walsh, J. L. Mcbride, P. J. Klotzbach, S. Balachandran, S. J. Camargo, G. Holland, T. R. Knutson, J. P. Kossin, T.-C. Lee, A. Sobel, M. Sugi, *WIREs Clim Change* **2015**, DOI 10.1002/wcc.371.

[16] L. Wu, H. Zhao, C. Wang, J. Cao, J. Liang, *Advances in Atmospheric Sciences 2022 39:2* **2022**, *39*, 205–221.

[17] I. Graabak, M. Korpås, *Energies 2016, Vol. 9, Page 449* **2016**, *9*, 449.

[18] P. Cosgrove, T. Roulstone, S. Zachary, *Renew. Energy* **2023**, *212*, 299–307.

[19] L. Liu, G. He, M. Wu, G. Liu, H. Zhang, Y. Chen, J. Shen, S. Li, *Nature Energy 2023 8:8* **2023**, *8*, 870–880.

[20] D. Heide, M. Greiner, L. von Bremen, C. Hoffmann, *Renew. Energy* **2011**, *36*, 2515–2523.

[21] Q. Chen, Z. Kuang, X. Liu, T. Zhang, *Appl. Energy* **2022**, *312*, 118744.

[22] J. Hirvonen, H. ur Rehman, K. Sirén, *Solar Energy* **2018**, *162*, 472–488.

[23] R. J. Mahfoud, N. F. Alkayem, Y. Zhang, Y. Zheng, Y. Sun, H. H. Alhelou, *Renewable and Sustainable Energy Reviews* **2023**, *178*, 113267.

[24] S. Rehman, L. M. Al-Hadhrami, M. M. Alam, *Renewable and Sustainable Energy Reviews* **2015**, *44*, 586–598.

[25] N. G. Chatzigeorgiou, S. Theocharides, G. Makrides, G. E. Georghiou, *J. Energy Storage* **2024**, *86*, 111192.

[26] T. Jaradat, T. Khatib, *Future Batteries* **2025**, *7*, 100106.

[27] A. R. Dahiru, A. Vuokila, M. Huuhtanen, *J. Energy Storage* **2022**, *56*, 105861.

[28] L. Colelli, S. Dell'Aversano, C. Bassano, G. Vanga, K. Gallucci, G. Vilardi, *Energy Convers. Manag.* **2026**, *347*, 120529.

[29] M. Ozturk, I. Dincer, *Int. J. Hydrogen Energy* **2021**, *46*, 31511–31522.

[30] A. M. Elberry, J. Thakur, J. Veysey, *J. Energy Storage* **2021**, *44*, 103474.

[31] R. Bhandari, N. Adhikari, *Int. J. Hydrogen Energy* **2024**, *82*, 923–951.

[32] S. S. Muir, X. Yao, *Int. J. Hydrogen Energy* **2011**, *36*, 5983–5997.

[33] M. G. Rasul, M. A. Hazrat, M. A. Sattar, M. I. Jahirul, M. J. Shearer, *Energy Convers. Manag.* **2022**, *272*, 116326.

[34] H. Ellison, *Energy for a Sustainable World: From the Oil Age to a Sun-Powered Future*, Wiley-VCH, Weinheim, **2011**.

[35] I. Rolo, V. A. F. Costa, F. P. Brito, *Energies 2024, Vol. 17, Page 180* **2023**, *17*, 180.

[36] D. Saygin, H. Blanco, F. Boshell, J. Cordonnier, K. Rouwenhorst, P. Lathwal, D. Gielen, *Sustainability* **2023**, *15*, 1623.

[37] S. Mingolla, L. Rosa, *Nature Food 2025 6:6* **2025**, *6*, 610–621.

[38] R. Arshad, I. Skalidis, D. Kopečný, S. Brabencová, M. Opatíková, P. Ilík, P. Pospíšil, F. Hamdi, S. Ćavar Zeljković, M. Kopečná, P. Roudnický, D. Lazár, E. Elias, R. Croce, P. L. Kastritis, R. Kouřil, *Nature Communications 2025 17:1* **2026**, *17*, 341-.

[39] N. Nelson, C. F. Yocum, *Annu. Rev. Plant Biol.* **2006**, *57*, 521–565.

[40] B. E. Schirrmeister, J. M. De Vos, A. Antonelli, H. C. Bagheri, *PNAS* **2013**, *110*, 1791–1796.

[41] T. Matsuo, K. Ito-Miwa, Y. Hoshino, Y. I. Fujii, S. Kanno, K. J. Fujimoto, R. Tsuji, S. Takeda, C. Onami, C. Arai, Y. Yoshiyama, Y. Mino, Y. Kato, T. Yanai, Y. Fujita, S. Masuda, T. Kakegawa, H. Miyashita, *Nature Ecology & Evolution 2025 9:4* **2025**, *9*, 599–612.

[42] N. Nelson, *Biochimica et Biophysica Acta (BBA) - Bioenergetics* **2011**, *1807*, 856–863.

[43] J. A. Bassham, *Proc. Nat. Acad. Sci. USA* **1971**, *68*, 2877–2882.

[44] J. M. Berg, J. L. Tymoczko, L. Stryer, *Biochemie: Evolution Einer Wissenschaft*, Springer Spektrum, Berlin, Heidelberg, **2013**.

[45] B. König, *Chemical Photocatalysis*, De Gruyter, Berlin, Boston, **2020**.

[46] J. Knoppová, R. Sobotka, J. Yu, M. Bečková, J. Pilný, J. P. Trinugroho, L. Csefalvay, D. Bína, P. J. Nixon, J. Komenda, *Plant Physiol.* **2022**, *189*, 790–804.

[47] A. R. Holzwarth, M. G. Müller, M. Reus, M. Nowaczyk, J. Sander, M. Rögner, *Proc. Natl. Acad. Sci. U. S. A.* **2006**, *103*, 6895–6900.

[48] M. Hervás, J. A. Navarro, M. A. De La Rosa, *Acc. Chem. Res.* **2003**, *36*, 798–805.

[49] J. Barber, *Cold Spring Harb. Symp. Quant. Biol.* **2012**, *77*, 295–307.

[50] R. Höhner, A. Aboukila, H. H. Kunz, K. Venema, *Front. Plant Sci.* **2016**, *7*, 175050.

[51] S. Jarvit, P. J. Gollanf, E. M. Aro, *Front. Plant Sci.* **2013**, *4*, DOI 10.3389/FPLS.2013.00434.

[52] T. Sekiguchi, K. Yoshida, K. ichi Wakabayashi, T. Hisabori, *Journal of Biological Chemistry* **2024**, *300*, 107659.

[53] A. N. Webber, W. Lubitz, *Biochim. Biophys. Acta Bioenerg.* **2001**, *1507*, 61–79.

[54] P. Fromme, P. Jordan, N. Krauß, *Biochim. Biophys. Acta Bioenerg.* **2001**, *1507*, 5–31.

[55] J. Dunn, M. H. Grider, *StatPearls* **2023**.

[56] T. Förster, *Ann. Phys.* **1948**, *437*, 55–75.

[57] G. J. Kavarnos, *Springer, Berlin, Heidelberg* **2005**, *156*, 21–58.

[58] R. A. Marcus, *J. Chem. Phys.* **1956**, *24*, 966–978.

[59] T. Spatzal, M. Aksoyoglu, L. Zhang, S. L. A. Andrade, E. Schleicher, S. Weber, D. C. Rees, O. Einsle, *Science (1979).* **2011**, *334*, 940.

[60] D. Schilter, J. M. Camara, M. T. Huynh, S. Hammes-Schiffer, T. B. Rauchfuss, *Chem. Rev.* **2016**, *116*, 8693–8749.

[61] S. T. Stripp, T. Happe, *Dalton Transactions* **2009**, 9960–9969.

[62] M. T. Stiebritz, M. Reiher, *Chem. Sci.* **2012**, *3*, 1739–1751.

[63] J. W. Peters, G. J. Schut, E. S. Boyd, D. W. Mulder, E. M. Shepard, J. B. Broderick, P. W. King, M. W. W. Adams, *Biochimica et Biophysica Acta (BBA) - Molecular Cell Research* **2015**, *1853*, 1350–1369.

[64] A. S. Pandey, T. V. Harris, L. J. Giles, J. W. Peters, R. K. Szilagyi, *J. Am. Chem. Soc.* **2008**, *130*, 4533–4540.

[65] M. W. Adams, *J. Biol. Chem.* **1987**, *262*, 15054–15061.

[66] H. Ogata, K. Nishikawa, W. Lubitz, *Nature* **2015**, *520*, 571–574.

[67] T. Hiromoto, K. Ataka, O. Pilak, S. Vogt, M. S. Stagni, W. Meyer-Klaucke, E. Warkentin, R. K. Thauer, S. Shima, U. Ermler, *FEBS Lett.* **2009**, *583*, 585–590.

[68] F. V. Schmidt, L. Schulz, J. Zarzycki, S. Prinz, N. N. Oehlmann, T. J. Erb, J. G. Rebelein, *Nature Structural & Molecular Biology 2023 31:1* **2023**, *31*, 150–158.

[69] J. W. Peters, R. K. Szilagyi, *Curr. Opin. Chem. Biol.* **2006**, *10*, 101–108.

[70] R. R. Eady, *BioFactors* **1988**, *1*, 111–116.

[71] A. N. Glazer, K. J. Kechris, *PLoS One* **2009**, *4*, e6136.

[72] S. Batool, M. Langer, S. N. Myakala, M. Heiland, D. Eder, C. Streb, A. Cherevan, *Advanced Materials* **2024**, *36*, DOI 10.1002/adma.202305730.

[73] M. A. Zabara, B. Ölmez, M. Buldu-Akturk, B. Yarar Kaplan, A. C. Kırlıoğlu, S. Alkan Gürsel, M. Ozkan, C. S. Ozkan, A. Yürüm, *Global Challenges* **2024**, *8*, 2400011.

[74] M. Drosou, F. Kamatsos, C. A. Mitsopoulou, *Inorg. Chem. Front.* **2019**, *7*, 37–71.

[75] E. Amouyal, *Solar Energy Materials and Solar Cells* **1995**, *38*, 249–276.

[76] A. Mazzeo, S. Santalla, C. Gaviglio, F. Doctorovich, J. Pellegrino, *Inorganica Chim. Acta* **2021**, *517*, 119950.

[77] E. Deponti, M. Natali, *Dalton Transactions* **2016**, *45*, 9136–9147.

[78] S. Yang, J. Han, W. Zhang, *Chemistry - A European Journal* **2023**, *29*, DOI 10.1002/CHEM.202302770.

[79] P. Sabatier, *La Catalyse En Chimie Organique*, Librairie Polytechnique, Paris, **1920**.

[80] L. Mawrie, F. Rahman, M. A. Ali, S. Gazi, *Appl. Catal. A Gen.* **2023**, *651*, 119010.

[81] D. M. Arias-Rotondo, J. K. McCusker, *Chem. Soc. Rev.* **2016**, *45*, 5803–5820.

[82] J. Van Houten, R. J. Watts, *Chemistry (Easton).* **1978**, *17*, 3381.

[83] V. Balzani, G. Bergamini, F. Marchioni, P. Ceroni, *Coord. Chem. Rev.* **2006**, *250*, 1254–1266.

[84] J. R. Lakowitcz, *Principles of Fluorescence Spectroscopy*, Springer, New York, **2006**.

[85] W. Pauli, Pauli, W., *ZPhy* **1925**, *31*, 765–783.

[86] F. Hund, *Zeitschrift für Physik* **1925**, *33*, 855–859.

[87] E. Condon, *Physical Review* **1926**, *28*, 1182.

[88] M. Kasha, *Discuss. Faraday Soc.* **1950**, *9*, 14–19.

[89] F. H. Burstall, *J. Chem. Soc.* **1936**, 173–175.

[90] W. W. Brandt, G. Frederick Smith, *Anal. Chem.* **1949**, *21*, 1313–1319.

[91] J. P. Paris, W. W. Brandt, *Journal American Chemical Society* **1959**, *81*, 5001–5002.

[92] G. Scattolini, A. Rosichini, N. Kaul, **2025**, DOI 10.1021/acs.inorgchem.5c03471.

[93] C. Creutz, N. Sutin, *J. Am. Chem. Soc.* **1976**, *98*, 6384–6385.

[94] J. V. Caspar, T. J. Meyer, *J. Am. Chem. Soc.* **1983**, *105*, 5583–5590.

[95] J. N. Demas, D. Diemente, E. W. Harris, *J. Am. Chem. Soc.* **1973**, *95*, 6864–6865.

[96] S. Roffia, R. Casadei, F. Paolucci, C. Paradisi, C. A. Bignozzi, F. Scandola, *J. Electroanal. Chem. Interfacial Electrochem.* **1991**, *302*, 157–171.

[97] B. Limburg, E. Bouwman, S. Bonnet, *ACS Catal.* **2016**, *6*, 5273–5284.

[98] I. M. Dixon, S. Bonnet, F. Alary, J. Cuny, *Journal of Physical Chemistry Letters* **2021**, *12*, 7278–7284.

[99] A. Soupart, F. Alary, J. L. Heully, P. I. P. Elliott, I. M. Dixon, *Inorg. Chem.* **2020**, *59*, 14679–14695.

[100] A. Soupart, F. Alary, J.-L. Heully, P. I. P. Elliott, I. M. Dixon, *Coord. Chem. Rev.* **2020**, *408*, DOI 10.1016/j.ccr.2020.213184.

[101] K. Eastham, P. A. Scattergood, D. Chu, R. Z. Boota, A. Soupart, F. Alary, I. M. Dixon, C. R. Rice, S. J. O. Hardman, P. I. P. Elliott, *Inorg. Chem.* **2022**, *61*, 19907–19924.

[102] D. Jespersen, B. Keen, J. I. Day, A. Singh, J. Briles, D. Mullins, J. D. Weaver, **2019**, DOI 10.1021/acs.oprd.9b00041.

[103] V. Balzani, A. Credi, M. Venturi, *ChemSusChem* **2008**, *1*, 26–58.

[104] M. Natali, E. Deponti, D. Vilona, A. Sartorel, M. Bonchio, F. Scandola, *Eur. J. Inorg. Chem.* **2015**, *2015*, 3467–3477.

[105] J. R. Darwent, P. Douglas, A. Harriman, G. Porter, M. C. Richoux, *Coord. Chem. Rev.* **1982**, *44*, 83–126.

[106] A. Nabiyan, J. B. Max, C. Neumann, M. Heiland, A. Turchanin, C. Streb, F. H. Schacher, *Chemistry – A European Journal* **2021**, *27*, 16924–16929.

[107] J. H. Shon, T. S. Teets, *ACS Energy Lett.* **2019**, *4*, 558–566.

[108] A. Juris, V. Balzani, F. Barigelletti, S. Campagna, P. Belser, A. von Zelewsky, *Coord. Chem. Rev.* **1988**, *84*, 85–277.

[109] E. Kozma, M. Catellani, *Dyes and Pigments* **2013**, *98*, 160–179.

[110] S. Batool, S. P. Nandan, S. N. Myakala, A. Rajagopal, J. S. Schubert, P. Ayala, S. Naghdi, H. Saito, J. Bernardi, C. Streb, A. Cherevan, D. Eder, *ACS Catal.* **2022**, *12*, 6641–6650.

[111] X. B. Fan, S. Yu, B. Hou, J. M. Kim, *Isr. J. Chem.* **2019**, *59*, 762–773.

[112] W. W. Yong, H. Lu, H. Li, S. Wang, M. T. Zhang, *ACS Appl. Mater. Interfaces* **2018**, *10*, 10828–10834.

[113] Y. Pellegrin, F. Odobel, *Comptes Rendus Chimie* **2017**, *20*, 283–295.

[114] J. Amaro-Gahete, M. V. Pavliuk, H. Tian, D. Esquivel, F. J. Romero-Salguero, S. Ott, *Coord. Chem. Rev.* **2021**, *448*, 214172.

[115] A. J. Bard, M. A. Fox, *Acc. Chem. Res* **1995**, *28*, 141–145.

[116] M. L. Grutza, A. Rajagopal, C. Streb, P. Kurz, *Sustain. Energy Fuels* **2018**, *2*, 1893–1904.

[117] Q. Yin, J. M. Tan, C. Besson, Y. V. Geletii, D. G. Musaev, A. E. Kuznetsov, Z. Luo, K. I. Hardcastle, C. L. Hill, *Science (1979).* **2010**, *328*, 342–345.

[118] R. S. Khnayzer, V. S. Thoi, M. Nippe, A. E. King, J. W. Jurss, K. A. El Roz, J. R. Long, C. J. Chang, F. N. Castellano, *Energy Environ. Sci.* **2014**, *7*, 1477–1488.

[119] I. Vural Gürsel, T. Noël, Q. Wang, V. Hessel, *Green Chemistry* **2015**, *17*, 2012–2026.

[120] J. M. Lehn, J. P. Sauvage, *Nouv. J. Chim* **1977**, *1*, 449–451.

[121] Y. Zhang, S. Pang, Z. Wei, H. Jiao, X. Dai, H. Wang, F. Shi, *Nature Communications 2018 9:1* **2018**, *9*, 1465-.

[122] M. D. Argyle, C. H. Bartholomew, *Catalysts 2015, Vol. 5, Pages 145-269* **2015**, *5*, 145–269.

[123] N. Shambhawi, O. Mohan, T. S. Choksi, A. A. Lapkin, *Catal. Sci. Technol.* **2024**, *14*, 515–532.

[124] F. Zaera, *Chem. Rev.* **2022**, *122*.

[125] M. D. Wilkinson, M. Dumontier, Ij. J. Aalbersberg, G. Appleton, M. Axton, A. Baak, N. Blomberg, J. W. Boiten, L. B. da Silva Santos, P. E. Bourne, J. Bouwman, A. J. Brookes, T. Clark, M. Crosas, I. Dillo, O. Dumon, S. Edmunds, B. Mons, et al., *Sci. Data* **2016**, *3*, 160018-.

[126] D. Ziegenbalg, A. Pannwitz, S. Rau, B. Dietzek-Ivanšić, C. Streb, *Angew. Chem. Int. Ed.* **2022**, *61*, DOI 10.1002/ANIE.202114106.

[127] A. Rajagopal, F. Venter, T. Jacob, L. Petermann, S. Rau, S. Tschierlei, C. Streb, *Sustain. Energy Fuels* **2019**, *3*, 92–95.

[128] B. C. M. Martindale, E. Joliat, C. Bachmann, R. Alberto, E. Reisner, *Angew. Chem. Int. Ed.* **2016**, *55*, 9402–9406.

[129] B. Kirchhoff, S. Rau, C. Streb, *Eur. J. Inorg. Chem.* **2016**, *2016*, 1425–1429.

[130] M. Natali, M. Orlandi, S. Berardi, S. Campagna, M. Bonchio, A. Sartorel, F. Scandola, *Inorg. Chem.* **2012**, *51*, 7324–7331.

[131] R. Das, S. Chakraborty, S. C. Peter, *ACS Energy Lett.* **2021**, *6*, 3270–3274.

[132] A. Rajagopal, E. Akbarzadeh, C. Li, D. Mitoraj, I. Krivtsov, C. Adler, T. Diemant, J. Biskupek, U. Kaiser, C. Im, M. Heiland, T. Jacob, C. Streb, B. Dietzek, R. Beranek, *Sustain. Energy Fuels* **2020**, *4*, 6085–6095.

[133] L. Sun, B. Åkermark, S. Ott, *Coord. Chem. Rev.* **2005**, *249*, 1653–1663.

[134] C. J. Brown, F. D. Toste, R. G. Bergman, K. N. Raymond, *Chem. Rev.* **2015**, *115*, 3012–3035.

[135] N. Vallavoju, J. Sivaguru, *Chem. Soc. Rev.* **2014**, *43*, 4084–4101.

[136] L. Buzzetti, G. E. M. Crisenza, P. Melchiorre, *Angew. Chem. Int. Ed.* **2019**, *58*, 3730–3747.

[137] J. A. Malik, A. Madani, B. Pieber, P. H. Seeberger, *J. Am. Chem. Soc.* **2020**, *142*, 11042–11049.

[138] T. D. Svejstrup, A. Chatterjee, D. Schekin, T. Wagner, J. Zach, M. J. Johansson, G. Bergonzini, B. König, *ChemPhotoChem* **2021**, *5*, 808–814.

[139] O. S. Wenger, *Nature Chemistry* **2020**, *12*, 323–324.

[140] S. E. Braslavsky, *Pure and Applied Chemistry* **2007**, *79*, 293–465.

[141] S. E. Braslavsky, A. M. Braun, A. E. Cassano, A. V Emeline, M. I. Litter, L. Palmisano, V. N. Parmon, N. Serpone, *Pure Appl. Chem* **2011**, *83*, 931–1014.

[142] M. Sender, F. Huber, M. Moersch, D. Kowalczyk, J. Hniopek, S. Klingler, M. Schmitt, S. Kaufhold, K. Siewerth, J. Popp, B. Mizaikoff, D. Ziegenbalg, S. Rau, *ChemSusChem* **2022**, *15*, DOI 10.1007/s41981-021-00174-1.

[143] W. K. Jo, R. J. Tayade, *Ind. Eng. Chem. Res.* **2014**, *53*, 2073–2084.

[144] D. Kowalczyk, P. Li, A. Abbas, J. Eichhorn, P. Buday, M. Heiland, A. Pannwitz, F. H. Schacher, W. Weigand, C. Streb, D. Ziegenbalg, *ChemPhotoChem* **2022**, *6*, DOI 10.1002/cptc.202200044.

[145] H. J. Kuhn, S. E. Braslavsky, R. Schmidt, *Pure Appl. Chem* **2004**, *76*, 2105–2146.

[146] A. Müller, S. Sarkar, R. G. Bhattacharyya, S. Pohl, M. Dartmann, *Angewandte Chemie International Edition in English* **1978**, *17*, 535–535.

[147] A. Müller, W. Nolte, B. Krebs, *Angewandte Chemie International Edition in English* **1978**, *17*, 279–279.

[148] M. Dave, A. Rajagopal, M. Damm-Ruttensperger, B. Schwarz, F. Nägele, L. Daccache, D. Fantauzzi, T. Jacob, C. Streb, *Sustain. Energy Fuels* **2018**, *2*, 1020–1026.

[149] Y. Lei, M. Yang, J. Hou, F. Wang, E. Cui, C. Kong, S. Min, R. Li, / Chemcomm, C. Communication, *Chem. Commun* **2018**, *54*, 603–606.

[150] M. Heiland, R. De, S. Rau, B. Dietzek-Ivansic, C. Streb, *Chemical Communications* **2022**, *58*, 4603–4606.

[151] A. Müller, E. Krickemeyer, U. Reinsch, *ZAAC - Journal of Inorganic and General Chemistry* **1980**, *470*, 35–38.

[152] J. McAllister, N. A. G. Bandeira, J. C. McGlynn, A. Y. Ganin, Y. F. Song, C. Bo, H. N. Miras, *Nature Communications 2019 10:1* **2019**, *10*, 1–10.

[153] S. A. Weissman, N. G. Anderson, *Org. Process Res. Dev.* **2015**, *19*, 1605–1633.

[154] G. E. P. Box, W. G. Hunter, J. S. Hunter, *Statistics for Experimenters*, Wiley, New York, **1978**.

[155] “Interpretieren der wichtigsten Ergebnisse für Einfache ANOVA - Minitab,” can be found under https://support.minitab.com/de-de/minitab/help-and-how-to/statistical-modeling/anova/how-to/one-way-anova/interpret-the-results/key-results/#step-4-determine-how-well-the-model-fits-your-data, **2025**.

[156] C. G. Morales-Guio, X. Hu, *Acc. Chem. Res.* **2014**, *47*, 2671–2681.

[157] D. Merki, X. Hu, *Energy Environ. Sci.* **2011**, *4*, 3878–3888.

[158] T. Wang, H. Xie, M. Chen, A. D’Aloia, J. Cho, G. Wu, Q. Li, *Nano Energy* **2017**, *42*, 69–89.

[159] J. D. Benck, T. R. Hellstern, J. Kibsgaard, P. Chakthranont, T. F. Jaramillo, *ACS Catal.* **2014**, *4*, 3957–3971.

[160] R. A. Sheldon, *Chem. Soc. Rev.* **2012**, *41*, 1437–1451.

[161] B. Seo, S. H. Joo, *Nano Converg.* **2017**, *4*, 1–11.

[162] A. A. Adesina, *Catalysis Surveys from Asia* **2004**, *8*, 265–273.

[163] L. Candish, K. D. Collins, G. C. Cook, J. J. Douglas, A. Gómez-Suárez, A. Jolit, S. Keess, *Chem. Rev.* **2022**, *122*, 2907–2980.

[164] S. L. Y. Tang, R. L. Smith, M. Poliakoff, *Green Chemistry* **2005**, *7*, 761–762.

[165] D. Kowalczyk, G. Knorr, K. Peneva, D. Ziegenbalg, *React. Chem. Eng.* **2023**, *8*, 2967–2983.

[166] H. E. Bonfield, T. Knauber, F. Lévesque, E. G. Moschetta, F. Susanne, L. J. Edwards, *Nature Communications 2020 11:1* **2020**, *11*, 1–4.

[167] R. Carlson, J. Carlson, *Design and Optimization in Organic Synthesis*, Google Books, **2005**.

[168] V. Czitrom, *American Statistician* **1999**, *53*, 126–131.

[169] N. Serpone, *J. Photochem. Photobiol. A Chem.* **1997**, *104*, 1–12.

[170] A. Salinaro, A. V. Emeline, N. Serpone, J. Zhao, H. Hidaka, V. K. Ryabchuk, *Pure and Applied Chemistry* **1999**, *71*, 321–335.

[171] A. P. Demchenko, *Methods Appl. Fluoresc.* **2020**, *8*, DOI 10.1088/2050-6120/AB7365.

[172] A. Müller, E. Diemann, R. Jostes, H. Bögge, *Angewandte Chemie International Edition in English* **1981**, *20*, 934–955.

[173] E. F. Schuberiil, *Light Emitting Diodes*, E. Fred Schubert, Troy, New York, **2018**.

[174] A. Beer, *Annalen der Physik und Chemie* **1852**, *86*, 78–88.

[175] F. Neese, *Wiley Interdiscip. Rev. Comput. Mol. Sci.* **2025**, *15*, e70019.

[176] A. D. Becke, *J. Chem. Phys.* **1993**, *98*, 5648–5652.

[177] F. Weigend, R. Ahlrichs, *Physical Chemistry Chemical Physics* **2005**, *7*, 3297–3305.

[178] S. Grimme, S. Ehrlich, L. Goerigk, *J. Comput. Chem.* **2011**, *32*, 1456–1465.

[179] S. Grimme, J. Antony, S. Ehrlich, H. Krieg, *Journal of Chemical Physics* **2010**, *132*, DOI 10.1063/1.3382344/926936.

[180] D. Andrae, U. Häußermann, M. Dolg, H. Stoll, H. Preuß, *Theor. Chim. Acta* **1990**, *77*, 123–141.

[181] B. Seo, G. Y. Jung, S. J. Lee, D. S. Baek, Y. J. Sa, H. W. Ban, J. S. Son, K. Park, S. K. Kwak, S. H. Joo, *ACS Catal.* **2020**, *10*, 652–662.

[182] S. H. Kolbinger, L. Haxha, P. Schröder, D. Kowalczyk, L. Senz, L. Schleicher, A. Mukherjee, D. Malcolm, C. L. Kufner, D. Ziegenbalg, C. Streb, *Sustain. Energy Fuels* **2026**, *10*, 1313–1320.

[183] “Werkzeuge für Datenanalyse, Statistik und Prozessverbesserung | Minitab,” can be found under https://www.minitab.com/de-de/, **2025**.

[184] A. Valaei, A. Hofmann, A. Rose, P. Kuschmitz, P. Voepel, B. Milow, R. Marschall, D. Ziegenbalg, *Chemical Engineering Journal* **2025**, *524*, DOI https://doi.org/10.1016/j.cej.2025.168924.

[185] M. Cossi, N. Rega, G. Scalmani, V. Barone, *J. Comput. Chem.* **1998**, *24*, 669.

[186] F. Plasser, *Journal of Chemical Physics* **2020**, *152*, DOI 10.1063/1.5143076.

[187] W. Hu, L. Xie, C. Gu, W. Zheng, Y. Tu, H. Yu, B. Huang, L. Wang, *Coord. Chem. Rev.* **2024**, *506*, 215715.

[188] S. Batool, M. Langer, S. N. Myakala, M. Heiland, D. Eder, C. Streb, A. Cherevan, *ADVANCED MATERIALS* **2024**, *36*, DOI 10.1002/adma.202305730.

[189] Y. Lei, M. Yang, J. Hou, F. Wang, E. Cui, C. Kong, S. Min, *Chemical Communications* **2018**, *54*, 603–606.

[190] A. Baloglou, M. Ončák, M. L. Grutza, C. Van Der Linde, P. Kurz, M. K. Beyer, *Journal of Physical Chemistry C* **2019**, *123*, 8177–8186.

[191] T. Wang, J. Zhuo, K. Du, B. Chen, Z. Zhu, Y. Shao, M. Li, T. Y. Wang, J. Q. Zhuo, K. Z. Du, B. B. Chen, Z. W. Zhu, Y. H. Shao, M. X. Li, *Advanced Materials* **2014**, *26*, 3761–3766.

[192] B. Keita, S. Floquet, J.-F. Lemonnier, E. Cadot, A. Kachmar, M. Bénard, M.-M. Rohmer, L. Nadjo, *The Journal of Physical Chemistry C* **2008**, *112*, 1109–1114.

[193] Z. Huang, W. Luo, L. Ma, M. Yu, X. Ren, M. He, S. Polen, K. Click, B. Garrett, J. Lu, K. Amine, C. Hadad, W. Chen, A. Asthagiri, Y. Wu, *Angew. Chem. Int. Ed.* **2015**, *54*, 15181–15185.

[194] S. Henriette Kolbinger, Laura Haxha, P. Charlotte Schröder, Daniel Kowalczyk, Luis Senz, Luca Schleicher, Arijit Mukherjee, Daniel Malcolm, C. L. Kufner, Dirk Ziegenbalg, Carsten Streb, *Sustain. Energy Fuels* **2026**, DOI 10.1039/D5SE01490E.

[195] Vaidyalingam A., Dutta P. K., *Anal. chem.* **2000**, *72*, 5219–5224.

[196] S. Liu, B. Chen, Y. Yang, Y. Yang, Q. Chen, X. Zeng, B. Xu, *Electrochem. commun.* **2019**, *109*, DOI 10.1016/j.elecom.2019.106583.

[197] E. Deponti, A. Luisa, M. Natali, E. Iengo, F. Scandola, **2014**, *43*, 16345.

[198] M. P. Mclaughlin, T. M. Mccormick, R. Eisenberg, P. L. Holland, *Chemical Communications* **2011**, *47*, 7989–7991.

[199] H. Ooka, J. Huang, K. S. Exner, *Front. Energy Res.* **2021**, *9*, 654460.

[200] F. Neese, *WIRES-Comp. Mol. Sci.* **2012**, *2(1)*, 8.

[201] F. Neese, *WIRES-Comp. Mol. Sci.* **2022**, *e1606*, 1.

[202] J. Tao, J. P. Perdew, V. N. Staroverov, G. E. Scuseria, *Phys. Rev. Lett.* **2003**, *91*, 146401.

[203] F. Weigend, R. Ahlrichs, *PCCP* **2005**, *7*, 3297.

[204] S. Grimme, S. Ehrlich, L. Goerigk, *J. Comput. Chem.* **2011**, *32*, 1456.

[205] S. Grimme, J. Antony, S. Ehrlich, H. Krieg, *J. Chem. Phys.* **2010**, *132*, 154104.

[206] D. Andrae, U. Häussermann, M. Dolg, H. Stoll, H. Preuss, *Theor. Chim. Acta* **1990**, *77*, 123.

[207] A. D. Becke, *J. Chem. Phys.* **1993**, *98*, 5648.

[208] C. Lee, W. Yang, R. G. Parr, *Phys. Rev. B* **1988**, *37*, 785.

[209] A. Chapovetsky, P. Patel, C. Liu, A. P. Sattelberger, D. M. Kaphan, M. Delferro, *Organometallics* **2020**, *39*, 4430–4436.

[210] F. A. Cotton, C. A. Murillo, R. A. (eds) Walton, *Multiple Bonds between Metal Atoms*, Springer, **2006**.

6 Curriculum vitae

Adress: [redacted]

Mobile: [redacted]

Mail: henriette.kolbinger@uni-mainz.de

Date and place of birth: [redacted], Worms

Education

06.2023 – present **Studii doctorale**

- Johannes Gutenberg-University Mainz, Inorganic Chemistry, Group of Prof. Carsten Streb
  Funded by a grant from the HaVo-foundation

04.2021 – 03.2023 **Master's program**

- Johannes Gutenberg-Universität Mainz:
  M. Sc. Chemistry (Grade: 1,6)

Master thesis: In Cooperation with Thermo Fisher Scientific Bremen and the Max Planck-Institute for Chemistry Mainz:
Development of a Method to Analyze Stable Isotopes in Phosphates Using Orbitrap Mass Spectrometry
(Grade: 1,2)

04.2018 – 03.2021 **Bachelor's program**

- Johannes Gutenberg-University Mainz:
  B. Sc. Chemistry (Grade: 2,0)

Bachelor thesis: In Cooperation with the Max Planck-Institute for Polymer research Mainz:
Spectroscopic Investigations of Flow at Water Mineral Interfaces
(Grade: 1,4)

[redacted]

7 Acknowledgements

It's been a long way since I have come to the point of finishing my PhD. Even though three years do not seem to be such a long time after all. I really enjoyed the time, and I am very grateful for everyone that made it possible and accompanied me. Therefore, I would like to name them some of them here and thank them here personally.

First and foremost, I would like to thank **Prof. Dr. Carsten Streb**. I always enjoyed working with him a lot and could not wish for a better supervisor. He always supported and guided me in the best way and enabled me to unfold my full potential while following my interests. There never was anything that could not be done and whenever necessary he always had an appointment at short notice ready. I am also especially grateful that he suggested me for the HaVo scholarship which I wouldn't have gotten without him. In that way he paved my way into the future and into industry.

At this point, I would also like to thank the **HaVo-foundation** for the financial support throughout the last year of my PhD and honoring me with this scholarship.

Second, I would like to thank **Prof. Dr. Katja Heinze** for being my second thesis examiner.

Another important part of my whole PhD was the students that I supervised. They really performed many, many experiments for the projects and it was a lot of fun to work with them! So, thank you, **David, Laura, Charly, Daniil, Kristina and Luca**. It was a special honor for me to supervise Lucas Master thesis as I have known him since his first semester. I really enjoyed this time and am grateful for the trust you have put in me. The collaboration with you now as a colleague makes me proud and I am truly grateful for your support throughout all of my projects!

Thanks also go to my Hiwis **Klara** and **Anni** for their motivated work.

But for those of you who know me better, you surely now think that I must have forgotten someone. I can assure you that this is not the case but the person I want to thank next deserves special thanks.

For me, he has many names like Ricci, Melissa, Melissa-Shanice or Leolui, but you better know him as **Luis**. Without Luis my work would have been a lot slower and most likely more tedious. Your drive to upgrade the laboratory setups has enabled me and the whole group to set the limits higher than before and saves us an immense amount of time! I feel very honored that you trusted me with the supervision of both your bachelor and your master thesis. It was amazing to see you thrive, your motivation and your passion and I am looking forward to seeing what you will accomplish and create in your PhD thesis. Especially when you tell me about it from your window across the yard.

Furthermore, I would like to thank the whole group for all the great memories I was allowed to make with them! I really enjoyed all of our social events and organizing them for you! Special thanks go to **Moritz J.** for always supplying me with the catalysts and

teaching my students how to synthesize them. Another special thanks go to **Kiki** for always having an open ear and the nice lunches we had and of course for the great music you showed me and we enjoyed ourselves together.

Another special person for me from our working group is definitely **Yuliia**. Thank you so much for the great coffee breaks! I had a lot of fun working with you on the business trip forms and the FMOCS. I really enjoy our hair stylist appointments.

Next up, I would like to thank all of my collaboration partners for their dedicated work, insightful discussions and support. Of course, also here is a special person that I want to give a special thanks to: **Dani**. Your truly inspiring work was the basis for my whole research and with your drive and knowledge you were a great teacher to me.

Thank you, **Dirk**, as well. I also learned a lot from your expertise and our collaborations.

In general, I would like to thank the whole **Catalight consortium**. Thanks to this network, I met many amazing people and researchers like **Evii**. Thank you for the many laughs we had and your amazing Pizzaschnecken.

Another extremely important part of my life is of course my friends! I am grateful for every single one of them and how they have lifted me up when I was feeling down and how they reminded me that what I am doing is not the usual. Especially, thank you, **Sonja** my sister of the zee, for kite surfing with me, taking care of me, sewing my pants and being the herb witch in my life; thank you, **Franzi,** for all of these amazing conversations we have; and thank you**, Tanja** my Zwingling, for showing me movies from the 80s and leaving the center part of the ice cream to me. You girls are absolutely amazing!

A really special thanks goes to **Nuri**. From my early semesters in my bachelor's studies, you always provided me with helpful advice and helped me to fulfill my dreams step by step. Without you my path would have looked a lot different. Thanks for the unconditional support in any situation!

Thank you also, **Barbara**, for the nice Sundays and vacations we always have!

I would also like to thank my **parents**. They taught me how to be a strong and independent woman, while supporting my interests in science and dancing. Especially my dad supported my scientific curiosity. Your early support of my dreams enabled me to follow them without any worry or doubt.

Thanks again to everyone who helped me get through my last tonsilitis last year. It really was a crazy time. Here, I would like to thank **Luca** especially for caring and being there. Your cooking and support helped me through that time immensely and in general through my last year of PhD.

Last but not least I would like to take the time to thank myself for keeping up with my ambitious plans and that I did not let any hindering like sickness or non-working machines stop me. I'm truly grateful that I was able to achieve this goal in the time I had planned for it. Now I'm ready to mess up the industry.